SOL-GEL MATERIALS FOR INTEGRATED OPTICS

by

Jason E. Chisham

A thesis submitted to the Faculty of Graduate

Studies and Research in partial fulfillment

of the requirements for the degree of

Master of Science

Department of Chemistry

McGill University

Montreal, Quebec, Canada

© May 1996

Canada

in memory of

Joseph Wrobel

(a.k.a. Gramps)

Abstract

The sol-gel process is a low temperature solution route to amorphous and crystalline materials. Organic modification of the precursors allows the formation of organic-inorganic composite materials. We use the sol-gel process to produce an organically-modified ceramic for integrated optical applications. Photosensitive organic components allow the fabrication of passive integrated optical devices by photolithography. We demonstrate the fabrication and characterization of channel waveguides, waveguide devices and gratings in this material. Active devices based on the emission of erbium at 1.55 μm are under much investigation because of their potential use in telecommunications. Luminescence quenching is a major problem as an Er^{3+} ion in its excited state transfers its energy to a nearby vibrational mode of its environment and decays non-radiatively to the ground state. Encapsulation of the ion into a coordination sphere to shield the ion from its surroundings may lead to reduced quenching. We synthesize several erbium tetrakis β-diketone complexes and dope them into different solvent environments and sol-gel hosts to probe guest-host interactions in the excited state.

Résumé

Le procédé sol-gel est une solution de basse température sur la voie des matériaux amorphes et cristallins. La modification organique des précurseurs permet la formation de matériaux composites organiques-inorganiques. Nous utilisons le procédé sol-gel afin de produire une céramique modifiée par voie organique pour des applications en optique intégrée. Les composantes photosensibles organiques permettent la fabrication de dipositifs passifs d'optique intégrée par photolithographie. Nous démontrons la fabrication ainsi que la caratérisation de canaux de guides d'ondes, de dispositifs à guide d'ondes ainsi que de reseaux à partir de ce matériau. Les dispositifs actifs basés sur l'émission de l'erbium à 1.55 μm font l'objet de plusieurs investigations à cause de leur utilization potentielle dans le domaine des télécommunications. La désactivation de la luminescence est un problème majeur car un ion Er^{3+} dans son état excité transfère son énergie à un mode de vibration voisin et revient de façon non-radiative à l'état fondamental. L'encapsulation de l'ion à l'intérieur d'une sphère de coordination pour protéger l'ion de son environnement pourrait mener à une réduction de la désactivation. Nous synthétisons plusieurs complexes d'erbium tetrakis β-diketone et les dopons dans différents solvents et hôtes sol-gel pour sonder les interactions dans l'état excité.

Acknowledgements

Table of Contents

List of Figures and Tables

General Introduction

The term "integrated optics" was first coined in 1969 by S.E. Miller to describe the fabrication of complex optical circuits on a single chip consisting of miniaturized components interconnected by small optical transmission lines, or waveguides. This, he proposed, could be accomplished using lithographic techniques analogous to the fabrication of electronic integrated circuits. The field of integrated optics includes the guiding, generation, manipulation and detection of light waves, and the coupling of these waves into and out of integrated optical circuits. The devices that make up these circuits can be classified as active or passive. Active devices, such as lasers and electro-optic modulators, perform their functions due to the application of an external field. Passive devices, such as power dividers and wavelength division multiplexers, are designed to operate without application of an external field.

There are several materials that are currently being used for integrated optics, both commercially and in the laboratory. Lithium niobate, with its excellent electro-optic and piezoelectric properties, and semiconductor materials, with the advantage of full integration with electronics, have been the materials of choice to date. Interest in glass has been increasing due to its many inherent advantages over the previously mentioned materials. These include high mechanical, thermal and chemical stability, high threshold-to-optical damage ratio, and small coupling losses between optical fibers and glass waveguides due to a close match in refractive index. Among the many different processes for making glass integrated optics devices, the sol-gel process is particularly attractive. It

1

is a low temperature, solution process in which metal alkoxides undergo hydrolysis and polycondensation to yield glasses. Resulting material properties can be tailored via judicious choice of reagents. Because the reactions occur in solution, doping with active materials readily occurs.

Active devices based on erbium doped glasses are currently receiving much attention. Their importance lies in the characteristic emission of erbium at 1.55 μm, which is an important wavelength in optical fiber telecommunications. Devices such as waveguide lasers and amplifiers utilizing this wavelength are expected to be important elements in future fiber optic networks.

The materials we have studied are organically modified sol-gels. One, (referred to throughout this thesis as the ormocer) which was investigated primarily in thin film form, consists of a silicon alkoxide with a photopolymerizable organic substituent, and a zirconium alkoxide complexed by the carboxylate of methacrylic acid. On exposure to ultraviolet radiation, the organic components polymerize, causing an increase in refractive index. Its material properties are discussed in Chapter 1. Waveguides, waveguide devices, and gratings were made from this material and are discussed in Chapter 2. Erbium, in the form of coordination complexes, was doped into the sol for luminescence investigations. Another sol-gel was prepared from methyltrimethoxysilane (MTMS). This was used primarily as an alternate host material for erbium complexes. Erbium doped sol-gels are presented in Chapter 3.

1. Optical Materials via the Sol-Gel Process

1.1. Introduction

1.1.1. Sol-Gel Chemistry

The sol-gel process is a low temperature liquid phase route to amorphous and crystalline materials that proceeds via the hydrolysis and polycondensation of alkoxides.[1] In principle, the process is applicable to any metal alkoxide (M = B, Al, Ti, Zr, etc.); however, silicon alkoxides have been the most intensively studied. There are three general reactions that can be written to represent the sol-gel process, for which silicon alkoxides will be used as examples:

$$\equiv Si-OR + H_2O \leftrightarrow \equiv Si-OH + ROH \qquad (1.1)$$

alcohol condensation $\qquad \equiv Si-OR + HO-Si \equiv \leftrightarrow \equiv Si-O-Si \equiv + ROH \qquad (1.2)$

water condensation $\qquad \equiv Si-OH + HO-Si \equiv \leftrightarrow \equiv Si-O-Si \equiv + H_2O \qquad (1.3)$
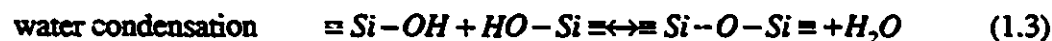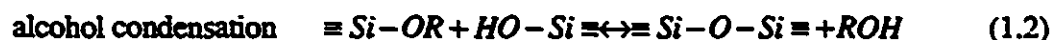
Solvents are commonly used to homogenize the alkoxides and water which are most often immiscible. Solvents also help to control the concentrations of silicate species and water in regards to gelation kinetics.

One of the most important parameters in sol-gel chemistry is the H_2O:Si molar ratio (r-value). In theory, complete hydrolysis of a tetrafunctional alkoxide can be accomplished with an r-value of 2. In practice, this does not occur. In fact, even with r-values up to 50, some alkoxide groups remain unhydrolyzed. This is most probably due to alcoholysis of Si-O-Si bonds (the reverse of reaction 1.2) reforming alkoxy groups.

Another important factor in regards to the kinetics of the reactions is the steric bulk and electron donating or withdrawing characteristics of the alkoxide groups or organic substituents. These have a great influence on the rates of the hydrolysis and condensation reactions.

Brinker and Scherer[1] have described the hydrolysis and condensation reactions in detail. It is generally accepted that the hydrolysis reaction occurs by nucleophilic attack of oxygen in water at the Si atom. The reaction is usually catalyzed by acid or base. In acid catalyzed hydrolysis, an alkoxide group is protonated, drawing electron density away from Si. This makes Si more electrophilic and prone to nucleophilic attack by water. As a water molecule attacks, it acquires a partial positive charge, making the protonated alkoxide a better leaving group. The transition state has S_N2 character and inversion of configuration usually occurs with good leaving groups.
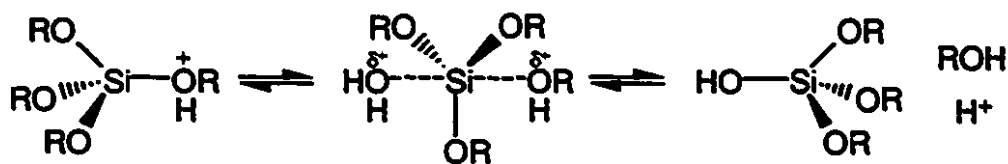
Figure 1.1 Acid catalyzed hydrolysis with inversion of configuration

Hydrolysis rates are increased with groups that do not give rise to substantial steric crowding around Si. Substitution of alkoxide groups with alkyl groups also increases the rate, since these electron donating substituents help stabilize the positive charge Si acquires in the transition state.

In base catalyzed hydrolysis, OH⁻ attacks Si, displacing OR⁻ in an S_N2 mechanism. This results in inversion of configuration.
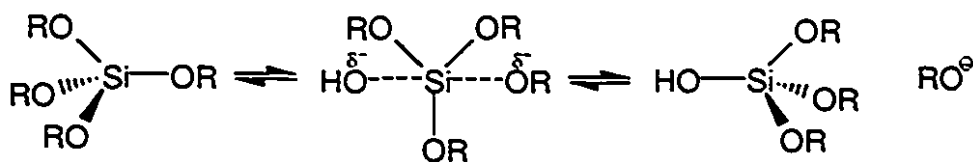
Figure 1.2 Base catalyzed hydrolysis with inversion of configuration

Another mechanism suggests the formation of a stable five-coordinate intermediate. Two transition states are formed, the second of which can lead to loss of any ligand.
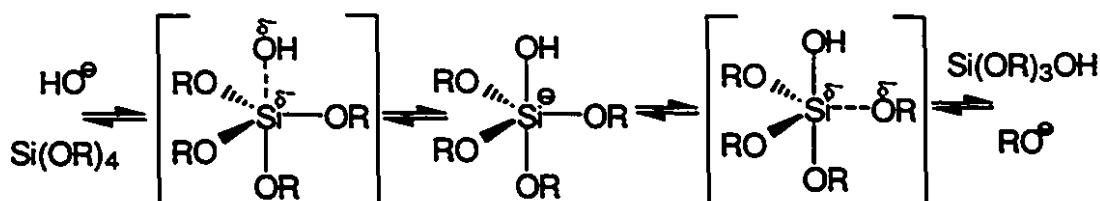
Figure 1.3 Base catalyzed hydrolysis with retention or inversion of configuration

Electron withdrawing substituents which help to stabilize the negative charge on Si increase the hydrolysis rate. Electron donating groups, e.g., alkyls, do just the opposite.

Condensation reactions produce either alcohol or water. The product that dominates is primarily determined by the r-value: for r << 2 the alcohol producing reaction is favoured, while for r >> 2 the water producing reaction is favoured. In base catalyzed condensation, OH⁻ deprotonates a silanol which then takes part in a nucleophilic attack on a siloxane. Acidity of the silanols is determined by the other substituents on Si. As more basic groups (OR and OH) are replaced by OSi, the acidity of the remaining silanols increases due to the polarizing effect of reduced electron density on Si. One possible mechanism involving a stable pentacoordinate intermediate is shown in Fig. 1.4.

5

$$\equiv\text{SiOH} + \text{HO}^{\ominus} \longrightarrow \equiv\text{SiO}^{\ominus} + \text{H}_2\text{O} \xrightleftharpoons{\text{Si(OR)}_4}$$

Figure 1.4 *Base catalyzed condensation*

In acid catalyzed condensation, nucleophilic attack by a neutral species on a protonated silanol occurs. Silanols most likely to be protonated are found on monomers and on end groups of chains, since these are the most basic silanols.

Figure 1.5 *Acid catalyzed condensation*

Thus it can be seen that basic catalysts lead to compact, branched structures which are more suited to formation of monoliths. Acid catalysts produce extended, less branched polymers suitable for film formation since these chains can more easily flow past each other and cover the substrate surface.[2]

As condensation reactions occur, particles continually increase in size until a sol results (a colloidal suspension of solid particles in a liquid). The size of the sol particles depends heavily on the pH of the solution. For example, in the range of pH 2-7 for acid catalysts, particle size is ~2-4 nm since solubility of silica is low in this pH range. Under

6

basic conditions, sol particles are larger due to greater silica solubility at higher pH. With time, the sol particles aggregate to form a gel (a molecule of macroscopic dimensions extending throughout the solution). Further aging results in solvent evaporation and shrinkage of the solid network finally yielding a porous, amorphous, bulk solid known as a xerogel. Densification of xerogels can be accomplished by sintering at elevated temperatures. If the gel is dried under supercritical conditions, no shrinkage occurs, resulting in a very porous solid known as an aerogel.

Some researchers have developed procedures for making non-shrinking gels which do not require supercritical drying conditions. Ellsworth et al.[3] have produced transparent non-shrinking composites with a wide range of glass/polymer ratios. They use poly(silicic acid esters) bearing polymerizable alkoxides where the cosolvent and liberated alcohol polymerize. Thus gel drying is unnecessary and shrinkage does not occur. Prakash et al.[4] have prepared aerogel films by adding surface groups to inorganic gels. As the solvent evaporates, the gel springs back to a porous state. They have reported that porosities up to 98.5% are attainable by this method.

1.1.2. Optical Applications

One of the greatest attributes of making glasses by the sol-gel process is the ability to dope with a wide range of active materials. Dopants are usually introduced at the sol-stage and become entrapped in the pores of the gradually forming matrix. Porous transparent materials make very good hosts for biomolecules. Those which retain their activity while encapsulated in a silicate glass can have applications as optically based

7

biosensors.[5,6,7,8] The porosity of sol-gel glasses allows small analyte molecules to diffuse into the matrix while large receptor molecules (e.g., enzymes or proteins) remain fixed in the pores. Reactions occurring in the glass can then be monitored spectroscopically. The same is true for optically based chemical sensors where a number of different indicator molecules have been encapsulated for sensing pH,[9] metal ions[9] and gases.[10]

Other molecules that have been doped into sol-gels include those that are photochromic,[11] electro-optic,[12] and luminescent (both laser dyes[13,14] and rare earth ions[15,16,17]). The sol-gel process has also been used to make non-linear optical (NLO) materials. NLO active molecules such as organics[18,19] and quantum dots[20] (semiconductor microcrystallites which exhibit three-dimensional quantum confinement) can be doped into the sol. Alternatively, NLO chromophores can be bonded directly to the siloxane monomer and become a part of the framework on gelation.[21,22,23]

Thin films are used extensively in optical applications, from antireflective coatings[24] to waveguide lasers[25]. The ease of depositing thin, homogeneous films suitable for a particular application is no trivial matter, regardless of the method used. In regards to the sol-gel process, the sol stage is very conducive to casting films either by spin- or dip-coating. Rapid evaporation of solvent increases rates of condensation. Accordingly, gelation occurs much more quickly in films than in monoliths. Factors that must be taken into consideration here are interfacial adhesion between the substrate and the film, thermal, chemical and mechanical stability, cracking of the film on drying, and the need for multi-layer processing.

1.1.3. Organic Modification

Purely inorganic sol-gels lead to films that are brittle and often crack on drying.[26] In addition, films are very thin ($<<1\mu m$) and multiple coatings are often necessary for integrated optical applications. The use of a hybrid organic/inorganic system allows the formation of thicker, crack-free films. These materials are known as ormosils (organically modified silicates), or ormocers (organically modified ceramics). Physical and optical properties of the glasses can easily be tailored via choice of organic substituents.

Novak has outlined different ways in which organic modification can be accomplished.[27] One method involves embedding organic polymers in a glassy matrix. This is achieved by carrying out the hydrolysis and condensation of alkoxides in the presence of organic polymers, provided there is no phase separation. Another method is to use organic polymers containing trialkoxysilyl pendant groups, which then hydrolyze and condense with inorganic alkoxides. Additionally, substituted organo-siloxane monomers may be used. For simple alkyl substituents, the resulting glass has some organic character, but there is no organic polymer network. If the organic substituent is polymerizable, then a secondary organic network can be formed within the sol-gel. The material properties of this type of system can be exploited in many ways. Photolithographic writing of integrated optical devices in films of this type of material will be discussed in Chapter 2.

1.1.4. Kinetics of Sol-Gel Reactions

The characteristics of the organic substituent not only influences the resulting material properties, but also the sol-gel reactions themselves. As previously mentioned,

electron donating alkyl groups tend to increase acid-catalyzed hydrolysis rates but retard base-catalyzed rates. The size of the organic substituent also influences rates. Large, bulky groups decrease rates compared with smaller, unbranched groups. Kinetic control of a sol-gel reaction by choice of reagents is very useful.

In multicomponent systems, where two or more metal alkoxides are present, reagents may hydrolyze at different rates sufficient to form domains richer in one component than the other. Precipitation may also occur. One solution to this problem is to use mixed-metal alkoxides, where the starting alkoxide contains all the metals in the proper stoichiometry. The use of a double metal alkoxide is quite common in the formation of aluminosilicate gels.[28] Another approach is to add reagents in reverse order of their reactivities. In this method, partial hydrolysis of the less reactive component occurs first so that when the more reactive component is added, heterocondensation is promoted.[29] Reagents can also be modified chemically to control rates. Transition metal alkoxides hydrolyze much faster than their silicon counterparts and require strict processing control to prevent precipitation. Chelating agents can be very effective at slowing down hydrolysis and condensation rates provided they are stable in aqueous solution.

1.1.5. Refractive Index Control

One of the most important properties of optical materials that can be controlled by choice of reagents is refractive index. Buckman provides a thorough discussion of how polarizability at the molecular level determines refractive index of the bulk material.[30]

10

The microscopic process of polarization determines the effect a dielectric material has on light propagating through it. Dipole moments are created by the electric field of light, E, and these microscopic dipole moments add up to give a macroscopic dipole moment per unit volume, P. For optically linear materials, P is related to E by:

$$P = \chi \varepsilon_0 E \qquad (1.4)$$

where χ is the dielectric susceptibility and ε_0 is the permittivity of vacuum. The electric displacement, D, is related to E by:

$$D = \varepsilon_0 n^2 E = \varepsilon_0 E + P \qquad (1.5)$$

The refractive index, n, is thus determined by microscopic dipole moments induced in response to an electric field.

The microscopic dipole moment produced by an electric field is given by:

$$p = \alpha E \qquad (1.6)$$

where α is the polarizability of the atom. A typical solid can consist of many different polarizable species. The macroscopic polarization, P, can be calculated at any given position in a solid consisting of k different kinds of polarizable species with volume concentrations N_j by:

$$P = \sum_{j=1}^{k} N_j \alpha_j E_{loc} \qquad (1.7)$$

where E_{loc} is the local electric field. This P acts as a driving force for further formation of microscopic dipole moments. The expression which shows how all polarizable species in the solid combine to form the refractive index is given by the Claussius-Mossotti relation:

$$\frac{n^2 - 1}{n^2 + 2} = \frac{1}{3\varepsilon_0} \sum_{j=1}^{k} N_j \alpha_j \qquad (1.8)$$

11

Thus, the refractive index of the material can be tailored by suitable choice of reagents. For example, large, easily polarizable atoms such as lead, silver or zirconium will lead to materials with high refractive indices. Refractive index control is imperative in the field of integrated optics since the fundamental concept is the control and manipulation of light through materials. The most basic structure in integrated optics is the waveguide.

1.1.6. Waveguiding

A waveguide, depicted in Fig. 1.6, is a dielectric medium which transports energy at wavelengths in the infrared and visible portion of the electromagnetic spectrum. A necessary condition for waveguiding is that the refractive index of the waveguide must be greater than that of the surrounding media ($n_2 > n_1, n_3$). In addition, there is a minimum waveguide thickness that must exist which depends on the refractive indices of all media and on the wavelength of light that is to be guided. The propagation of a beam in a waveguide may be described in ray optics terms by applying Snell's Law for total internal reflection at both interfaces.
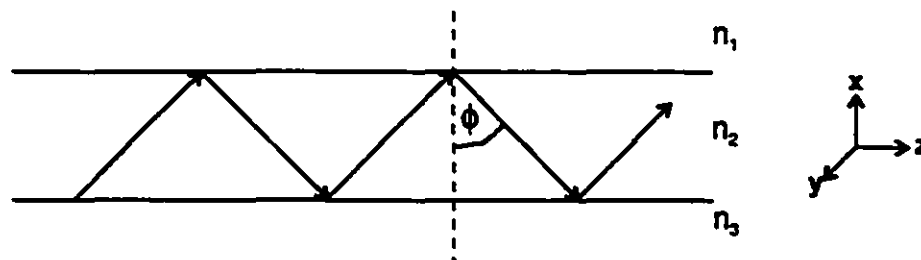
Figure 1.6 *Ray optics approximation of propagation of light in a waveguide*

12

Light waves propagate through the waveguide in distinct modes. A mode can be described as a spatial distribution of optical energy in one or more dimensions. Fig. 1.7 shows the electric field distribution for the m = 0, 1 and 2 modes.

m=0   m=1   m=2
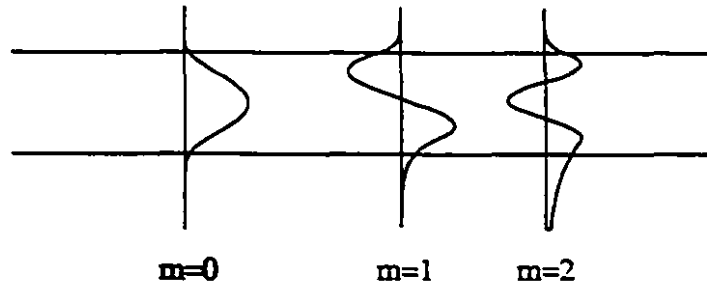
Figure 1.7 *Electric field distributions for the m=0,1, and 2 modes*

Each of these allowed modes (m = 0,1,2,...) has a propagation constant β_m given by Eqn. 1.9[31]:

$$\beta_m = k n_2 \sin \phi_m \qquad (1.9)$$

where k is a constant dependent on wavelength.

Modes possess well defined polarizations which are either transverse electric (TE, polarization of the electric field in the plane of the waveguide), or transverse magnetic (TM, polarization of the magnetic field in the plane of the waveguide). In both cases, the wave field extends outside the physical boundaries of the waveguide and is present as an evanescent field. As the mode order increases, the length of the evanescent tails in the superstrate and substrate increase, and thus carry a greater fraction of their total power outside the guiding layer than do lower order modes. It is therefore desirable in many cases to have waveguides that guide only the fundamental mode.

13

1.2. Experimental

1.2.1. Materials

3-Methacryloxypropyltrimethoxysilane (MAPTMS) inhibited with 250 ppm hydroquinone, and methyltrimethoxysilane (MTMS) were obtained from United Chemical Technologies Inc. (Bristol, PA). Methacrylic acid (MAA), 99% purity, inhibited with 250 ppm hydroquinone monomethyl ether, was obtained from Aldrich. The inhibitors were removed by passing the liquids through an inhibitor remover column packed with a polystyrene-divinylbenzene copolymer obtained from Aldrich. Zirconium (IV) n-propoxide ($Zr(OPr^n)_4$), 70 wt% solution in 1-propanol, was also obtained from Aldrich and used without further purification. IRGACURE-184 (1-hydroxycyclohexyl-1-phenylketone) was obtained from CIBA.

Substrates

Corning glass (2947) microscope slides (1 mm thick), $n_D=1.5115$, were purchased from Aldrich. Silicon wafers ($\langle100\rangle$ crystal cut) with a 2 $\mu m \pm 2.5\%$ thick thermal oxide layer were purchased from Si-Tech Inc. (Topsfield, MA). Silicon wafers ($\langle111\rangle$ crystal cut) were purchased from Silicon Quest International (Santa Clara, CA). Substrates were cleaned with a mild detergent, rinsed in flowing deionized water, then soaked in hot 1,1,1-trichloroethylene for 10 minutes. This was followed by rinsing in hot acetone then hot isopropanol and finally drying with nitrogen.

1.2.2. Sol-Gel Synthesis

Synthesis of the ormocer sol-gel was based on a procedure developed by H. Krug et al.[32] The glass can be prepared with various ratios of MAPTMS:Zr(OPr^n)$_4$:MAA; however, the ratio of Zr(OPr^n)$_4$:MA is always 1:1. The following is a detailed experimental procedure for a sol-gel with molar ratios of components of 5:2:2:

0.54 g (0.030 mol) of 10^{-2} M HCl is added dropwise to 10 g (0.040 mol) of MAPTMS stirred at room temperature in a 5 dram vial. In another 5 dram vial, 1.39 g (0.016 mol) of MAA is added dropwise to 7.54 g (0.016 mol) of Zr(OPr^n)$_4$, also stirred at room temperature. This forms a complex allowing the zirconium to be incorporated homogeneously into the sol without precipitation. After approximately 45 minutes, the pre-hydrolyzed MAPTMS is added slowly to the zirconium complex, and the combination allowed to stir for a further 45 minutes. This is followed by dropwise addition of 0.98 g (0.054 mol) of water. Following another 45 minutes of stirring, 0.31 g (1.5 wt%) of photoinitiator (IRGACURE 184) is rapidly dissolved. Finally the sol is filtered through a 0.2 μm Teflon filter and kept in a covered vial.

The MTMS sol-gel was prepared following the procedure of Haruvy and Webber.[33] 0.40 g (0.022 mol) of 10^{-2} M HCl was added to 2.0 g (0.015 mol) of MTMS (r = 1.5) at room temperature in a vial. Stirring was commenced and then the vial was lowered into a 75°C water bath. The initially diphasic mixture of clear and colourless liquids homogenized after 1 minute. During the reaction, some methanol was lost due to boiling during the course of the reaction (b.p. MeOH, 64.6°C). After 15 minutes, a clear, colourless, viscous sol was produced.

1.2.3. Sample Fabrication

Bulk samples were prepared by pouring the sol into a glass vial then covering it with perforated Parafilm® to let the solvent slowly evaporate at room temperature for several days.

Ormocer films were prepared by dip-coating. This procedure consists of submerging a substrate in the sol, then withdrawing it at a constant velocity to produce thin, homogeneous films. The dip-coating apparatus consisted of two Nanomover® micropositioners (Melles Griot) mounted in parallel to give a total vertical displacement of 5 cm. Fig. 1.8 schematically shows the dip-coating process.
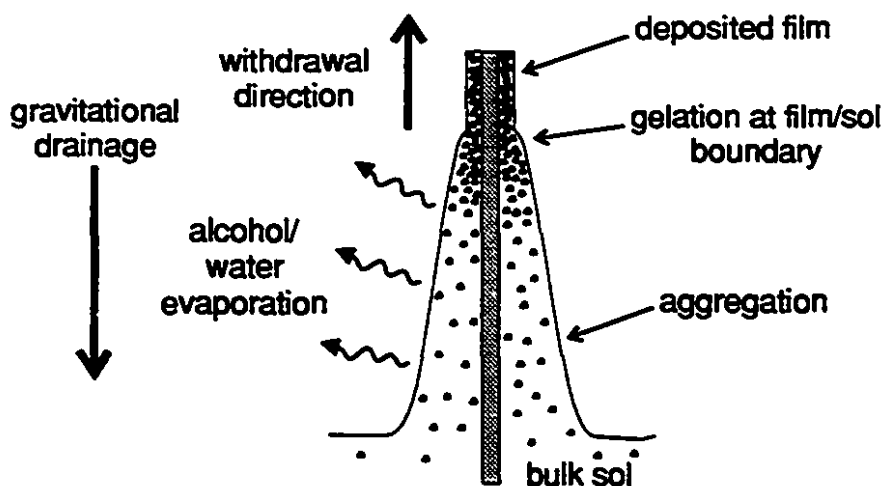
Figure 1.8 *The dip-coating process showing the many factors involved in film deposition*

Resulting film characteristics are dependent on many factors. Film thickness is governed by several competing forces including viscous drag upward on the liquid by the moving substrate, force of gravity, and surface tension gradient. During deposition, evaporation is primarily responsible for solidification of the film. The rate of evaporation is

16

dependent on the diffusion rate of vapour away from the film surface, which in turn is dependent on convection currents near the film surface, partial pressure of the volatile species, and deposition atmosphere. Deposition occurs as small polymeric particles that make up the dilute sol become highly concentrated, both due to gravitational draining and solvent evaporation, in the region near the boundary between film deposition and bulk solution. Condensation reactions are accelerated as the particles in the initially dilute sol are brought into close proximity. Viscosity dramatically increases and gelation occurs in seconds to minutes as opposed to hours to days with bulk gels.

Once cast, the film was placed in the oven to dry at 100°C for 30 minutes. Films were then exposed to UV light from a 100 W Hg arc lamp (Oriel Corp.) with a water filter to remove infrared radiation. Exposure times ranged from 1 to 60 minutes. The film was placed in a sample holder where the entire film was illuminated. After UV exposure for the desired length of time, the sample was removed from the holder and thermally treated for 60 minutes at temperatures selected from 80 to 140°C. This step enhanced the refractive index change and hardened the film.

MTMS sol-gel films were prepared by spin-coating on a photoresist spinner (Headway Research Inc., Garland, TX). The substrate was positioned flat on the rotatable chuck where a weak vacuum held it in place. The sol was passed through a 0.2 μm filter and deposited onto the substrate which was then spun at 2500 rpm for 120 seconds. Films were then baked for 12 hours at 100°C.

17

1.2.4. UV-Visible Absorption Spectroscopy

UV-visible absorption spectra were recorded with a Hewlett Packard 8452A diode array spectrophotometer over the wavelength range of 200 to 800 nm. Spectra were collected from the ormocer sol and were imported into GRAMS spectral analysis software (Galactic Industries, Salem, NH) where spectral processing was performed.

1.2.5. Fourier Transform Infrared (FTIR) Spectroscopy

Infrared spectra were collected with a Bruker IFS-48 Fourier transform infrared spectrometer, in the range of 400 to 5000 cm^{-1}. The data acquisition software used was OPUS (Version 2.0) running under Operating System 2 (OS/2). Spectral processing was performed in GRAMS.

1.2.6. Raman Spectroscopy

Raman spectra were collected on a system purchased from Instruments SA, Inc., consisting of a Jobin Yvon THR640 asymmetric Czerny-Turner single monochromator equipped with a UV-enhanced CCD detector. The laser excitation source was a Spectraphysics argon ion laser ($\lambda = 514.5$ nm). Data-acquisition software used was Prism software, Version 1.0 (Instruments SA, Inc.). Spectral processing was performed in GRAMS.

1.2.7. Film Thickness Measurements

Film thickness was measured on a Dektak® 3030ST surface profiler (Veeco Instruments Inc., Santa Barbara, CA) where a stylus scans the surface across the edge of the film to measure the step height between the bare substrate and the adjacent film.

1.2.8. Refractive Index Measurements

Refractive index measurements were performed using the prism coupling method.[34] Fig. 1.9 schematically shows the principle of prism coupling.
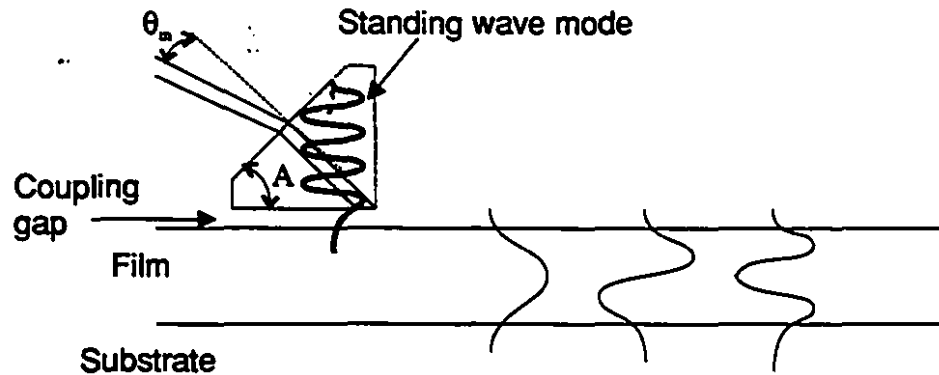
Figure 1.9 Principle of prism coupling

A prism with refractive index $n_p > n_{wg}$ is pressed onto the film. A small gap of air may be present between the base of the prism and the film due to surface irregularities and dust. A HeNe laser beam ($\lambda = 0.6328$ μm) directed onto the face of the prism is totally internally reflected at the prism-air gap interface and a standing wave mode develops. If the gap is small enough, the evanescent tail of this mode penetrates into the surface of the film. When the propagation constant in the z-direction, β_p, for this prism mode matches one of the propagation constants for an allowed mode in the waveguide, β_m, coupling of energy

19

occurs from the prism mode to the waveguide mode. This is often referred to as optical tunneling. The mth mode in the waveguide can be selected by changing the incident angle θ_m. Effective indices for each mode, N_m, are then calculated from the coupling angles (θ_m) according to Eqn. 1.10[32]:

$$N_m = n_p \sin\left\{\sin^{-1}\left(\frac{\sin\theta_m}{n_p}\right) + A\right\}$$
(1.10)

where A is the base angle of the prism.

1.3. Results and Discussion

1.3.1. Ormocer

The main reagents used to synthesize the ormocer sol-gel glass are shown in Fig. 1.10.
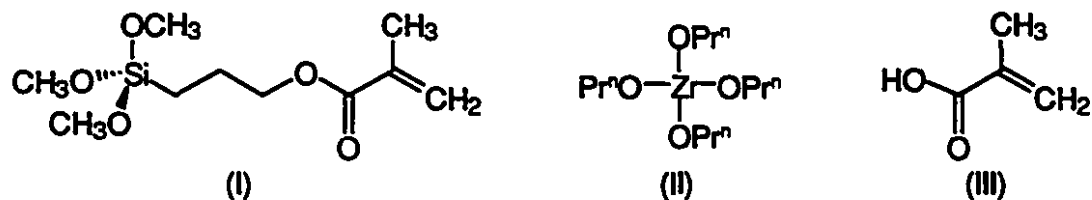
Figure 1.10 *Reagents used to synthesize the ormocer sol-gel*

MAPTMS (I) is the primary network forming component. It not only provides an inorganic framework, but the organic substituent also adds flexibility to the resulting glass, which helps prevent cracking. The methacryloxy group is photopolymerizable, allowing the formation of a secondary organic network on exposure to ultraviolet light. Zirconium (IV), which has a high polarizability, is added as $Zr(OPr^n)_4$ (II) to increase the refractive

index of the glass and provide mechanical stability. It is homogeneously incorporated into the sol-gel probably by complexation with MAA (III). This decreases the rate at which the $Zr(OPr^n)_4$ hydrolyzes, effectively preventing precipitation of ZrO_2. MAA is also photopolymerizable and is incorporated into the organic network on exposure to UV light.

The first addition of HCl to MAPTMS amounts to one half the theoretical quantity necessary to hydrolyze all methoxy groups in MAPTMS. Since there are three moles of methoxy groups for each mole of MAPTMS, and one water molecule is produced in the condensation reaction for each water molecule added, 1.5 moles of water is theoretically sufficient for complete hydrolysis. With half of this amount, 0.75 moles, the MAPTMS only undergoes partial hydrolysis and little, if any condensation. Unlike most sol-gel reactions, no solvent is used in this hydrolysis reaction. Silicon alkoxides and water are immiscible and usually a mutual solvent is used to homogenize the solution and allow the components to react. Tetraalkoxysilanes in particular, which have been studied in the greatest detail, are extremely slow to react unless a solvent is used. Alkyl substitution of the siloxane increases the electron density on Si and stabilizes the positively charged transition state in the hydrolysis reaction. Under acidic conditions, the hydrolysis rate is therefore increased. Initially, the MAPTMS and HCl are immiscible; however, within about 10 minutes the hydrolysis reaction has proceeded far enough to produce enough methanol to act as the solvent for the unreacted HCl and MAPTMS and the solution is homogenized. Metal alkoxides readily form complexes with carboxylic acids,[35] and addition of the Zr/MAA complex at this stage should promote heterocondensation reactions between silanol groups and unhydrolyzed propoxide groups on Zr.

21

The second addition of water to the sol is performed to complete the hydrolysis of the remaining methoxide and propoxide groups of MAPTMS and the Zr/MAA complex respectively. This amount is made up of the further 0.75 mol water/mol MAPTMS as well as 1.5 mol water/mol $Zr(OPr^n)_4$. Since the formation of the Zr/MAA complex generates one molecule of propanol, there are three propoxy groups remaining on each zirconium. 1.5 moles of water are again theoretically sufficient for hydrolysis. This makes up the remaining portion of the second water addition.

Transition metal alkoxides generally hydrolyze very rapidly, leading to uncontrolled condensation reactions and precipitates. Performing the hydrolysis of the Zr/MAA complex in the presence of prehydrolyzed MAPTMS avoids unwanted precipitation of ZrO_2. Instead, zirconia-methacrylate colloids are formed following hydrolysis and condensation of the Zr/MAA complex. Schmidt and Krug report that wide angle x-ray scattering (WAXS) measurements on this material show particle sizes of about 2 nm for these colloids.[36] Since they could not prove the existence of Zr-O-Si bonds, they propose a model for the unpolymerized system with zirconia-methacrylate colloids dispersed throughout a siloxane network. On polymerization of the methacrylate groups, the colloids become attached to the siloxane backbone. The model is shown in Fig. 1.11.
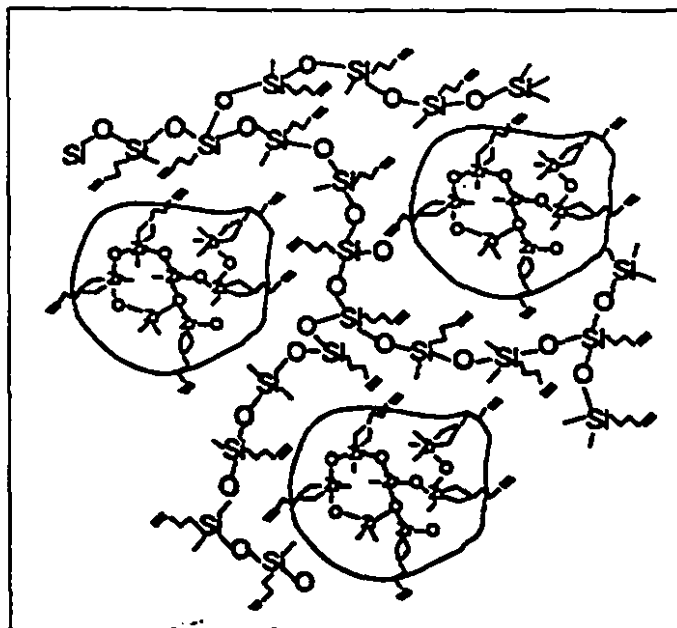
Figure 1.11 *Model of zirconia-methacrylate colloids dispersed throughout a siloxane network*

The sol is pale yellow due to the $Zr(OPr^n)_4$ which is yellow in colour. The colour is due to a tailing absorption beyond 380 nm as shown in Fig. 1.12.
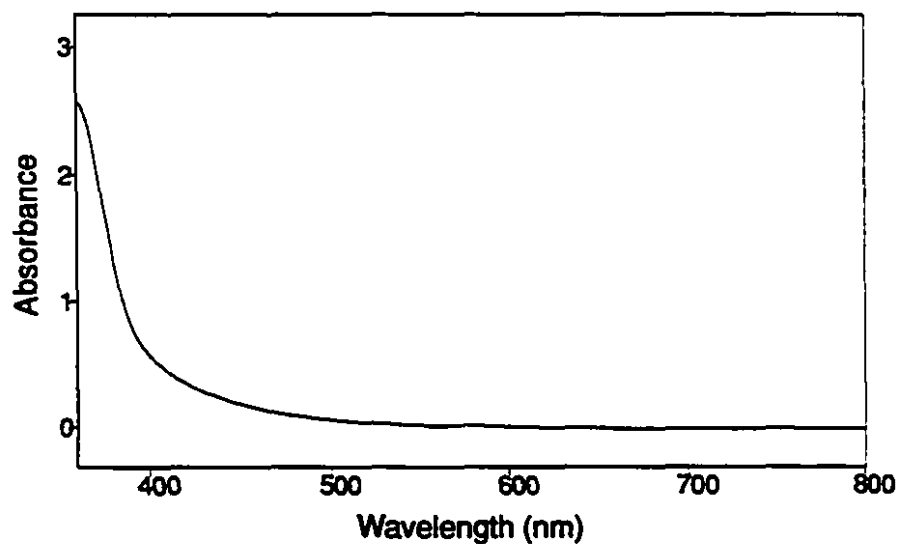
Figure 1.12 *UV-vis absorption spectrum of the ormocer sol*

The sol is stable for several months if stored in a sealed container so that solvent is not allowed to evaporate. The viscosity does nevertheless increase somewhat with time due to condensation reactions which continue slowly.

1.3.2. MTMS

The MTMS sol-gel system was synthesized to be a possible host for erbium complexes. The reasons for choosing this material were: (1) it produces crack-free films and bulk samples, (2) it can accommodate relatively high concentrations of dopants, and (3) it allows rapid fabrication of samples. Cracking of sol-gel films normally occurs due to the severe contraction of the rigid gel as the hydrolysis and condensation products (alcohol and water) are expelled during cross-linking. Maintaining a low volume of reactants helps avoid cracking in sol-gel films since this decreases the volume contraction in the glass. In this sol-gel, the molar ratio of water to MTMS (r-value) is 1.5. Although this is theoretically sufficient for complete hydrolysis of the three methoxy groups on MTMS, it does leave some unhydrolyzed methoxy groups. A higher r-value would lead to more complete hydrolysis and condensation, but would increase the volume of reactants to an extent that might cause films to crack.

Phase separation is a problem that often occurs when using a low r-value. Instead of obtaining a uniform distribution of partially hydrolyzed intermediates, about half the molecules are almost completely hydrolyzed, whereas the remaining half are almost unreacted. This occurs because of preferential attack by water on a siloxane monomer that has already been hydrolyzed once. A solution to this problem is to raise the temperature.

24

This overcomes the activation energy for the water to attack fully unhydrolyzed siloxanes, resulting in a more uniform distribution of partially hydrolyzed species (a kinetic solution to an otherwise thermodynamically driven reaction). Another effect of increasing the temperature is that the resulting sol is much more viscous because of the distillation of methanol. This is an advantage in further reducing the volume, allowing casting of films at a low degree of condensation. Overall, this permits the polymeric chains to rearrange and allow some stress-relaxation during alcohol evaporation.

1.3.3. FTIR

The sol-gels were further characterized by FTIR. Spectra are presented in Figs. 1.13 (ormocer) and 1.14 (MTMS glass). Tables 1.1 and 1.2 give observed frequencies and assignments for both materials, respectively. The ormocer spectrum shows a very prominent peak at 1720 cm^{-1} from the carbonyl, and at 1639 cm^{-1} from the vinyl group, both belonging to the methacryate group. The slightly broad peak at 1550 cm^{-1} is assigned to the C-O stretch in the Zr/MAA complex. The assignment is made based on reported vibrations for C-O stretching in $Cu(acac)_2$, which also exhibits bidentate chelation through oxygen.[37] The spectrum also contains several overlapping peaks between about 1200 and 900 cm^{-1}. The band profile in this region indicates Si-O stretching modes. Materials containing SiO_2 generally show two very distinguishable peaks at 1080 cm^{-1} and 1220 cm^{-1} due to the Si-O-Si asymmetric stretch.[1] Accordingly, we assign the broad intense absorption in Fig. 1.13 in the range 1000 - 1200 cm^{-1} to v_{Si-O}. The MTMS

spectrum is much less complicated than that of the ormocer. Again, we assign the broad

absorption between 1000 - 1200 cm^{-1} to ν_{Si-O}.
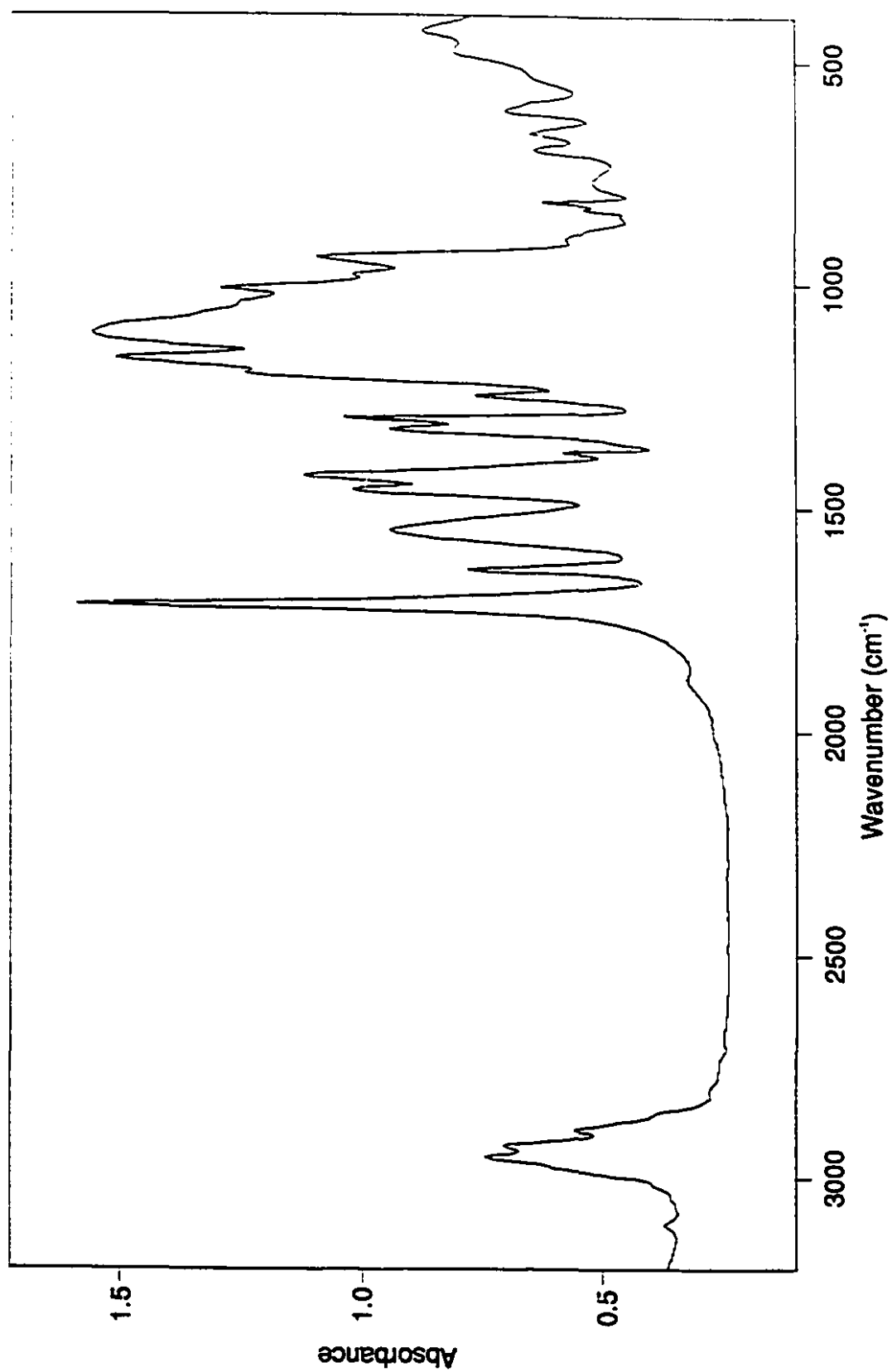
Figure 1.13 FTIR spectrum of the ormocer sol-gel (KBr disk)

27

Table 1.1 *Observed vibrational frequencies (cm^{-1}) and assignments for the ormocer sol-gel[a]*

Ormocer	Assignment[b]
3421 b	ν (O-H)
2955 m	ν_{as} (C-H)
2893 w	ν_s (C-H)
1720 vs	ν (C=O)
1639 m	ν_{as} (C=C)
1550 m	ν (C=O) $\left(-\overset{\mid}{\underset{\mid}{Zr}}\overset{O}{\underset{O}{\diamond}}C-\right)$
1460 m	δ_{as} (CH$_2$)
1429 m	δ_{as} (CH$_3$)
1375 w	δ_s (CH$_3$)
1323 m	
1298 m	
1248 m	
1200 sh	δ_s (Si-CH$_2$)
1169 s	ν (C-C(=O)-O)
1115 s	
1011 s	
980 m	ν (Si-O(H))
941 s	
899 w	
831 w	
816 w	
770 b	
696 w	
662 w	
611 m	
528 sh	
474 sh	δ(Si-O-Si)
428 m	

[a]Abbreviations used for band descriptions: vs, very strong; s, strong; m, medium; w, weak; sh, shoulder; b, broad.
[b]Vibrational mode descriptions: ν, stretching; δ, bending; as, asymmetric; s, symmetric.

28
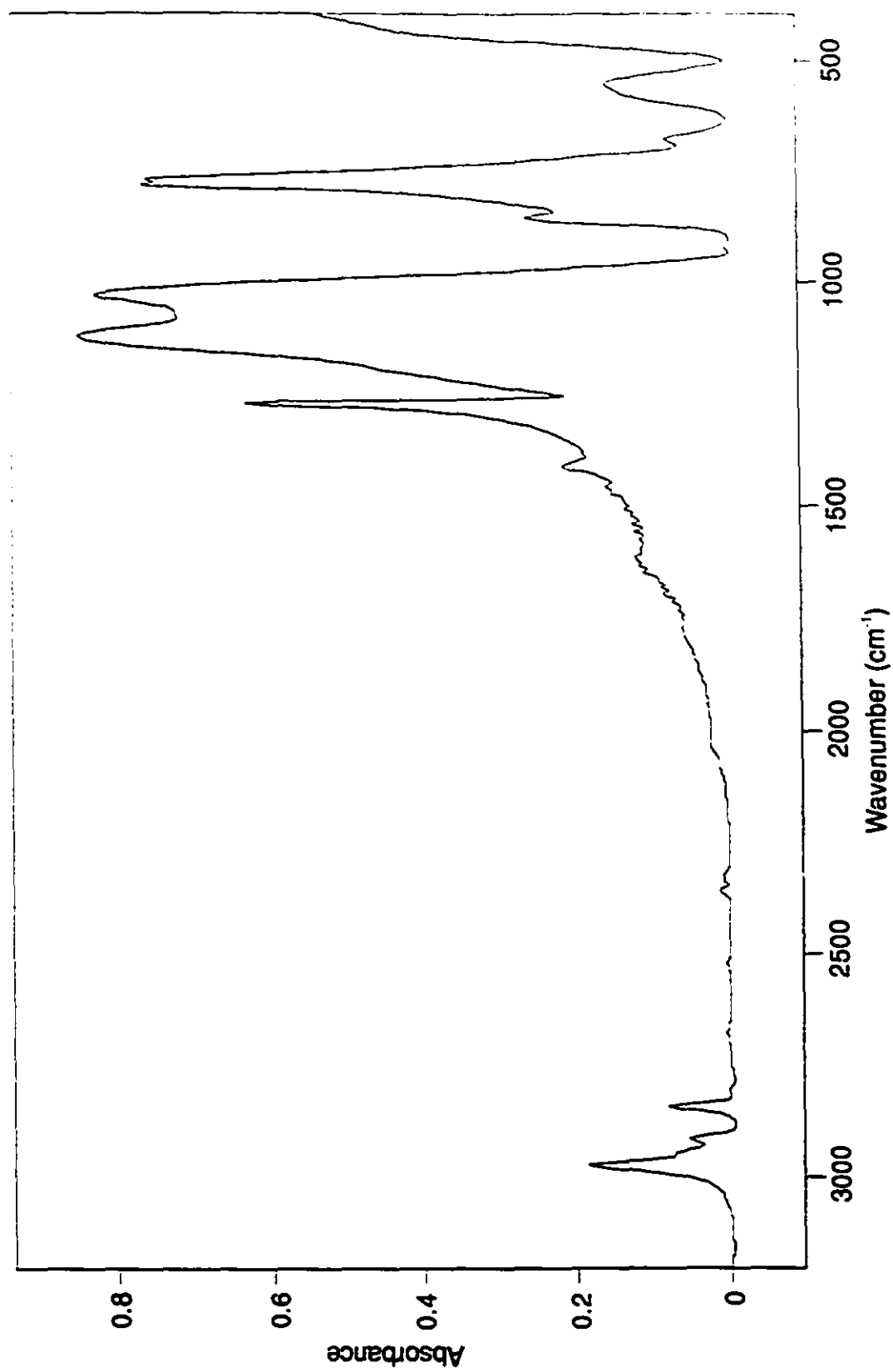
Figure 1.14 FTIR spectrum of the MTMS sol-gel (KBr disk)

29

Table 1.2 *Observed vibrational frequencies (cm⁻¹) and assignments for the MTMS sol-gel[a]*

MTMS Sol-gel	Assignment[b]
3444 b	v (O-H)
2974 m	v_{as} (C-H)
2916 w	v_s (C-H)
2843 w	v_s (C-H) Si-OCH₃
1412 m	δ_{as} (CH₃)
1275 s	δ_s (CH₃)
1122 vs	
1028 vs	
920 vw	
854 m	v_s (Si-O-C)
773 s; d	δ_s (CH₃)
679 w	
554 m	

[a]Abbreviations used for band descriptions: vs, very strong; s, strong; m, medium; w, weak; vw, very weak; sh, shoulder; b, broad; d, doublet.
[b]Vibrational mode descriptions: v, stretching; δ, bending; as, asymmetric; s, symmetric.

1.3.4. Photopolymerization

Photopolymerization of the vinyl groups in the ormocer was followed by Raman spectroscopy. Fig. 1.15 clearly shows a decrease in the intensities of the bands associated with the vinyl groups (i.e., the alkene C-H asymmetric stretch at 3105 cm⁻¹ and the C=C stretch at 1640 cm⁻¹) on exposure to UV light.
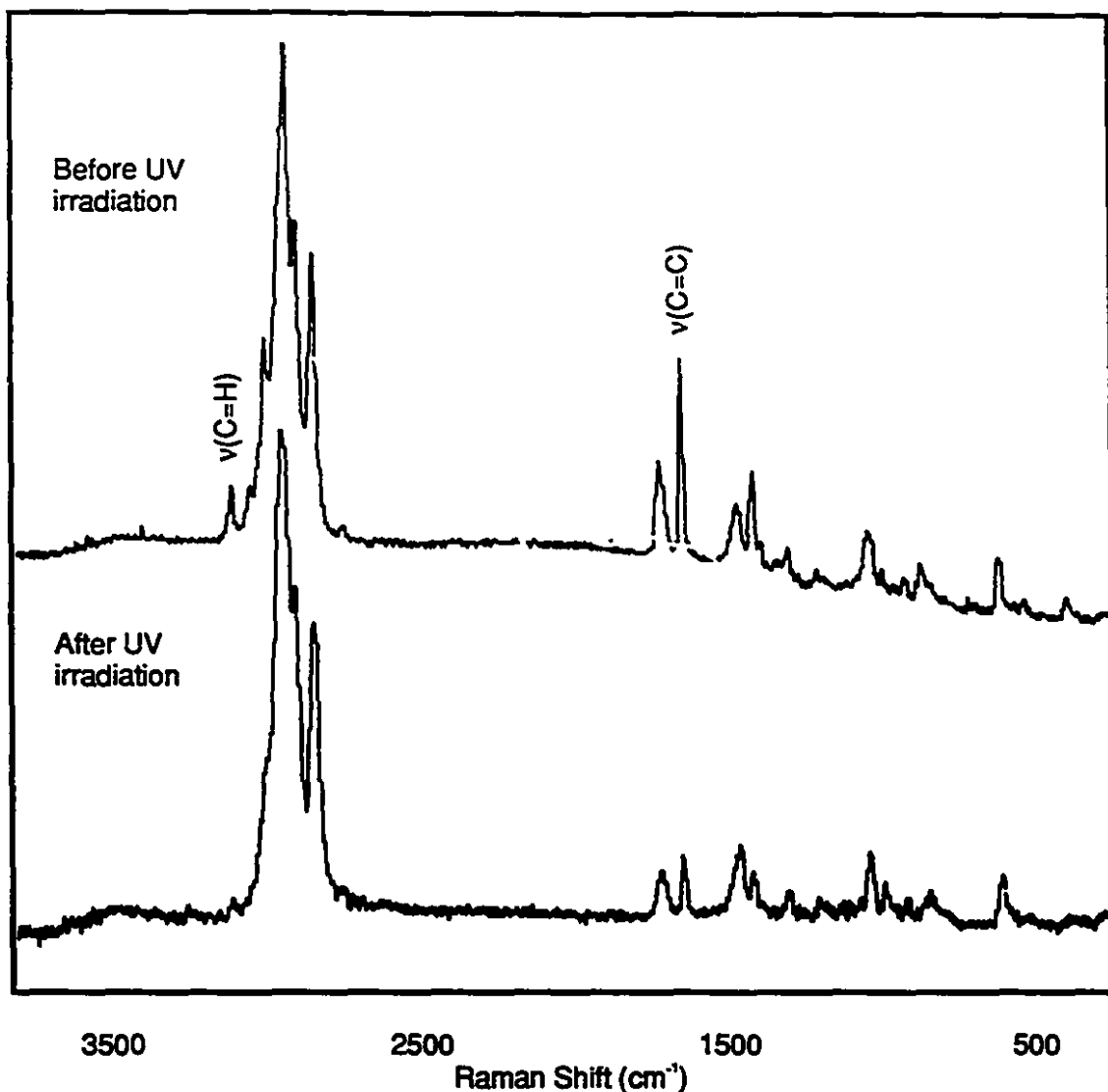
Figure 1.15 *Raman spectrum of ormocer sol before and after exposure to UV light*

In order for the photopolymerization reaction to occur efficiently, a photoinitiator must be present. We used 1-hydroxycyclohexyl-1-phenylketone which is excited to the triplet state when exposed to UV light. It then undergoes α-cleavage to produce benzoyl and 1-hydroxycyclohexyl radicals.

31
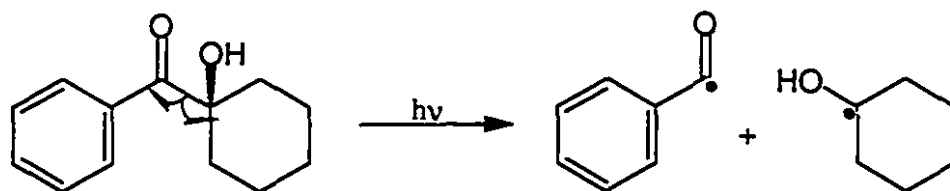
Figure 1.16 Radicals produced from α-cleavage of 1-hydroxycyclohexyl-1-phenylketone

The benzoyl radical is primarily responsible for initiation of the polymerization process. Fig. 1.17 shows the addition of the benzoyl radical to the methacrylate group.
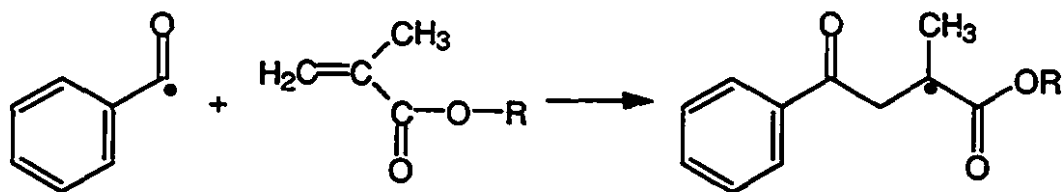
Figure 1.17 Addition of benzoyl radical to methacrylate group

There is some evidence[38] that the 1-hydroxycyclohexyl radical is also involved in the photoinitiation of acrylate polymerizations and Fig. 1.18 shows the addition of this radical to the methacrylate group.
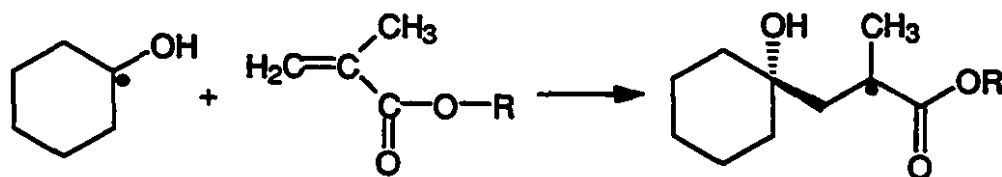
Figure 1.18 Addition of 1-hydroxycyclohexyl radical to methacrylate group

The refractive index of the ormocer increases on exposure to UV light. This may be due to the polymer network filling in voids within the inorganic network. Sol-gels are porous materials, and an organic polymer can form within these pores and densify the structure. Since refractive index is not just a function of polarizability, but also of volume concentrations of polarizable entities, then it is reasonable to suggest that a denser structure should have a slightly higher refractive index.

1.3.5. Films

The ormocer sol-gel produced good quality homogeneous films in one step by the dip-coating process. As can be seen in Fig. 1.19 the film thickness depends linearly on drawing speed. Thus, excellent control over film thickness was achieved.
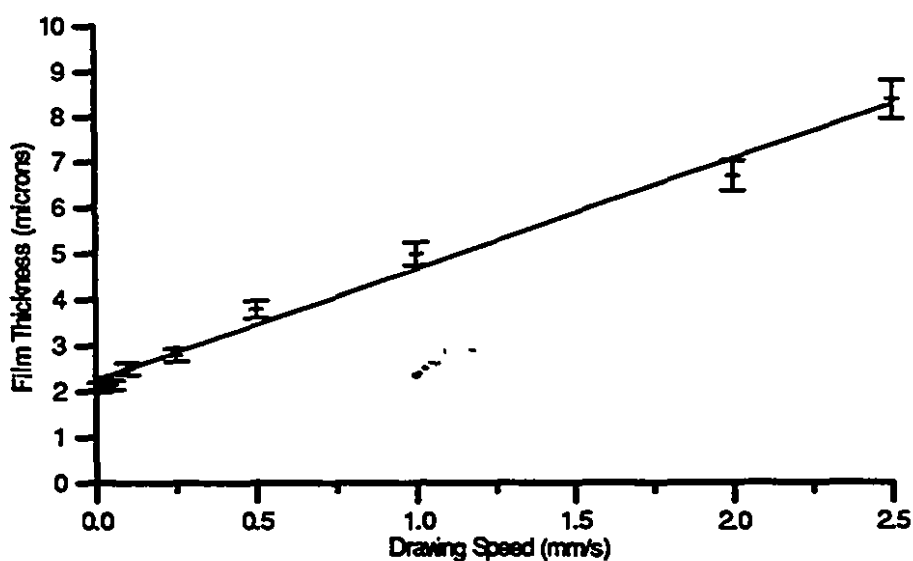
Figure 1.19 Variation of film thickness with drawing speed

These results were reproducible for sols that had not aged significantly. After about a week, sols became more viscous and thicker films resulted from the same drawing speeds.

The refractive index of the films as cast was measured to be 1.518 at $\lambda = 0.6328 \mu m$. Exposure of the films to UV light for up to 60 minutes increased the refractive index. Fig. 1.20 shows the change in refractive index with UV exposure time.
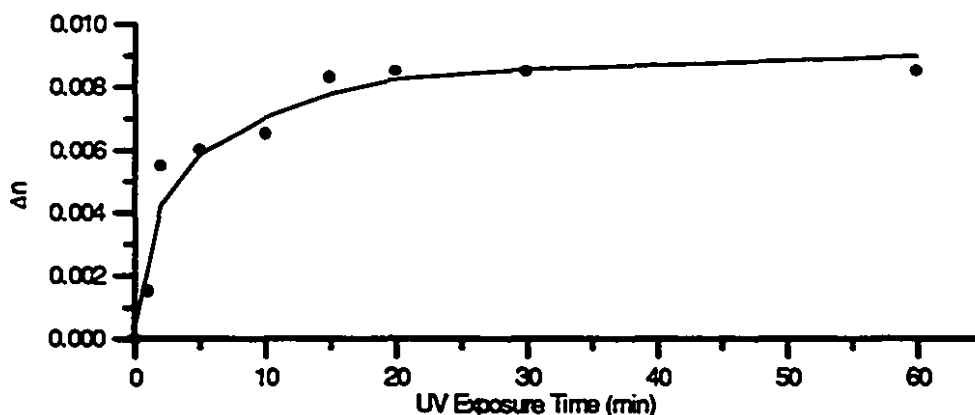
Figure 1.20 Change in refractive index with UV exposure time (the line is a guide to the eye)

As can be seen from Fig. 1.20, the maximum refractive index change occurred after about 20 minutes. Beyond this exposure time, no discernible change was measured.

The effect of postbaking on refractive index change was also investigated. Temperatures between 80 and 140°C for 60 minutes were used for different UV exposure times. Fig. 1.21 displays the results.
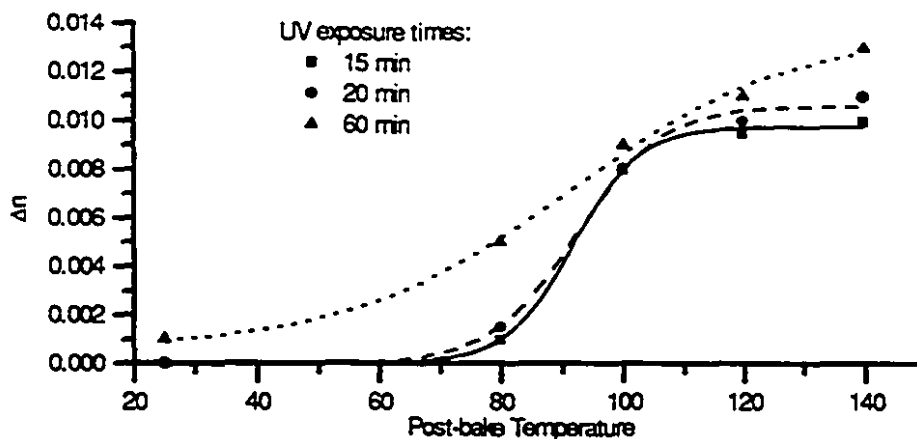
Figure 1.21 Change in refractive index with postbaking temperature

Films baked below ~100°C showed low mechanical stability as evidenced by the fact that they were easily scratched. Some films baked at 140°C showed cracks, thus the best postbaking temperatures were determined to be between 100 and 120°C.

MTMS films were not investigated in great detail. They did produce homogeneous, crack-free films with thicknesses in the range of 10 to 12 μm. Precise control of thickness was difficult since this is strongly dependent on the viscosity of the sol. The viscosity, in turn, is strongly dependent on the amount of methanol which evaporates during the reaction. Better control of reaction conditions, such as gravimetric monitoring of methanol evaporation, should lead to better reproducibility of film thickness.

35

1.4. Conclusions

The combination of complexing $Zr(OPr^n)_4$ with MAA and the addition of this complex to a prehydrolyzed siloxane prevented precipitation of large particles of ZrO_2 in the ormocer sol-gel. Photopolymerization of the ormocer sol was followed by Raman spectroscopy and the spectra clearly show a decrease in the bands associated with the vinyl groups ($\nu(C=C)$ and the alkene $\nu(C-H)$). This indicated the polymerization of the methacrylate groups does indeed occur. Ormocer films produced by dip-coating were of very good quality, and film thicknesses were accurately controlled from 2 to 8 μm by varying the withdrawal speed of the substrate from the sol. Refractive index of these films increased after exposure to UV light due to polymerization of the methacryl groups. A maximum Δn was obtained after about 20 minutes exposure. Post-baking also induces a refractive index change, with the best temperatures being between 100 and 120°C. The MTMS sol also produced good quality films and is potentially a good host for erbium.

1.5. References

1. C.J. Brinker and G.W. Scherer. *Sol-Gel Science*. Academic Press, San Diego, 1990.

2. L. Klein, Sol-Gel Coatings, In *Thin Film Processes II*, Academic Press, Boston, 1991.

3. M.W. Ellsworth and B.M. Novak, *Chem. Mater.*, 5, 839, (1993).

4. S.S. Prakash, C.J. Brinker, A.J. Hurd and S.M. Rao, *Nature*, 374, 439, (1995).

5. L.M. Ellerby, C.R. Nishida, F. Nishida, S.A. Yamanaka, B. Dunn, J.S. Valentine and J.I. Zink, *Science*, 255, 1113, (1992).

6. S. Wu, L.M. Ellerby, J.S. Cohan, B.Dunn, M.A. El-Sayed, J.S. Valentine and J.I. Zink, *Chem. Mater.*, 5, 115, 1993.

7. S.A. Yamanaka, B. Dunn, J.S. Valentine and J.I. Zink, *J. Am. Chem. Soc.*, 117, 9095, (1995).

8. P. Audebert and C. Demaille, *Chem. Mater.*, 5, 911, (1993).

9. R. Zusman, C. Rottman, M. Ottolenghi and D. Avnir, *J. Non-Cryst. Solids*, 122, 107, (1990).

10. A. Slama-Schwok, D. Avnir and M. Ottolenghi, *J. Phys. Chem.*, 93, 7544, (1989).

11. D. Levy, S. Einhorn and D. Avnir, *J. Non-Cryst. Solids*, 113, 137, (1989).

12. D. Levy, C.J. Serna, A. Serrano, J. Vidal and J.M. Oton, *Sol-Gel Optics II, SPIE Proc.*, 1758, 476, (1992).

13. E.T. Knobbe, B. Dunn, P.D. Fuqua and F. Nishida, *Appl. Optics*, 29, 2729, (1990).

14. J.M. McKiernan, S.A. Yamanaka, B. Dunn and J.I. Zink, *J. Phys. Chem.*, 94, 5652, (1990).

15. R.B. Lessard, K.A. Berglund and D.G. Nocera, *Mat. Res. Soc. Symp. Proc.*, 155, 119, (1989).

16. W. Xu, S. Dai, L.M. Toth, G.D., Del Cul and J.R. Peterson, *J. Phys. Chem.*, 99, 4447, (1995).

17. T. Fujiyama, M. Hori and M. Sasaki, *J. Non-Cryst. Solids*, **121**, 273, (1990).

18. Y. Zhang, P.N. Prasad and R. Burzynski, *Chem. Mater.*, **4**, 851, (1992).

19. Y. Nosaka, N. Tohriiwa, T. Kobayashi and N. Fujii, *Chem. Mater.*, **5**, 930, (1993).

20. M. Yamane, T. Takada, J. Mackenzie and C. Li, *Sol-Gel Optics II, SPIE Proc.*, **1758**, 577, (1992).

21. H.W. Oviatt, K.J. Shea, S. Kalluri, Y. Shi, W.H. Stier and L.R. Dalton, *Chem. Mater.*, **7**, 493, (1995).

22. J. Kim, J.L. Plawsky, E.V. Wagenen and G.M. Korenowski, *Chem. Mater.*, **5**, 1118, (1993).

23. L. Kador, R. Fischer, D. Haarer, R. Kasemann, S. Bruck, H. Schmidt and H. Durr, *Adv. Mater.*, **5**, 270, (1993).

24. B.E. Yoldas and D.P. Partlow, *Thin Solid Films*, **129**, 1, (1985).

25. T. Kitigawa, F. Bilodeau, B. Halo, S. Theriault, J. Albert, D.C. Jihnson, K.O. Hill, K. Hattori and Y. Hibino, *Elect. Lett.*, **30**, 1311, (1994).

26. J.D. Mackenzie, *Sol-Gel Optics, SPIE Proc.*, **1328**, 2, (1990).

27. B.M. Novak, *Adv. Mater.*, **5**, 424, (1993).

28. J.C. Pouxviel, J.P. Boilet, S. Sanger and L. Huber, In *Better Ceramics Through Chemistry*, C.J. Brinker, D.E. Clark and D.R. Ulrich, Eds., North-Holland, New York, p. 269, 1984.

29. B.E. Yoldas, *J. Mat. Sci.*, **14**, 1843, (1979).

30. A.B. Buckman, *Guided Wave Photonics*, Saunders College Publishing, Orlando, 1992.

31. R.G. Hunsperger, *Integrated Optics: Theory and Technology*, Springer-Verlag, Berlin, 1991.

32. H. Krug, F. Tiefensee, P. William Oliveira and H. Schmidt, *Sol-Gel Optics II, SPIE Proc.*, **1758**, 448, (1992).

33. Y. Haruvy and S.E. Webber, *Chem. Mater.*, **3**, 501, (1991).

34. *Introduction to Glass Integrated Optics*, S.I. Najafi, Ed., Artech House, Boston, 1992.

35. D.C. Bradley, R.G. Mehrotra and D.P. Gaur, *Metal Alkoxides*, Academic Press, London, 1978.

36. H. Schmidt and H. Krug, In *Inorganic and Organometallic Polymers II*, P. Wisian-Neilson, H.R. Allcock and K.J. Wynne, Eds., American Chemical Society, Washington, 1994.

37. H.A. Szymanski and R.E. Erickson, *Infrared Band Handbook, Vol. 1*, IFI/Plenum Data Corp., New York, 1970.

38. Phan, X.T.P., *J. Radiat. Curing*, **13**, 18, (1986).

2. Sol-Gel Integrated Optics Devices

2.1. Introduction

The goal of integrated optics is to realize the development of optical devices and systems on a single substrate, analogous to integrated electronics. Some applications of this technology include signal processing, computing, sensors and telecommunications.[1] Glass is a desirable material for fabricating these devices. It has excellent transparency, high threshold-to-optical damage ratio, thermal, mechanical, and chemical stability, and small coupling losses between silica waveguides and optical fibers.[2] In particular, silica based devices on silicon substrates have many advantages over other configurations.[3] Silicon technology is very well established and many of its facets can be applied to glass integrated optics. Silicon is available in cheap, large area substrates that permit fabrication of complex circuits or mass production of several simpler ones. Fiber-to-waveguide coupling can be accomplished using etched grooves in silicon. Perhaps most importantly, silicon can be used as a substrate for electronic, optoelectronic and waveguide components to make hybrid circuits.

Glass integrated optical devices have been fabricated by a number of different methods, including ion-exchange, flame hydrolysis deposition (FHD), plasma enhanced chemical vapour deposition (PECVD), low pressure chemical vapour deposition (LPCVD), and sputtering. Each of these methods has their own advantages in terms of quality and performance of the resulting devices. However, they all require expensive equipment, high temperature processing and labour intensive fabrication. Devices made by

the sol-gel process can be fabricated inexpensively at low temperatures in relatively few steps.

In fabricating any device, there are certain materials related criteria that must be met. Table 2.1 illustrates a general strategy involved in the application of materials chemistry to device fabrication, while Table 2.2 presents these strategies applied to a particular device (e.g., directional coupler). These strategies apply to all the devices presented in this thesis.

Table 2.1 *Strategy for application of materials chemistry to meet device criteria*

Device Criteria	Materials Chemistry Considerations
compatibility with silicon substrates and optical fibers	use a silica based system
compatibility with optoelectronic devices	low temperature processing (<400°C)
low losses	optical transparency at operating wavelengths
facile processing into waveguides and devices	thin film properties; photolithography
device reliability	factors such as adhesion, mechanical, environmental stability ultimately under chemical control
doping with active materials	systematic chemical modification to achieve desired effect

Table 2.2 *Materials chemistry solutions to directional coupler criteria*

Directional Coupler Criteria	Materials Chemistry Solutions
compatibility with silicon and optical fiber technologies	use sol-gel process (low temperature) to make silica based materials
low losses	sol-gel glass
facile device fabrication	thick films in one step with organically modified sol-gel
	photoinscription (use photosensitive organic compounds in sol-gel synthesis)
mechanical stability	inorganic components (e.g., zirconium)

The system we have worked with allows device fabrication from start to finish in only four steps. These steps can be summarized as:

    I. sol-gel synthesis

    II. film deposition by dip-coating

    III. photolithographic inscription of device pattern by UV light

    IV. post-baking

By using this method, waveguides, directional couplers, beamsplitters and gratings were fabricated and characterized. In addition, an embossing technique was also used to make gratings. In this case, a surface relief pattern pressed into a deformable film is replicated.

42

2.2. Device Fabrication (General)

All devices were made from thin films of the photosensitive ormocer described in Chapter 1. Synthetic details will not be repeated here. Films were cast by the dip-coating technique on glass, fused silica, silicon or silicon with SiO_2 buffer layer. For devices fabricated by exposure of the film to UV light through a mask, films were placed in the oven at 100°C for 30 minutes after dip-coating. This dried the films, preventing them from sticking to the mask. A mask with the appropriate pattern was placed in contact with the film using the sample holder shown in Fig. 2.1. It contained a spring loaded support to ensure good contact between the mask and the film.
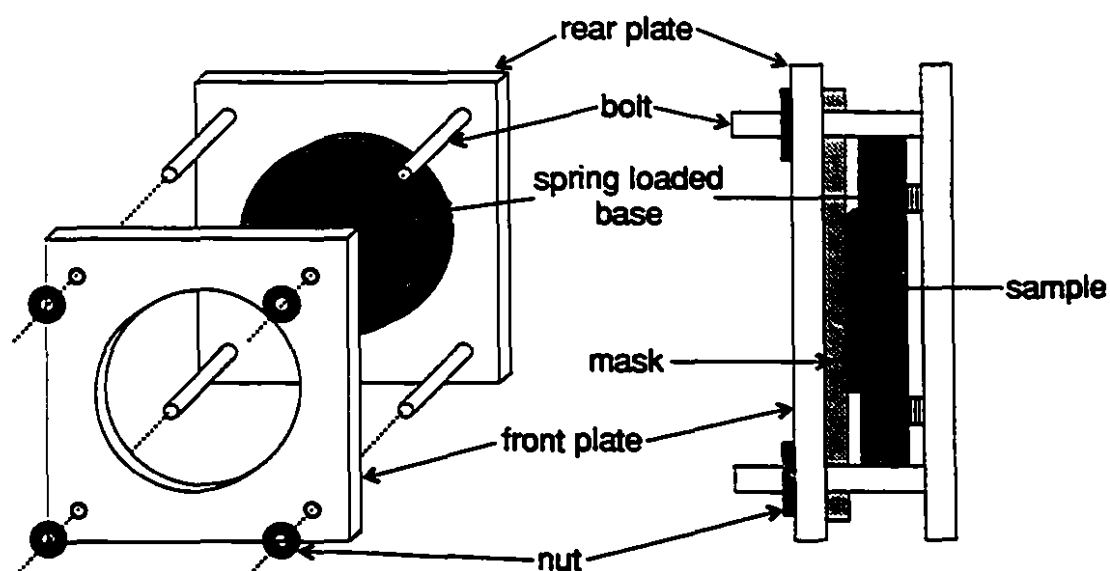
Figure 2.1 Sample holder used to expose films to UV light through a mask

Films were then exposed to UV light for varying lengths of time to define the devices. After UV exposure, the sample was removed from the holder and treated for 60 minutes at ~100°C to enhance the refractive index change and provide additional mechanical stability. Finally, the two ends of the sample were cleaved for optical testing.

43

Most devices were made in the above manner. Any differences to this procedure are noted in the **Fabrication** section for the particular device.

2.3. Waveguides

2.3.1. Introduction

Waveguides are the fundamental building blocks of any integrated optical device. Recall from Chapter 1, where we defined a waveguide as a dielectric medium which transports energy at wavelengths in the infrared and visible portion of the electromagnetic spectrum. Waveguides can be cylindrical fibers, planar laminates or channel structures.

Fiber   **Planar**   **Channel**
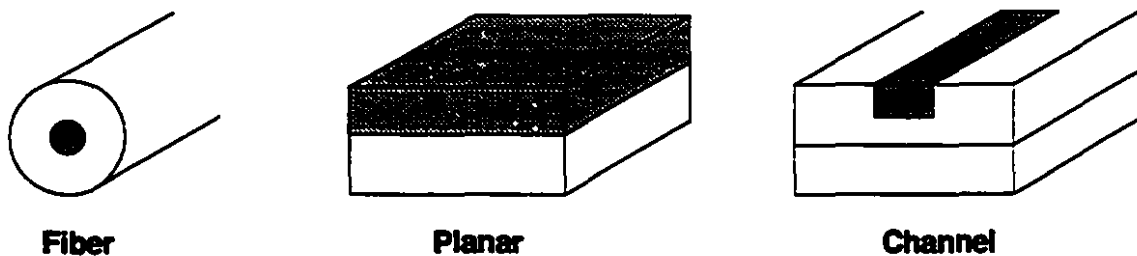
Figure 2.2 *Different waveguide forms*

Planar waveguides can be considered as one-dimensional since their index boundaries are only along one axis. Channel waveguides have index boundaries along two coordinate axes. This two-dimensional confinement allows the routing of optical signals between various components on a chip, much like a wire in an electronic circuit. Asymmetric waveguides (i.e., $n_3 \gg n_1$) are usually found in integrated optical circuits where a film of refractive index n_2 is deposited on a substrate with index n_3, surrounded by air with index n_1.

44

Recall also that light waves propagate through the waveguide in distinct modes with propagation constants β_m (for $m = 0,1,2....$). Waveguide dimensions, and refractive index differences between the waveguide and its surroundings, determine the modal properties.[4] For single mode operation, low refractive index differences (1 to 2%) demand dimensions on the order of one to several operating wavelengths. Higher differences (10 to 30%) require one-third to one-fourth the operating wavelength. If these dimensions are exceeded, the waveguides become multi-mode.

An important consideration in evaluating waveguide quality is attenuation, or equivalently, loss. The attenuation coefficient, α, describes these losses in a form given by:

$$\alpha = \frac{10\log(P_0/P_1)}{z_1 - z_0} \tag{2.1}$$

where P_o and P_1 are the optical power at points z_0 and z_1 along the waveguide. Units of α are dB/cm.

The two main loss mechanisms in glass waveguides are scattering and radiation.[5] All waveguides contain imperfections which lead to scattering. Surface scattering loss is particularly important since the zigzag manner in which light travels along the waveguide causes scattering at each reflection. Bulk scattering due to imperfections in the waveguide, including density fluctuations, is another loss channel. Both scattering mechanisms can lead to polarization scrambling and mode mixing. The fact that a streak is visible in a guiding layer indicates losses - the brighter the streak, the greater the losses. Radiation losses, where photons are emitted from the waveguide into the surrounding media, are important when waveguides are bent through a curve. Many channel waveguide devices

such as directional couplers, beamsplitters and Mach-Zender interferometers, have bends,

In addition, high optical component density on a single substrate requires the bending of

waveguides to guide light from one component to another.[6]

2.3.2. Fabrication of Waveguides

Planar waveguides were fabricated by exposing the entire film to UV light (i.e., no

mask was used). To make the channel waveguides, a mask with channel waveguide

patterns (containing 17 openings with widths ranging from 2 to 10 μm, increasing at

0.5 μm increments) was placed in contact with the film. Exposure times for both ranged

from 1 to 60 minutes. Postbaking was performed at temperatures ranging from 80 to

140°C for planar waveguides and was 100°C for channel waveguides.

2.3.3. Characterization

(a) Planar Waveguides

Details on film thickness and refractive indices as a function of UV exposure and

postbake temperature are given in Chapter 1 (Section 1.3.5) and are not repeated here.

(b) Channel Waveguides

A picture of a channel waveguide, 5 μm in width, viewed through an

optical microscope is shown in Fig. 2.3.
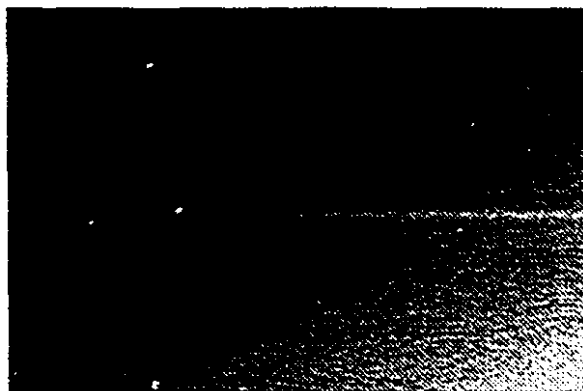
Figure 2.3 *Digitized optical microscope picture of channel waveguide*

Refractive index measurements of the waveguidewere performed using the prism coupling method. Results expressed in UV exposure time for channel waveguides made in 3.8 μm thick films are given in Fig. 2.4.
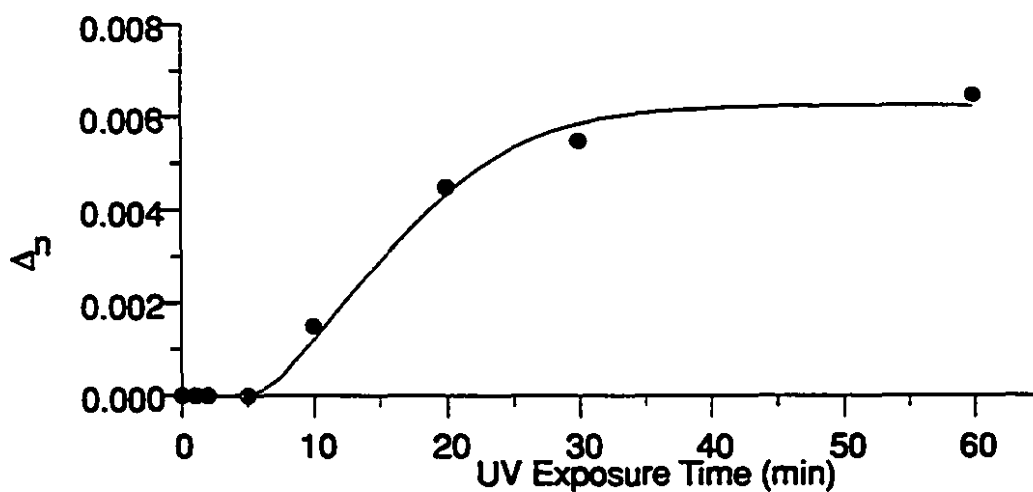
Figure 2.4 *Change in refractive index with UV exposure time for channel waveguides (the line is a guide to the eye)*

The curve characterizing the buried channel waveguides is somewhat different from that of the planar waveguides in Fig. 1.20. Here, there is a more gradual increase in refractive index change as exposure times increase in comparison with planar waveguides. Longer exposure times were necessary for maximal refractive index changes since the mask was made from glass that absorbed in the UV. An atomic force microscope (AFM) image of the channel waveguides is shown in Fig. 2.5.

As can be seen in Fig. 2.5, the waveguides are slightly raised relative to the unexposed regions of the film. This may lead one to believe that a ridge-type waveguide had been fabricated; however, this increase in thickness is only ~100 nm. Waveguides were analyzed using the beam propagation method (BPM),[7] a modelling tool for calculating the propagation of optical fields through waveguides and waveguide devices. The effective depth of the waveguides were determined to be ~3.5 μm from BPM. Thus, these waveguides are predominantly channel-type.
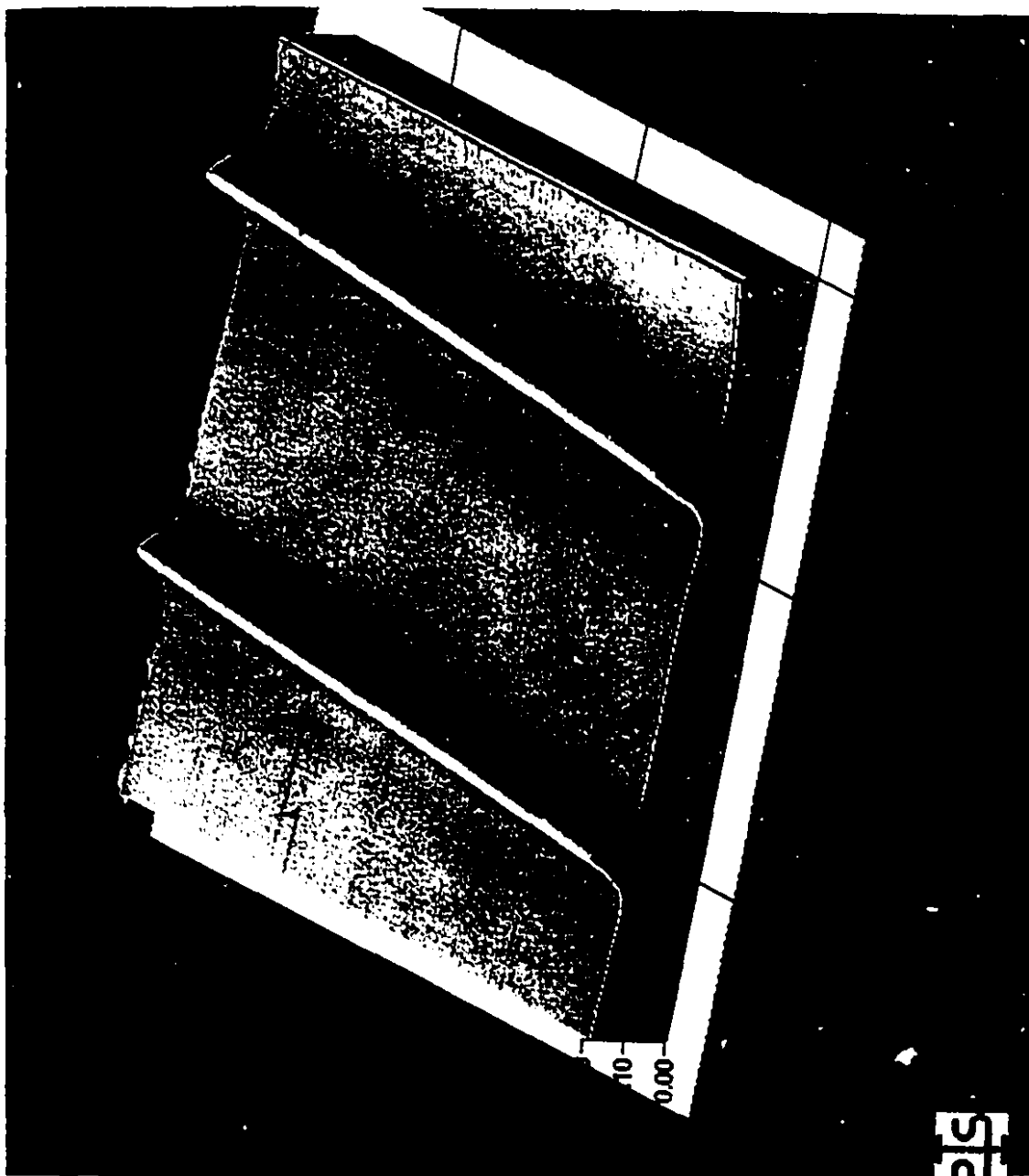
Figure 2.5 AFM image of channel waveguides

49

The waveguides guided light at $\lambda = 0.6328$ μm, but this was not always the case when a longer wavelength ($\lambda = 1.55$ μm) was used. Whether or not a waveguide can support modes and how many it can support at a given wavelength, λ_o, depends on the thickness of the waveguiding layer, d, and on n_1, n_2, and n_3. For an asymmetric waveguide where $n_3 \gg n_1$, the difference in refractive indices necessary for guiding is given by Eqn. 2.2[5]:

$$\Delta n = n_2 - n_3 \geq \frac{(2m+1)^2 \lambda_o^2}{32 n_2 d^2} \qquad (2.2)$$

For films thicker than 3.5 μm, Δn is quite small (~0.007) since this is just the difference in refractive indices between the exposed and non-exposed sol-gel. This is suitable for guiding at 0.6328 μm, but for guiding at 1.55 μm a greater Δn is necessary. This was accomplished by decreasing the film thickness to 3.5 μm, and the difference in refractive indices was then between the exposed sol-gel and the substrate thermaloxide, SiO_2. For a glass substrate with $n = 1.5115$, Δn was raised to 0.014. For a silicon substrate with an SiO_2 buffer layer with $n = 1.454$, Δn was raised to 0.071. These waveguide configurations are shown schematically in Fig. 2.6.

Figure 2.6 Different channel waveguide configurations for guiding at $\lambda=1.55$ μm

To test these waveguides, the samples were cleaved. Light at $\lambda = 1.55$ µm from a laser diode was then coupled into the waveguides via a single mode optical fiber. All waveguides ranging from 2 to 10 µm in width were able to guide at this wavelength. Light from the output of the 3 µm and 10 µm waveguides was focused onto a camera equipped with an infrared detector. Fig. 2.7 shows the mode profile of these guides. It can be seen that the 3 µm guide is single mode and the 10 µm guide exhibits two modes at $\lambda = 1.55$ µm.

Figure 2.7 *Digitized photograph showing mode profile of waveguides that are (a) 3 µm and (b) 10 µm in width*

Propagation losses were determined by the following procedure. Light was coupled into and out of the waveguide via optical fiber. A detector measured the intensity at the output and this was related to the input intensity by:

$$I_{out} = I_{in}(1-\alpha_p)(1-\alpha_c)^2 T_f \qquad (2.3)$$

where I_{out} is the output intensity, I_{in} is the input intensity, α_p is the propagation attenuation coefficient, α_c is the coupling attenuation coefficient and T_f is the fiber transmission (−1). The measurement was repeated, but this time instead of outcoupling with a fiber, the light

was focused by a microscope objective onto a detector. The intensity relationship in the latter case is:

$$I_{out2} = I_{in2}(1-\alpha_p)(1-\alpha_c)T_oT_f \qquad (2.4)$$

where T_o is the objective transmission (~0.8). T_f and T_o are both easily measured, and substituting for α_c in the above expressions allows the calculation of α_p.

For loss measurements at $\lambda = 1.55$ μm, a 3 μm single mode waveguide was selected. Losses were less than 0.3 dB/cm.

Another channel waveguide configuration was fabricated using a silicon substrate without an SiO_2 buffer layer. Silicon has a very high refractive index ($n = 3.85$) therefore a channel waveguide in a thin sol-gel film on a silicon substrate would not be able to guide light. Any light coupled into the waveguide would rapidly attenuate after a very short distance. Using the fact that the UV penetration depth is only ~3.5 μm, channel waveguides were fabricated in an 8 μm thick sol-gel film. This left a "buffer layer" of lower refractive index unexposed sol-gel which was ~4.5 μm in thickness. Fig. 2.8 shows a schematic of the waveguide configuration.

3.5 μm Waveguide

8 μm Sol-gel layer

Silicon
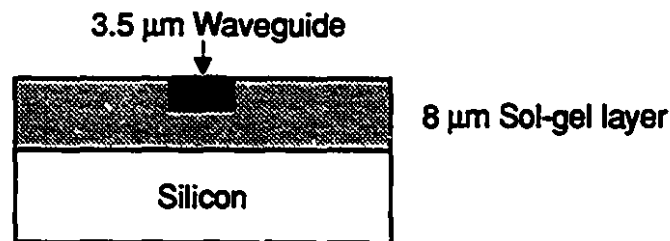
Figure 2.8 *Channel waveguide configuration utilizing "built-in" buffer layer*

To test the waveguides. light at $\lambda = 0.6328$ μm was coupled into each of the waveguides via an optical fiber. The transmitted light was focused and observed on a screen indicating that the built-in buffer layer was sufficiently thick to prevent light from radiating to the substrate. Depending on the width of the waveguides, two to four modes were observed. Propagation losses varied between 0.1 and 0.5 dB/cm. The testing set-up is shown in Fig. 2.9.
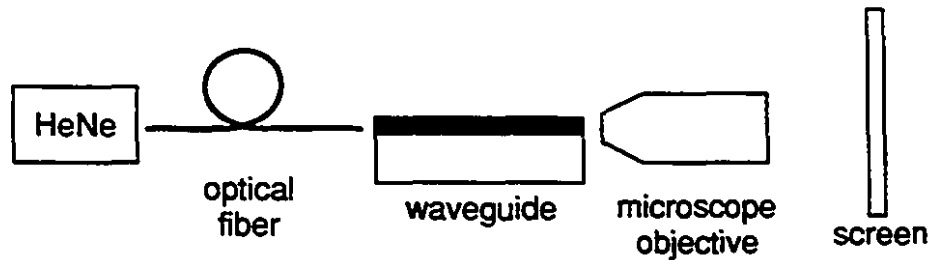
Figure 2.9 Set-up for testing of waveguides on silicon

The demonstration of this waveguide configuration is significant because it does not require the presence of a buffer layer on the silicon substrate. This removes one step in the fabrication of waveguides on silicon, contributing not only to a decrease in the period of time it takes to make a device, but also to a decrease in production cost.

53

2.4. Directional Coupler

2.4.1. Introduction

Guided light in integrated optical circuits can be divided or combined by use of directional couplers. Fig. 2.10 schematically shows a directional coupler.
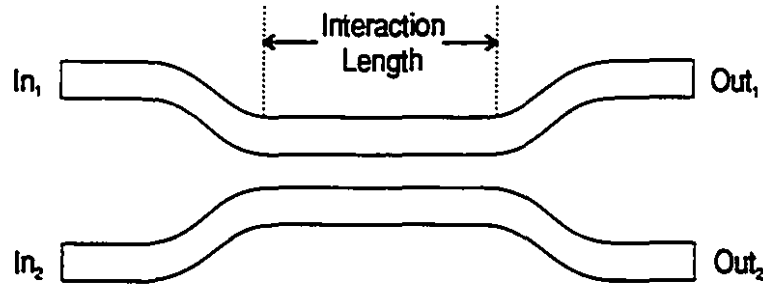
Figure 2.10 *Schematic of a directional coupler*

The principle of operation is as follows. Two identical channel waveguides placed in close proximity periodically exchange energy between themselves by optical tunneling. Energy transfer occurs by a process of synchronous coherent coupling between the overlapping evanescent tails of the guided modes in each waveguide. Energy propagating in one guide transfers to the other, then back again if the interaction length is sufficient. For this transfer to occur, the two guides must have identical propagation constants (i.e., $\Delta\beta = 0$). The distance required for complete energy exchange from one guide to the other, L_c (coupling length), is given by:

$$L_c = \frac{m\pi}{2\kappa} \qquad (2.5)$$

54

where κ is the coupling coefficient (depends on the degree of overlap of the guided wave fields), and $m = 0,1,2,...$ The power division ratio between the two output ports is given by:

$$\frac{P_1}{P_1 + P_2} = \cos^2\left(\frac{\pi z}{2L_c}\right) \tag{2.6}$$

where P_1 is the power remaining in the input guide, P_2 is the power transfered to the second guide and z is the interaction length. Symmetrical directional couplers, such as the one shown in Fig. 2.9, are used primarily as power dividers[8] and dual-wavelength division multi/demultiplexers (WDM)[9]. As a power divider, its function is to split a guided wave into two parts of lesser power which are then routed to another destination. By tailoring device design (e.g., interaction length, waveguide separation in coupling region), the coupler can be used to divide power at any ratio. As a WDM, it serves to mix (multiplex) or separate (demultiplex) two optical signals of different wavelengths. Normally, the interaction length of the coupler is chosen to be L_c for the shorter wavelength and $2L_c$ for the longer wavelength.

2.4.2. Fabrication of Directional Coupler

5 μm thick films on glass substrates were exposed to UV light for 60 minutes. The waveguide width of the directional coupler mask was 5 μm. The separation between the waveguides in the coupling region was 6 μm, and the coupling length was 17 mm.

2.4.3. Characterization

A Nd:YAG laser at λ = 1.06 μm was used to couple light into the In_1 arm of the coupler via a single-mode optical fiber. The waveguides of the directional coupler were single mode at this wavelength. A silicon detector was used to measure output light intensity, as shown in Fig. 2.11. The output power ratio of Out_2 to Out_1 was ~1.5. The beam propagation method was used to analyze the coupler. From the measured output power ratio, the width and depth of the waveguides were computed to conform to the results. These values were 5.5 μm and 3.7 μm respectively. Fig. 2.11 also shows the electric field distribution of guided light in the coupler as calculated by the beam propagation method. The transfer of power can clearly be seen in the coupling region as the intensity in arm 1 gradually decreases while that in arm 2 increases.
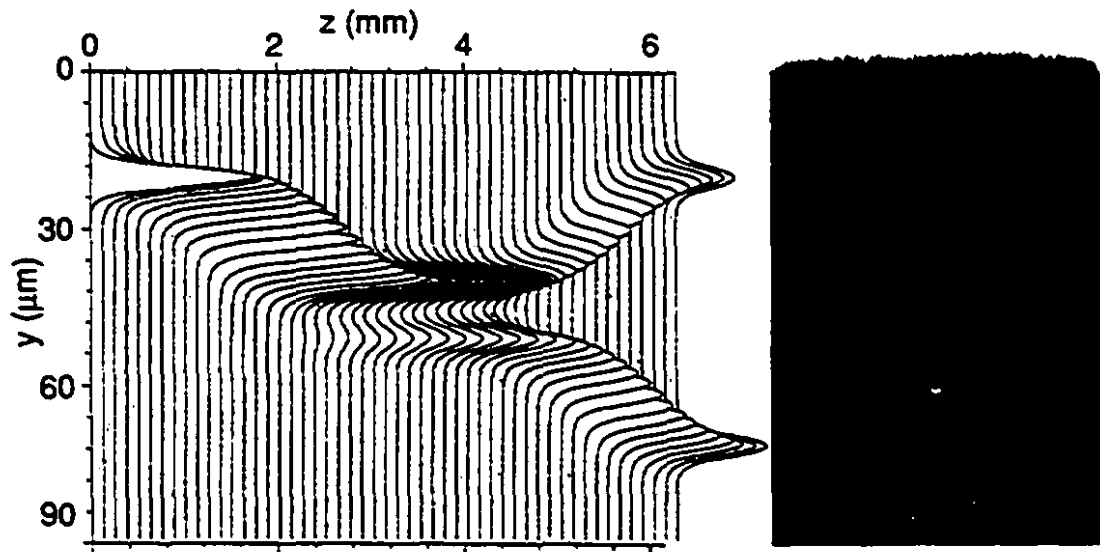
Figure 2.11 Electric field distribution of guided light in directional coupler determined by BPM, and experimental light output

56

2.5. 1 x 8 Beamsplitter

2.5.1. Introduction

Y-junction waveguide devices are usually used to divide light equally into two waveguides. They can be split into 4, 8 or more equal parts by cascading the Y-branches, making 1 x N splitters. In a symmetric Y-branch, the two outgoing branches in the Y are of equal width and make equal angles with the axis of the incoming branch as seen in Fig. 2.12.
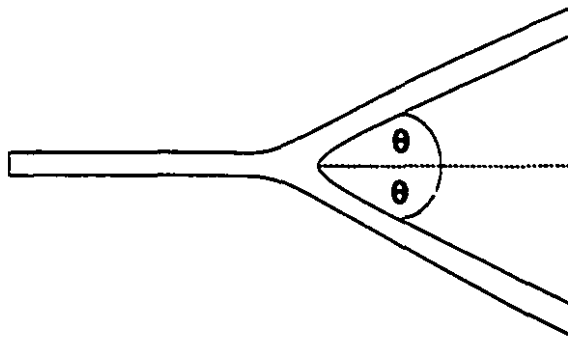
Figure 2.12 Schematic of a Y-branch waveguide

If all branches support only one mode, then an equal power division between the two branches takes place. Losses can be minimized by maintaining a small separation angle (less than one degree). Use of curved waveguides after the junction minimizes device length.

2.5.2. Fabrication of 1 x 8 Beamsplitter

8 μm thick films were deposited on silicon substrates and exposed to UV light for 4 hours. This gave a refractive index change of 0.01, which was sufficient to guide light at 1.55 μm. This was followed by a 60 minute postbake at 110°C. A schematic of the 1 x 8 beamsplitter mask is shown in Fig. 2.13. The mask also contained a channel waveguide which was utilized to determine the configuration losses (i.e., those due to curvature in the beamsplitter).

150 μm

L = 1.7 cm
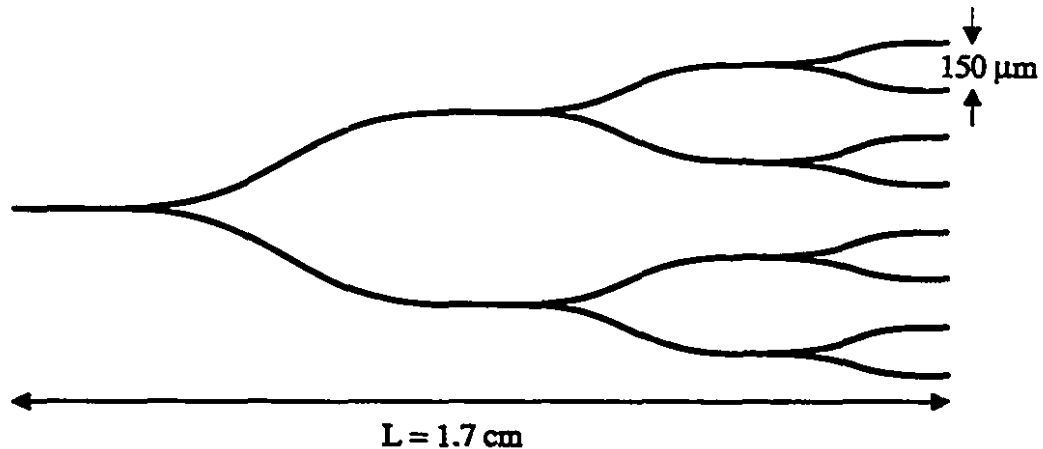
Figure 2.13 Diagram of mask used in fabrication of beamsplitter

2.5.3. Characterization

An AFM image of one of the Y-junctions in the beamsplitter is shown in Fig. 2.14. As with the channel waveguides, the arms of the Y-branch are slightly raised.

58
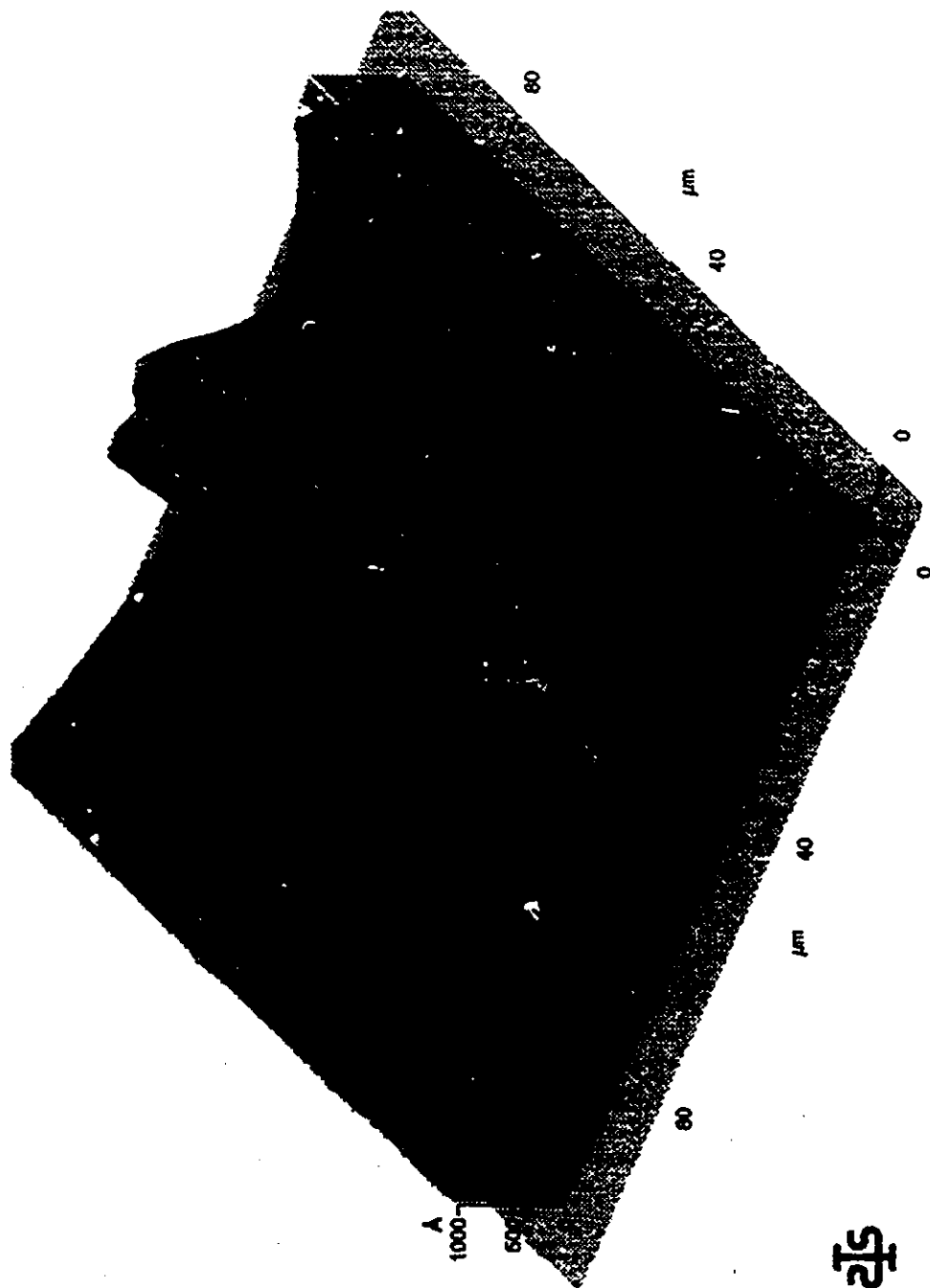
Figure 2.14 AFM image of beamsplitter showing Y-junction

59

Light from both a 0.6328 μm HeNe laser and a 1.55 μm laser diode were coupled into the input waveguide via optical fiber. The waveguides were multimode at 0.6328 μm and single mode at 1.55 μm. The output light was focused onto an infrared camera using a microscope objective. A photograph of light at 1.55 μm from the eight output ports of the beamsplitter is shown in Fig. 2.15.
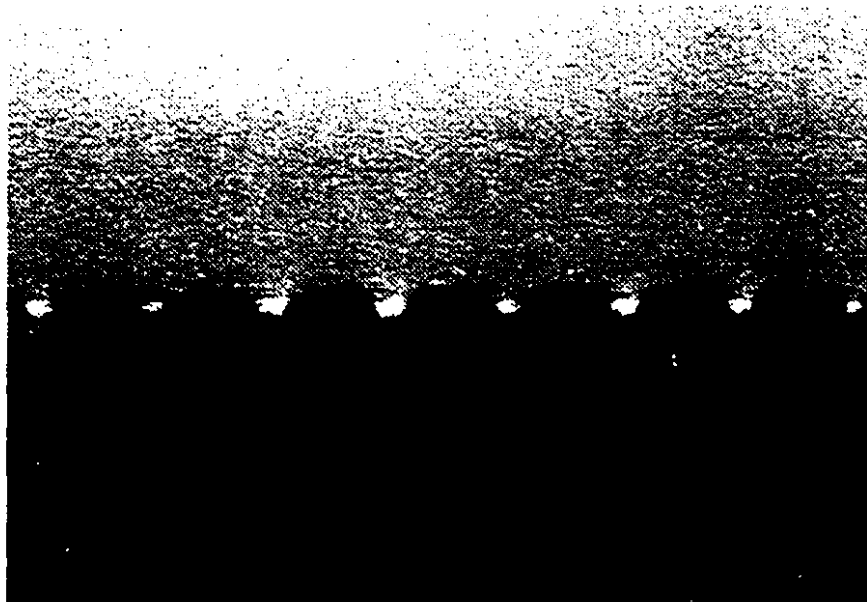
Figure 2.15 Digitized photograph of light at λ = 1.55 μm from output waveguides of 1 x 8 beamsplitter

Light from the output ports was focused onto a germanium photodetector to determine insertion losses. Fig. 2.16 displays measured insertion losses for each output port at 0.6328 μm and 1.55 μm.
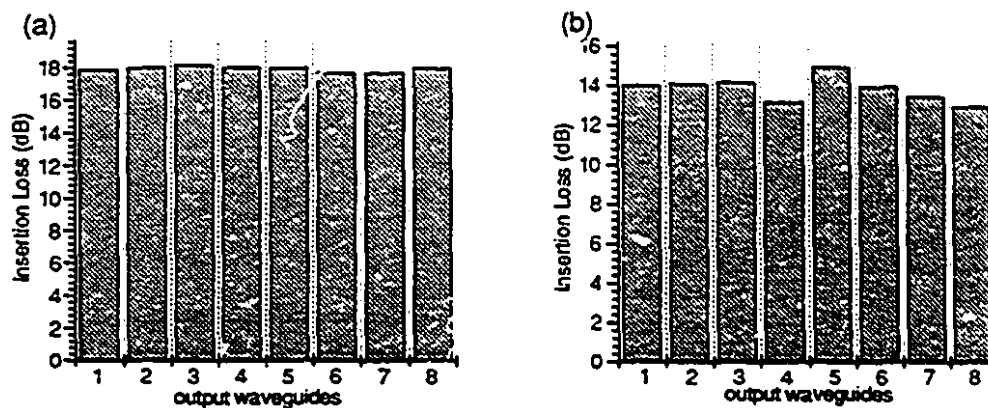
Figure 2.16 *Insertion losses measured from the output waveguides of the beamsplitter at (a) 0.6328 μm, and (b) 1.55 μm*

As can be seen in Fig. 2.16, a relatively uniform power distribution was obtained in this beamsplitter for both wavelengths.

Configuration losses were obtained by measuring the total intensity from all output waveguides of the beamsplitter and subtracting this from the intensity from the output of the channel waveguide on the same substrate. The result gives the configuration losses. These losses were calculated to be 0.83 dB at 1.55 μm while at 0.6328 μm, the losses were too small to be calculated. Configuration losses are inherent in the device design, and in this device are considered to be quite small. Propagation losses measured at 1.55 μm were determined to be less than 0.3 dB/cm, which is also considered to be relatively low.

2.6. Gratings

2.6.1. Introduction

Diffraction gratings are optical elements that consist of a highly regular groove, slit pattern, or refractive index modulations.[10] They direct light into directions that are a function of wavelength and the spacing of the modulations (period, Λ). Modualtions can either be refractive index or surface relief type. A surface relief type grating is shown in Fig. 2.17.
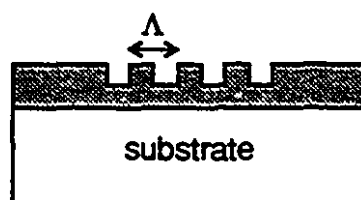
Figure 2.17 Schematic of surface relief type gratings

Diffraction gratings are important components in integrated optics devices. They are used in many areas including distributed feedback (DFB) lasers, distributed Bragg-reflector (DBR) lasers, optical filters, beam deflectors, waveguide couplers, wavelength multiplexers and demultiplexers. Their particular end use depends on design requirements in regards to grating depth and length, and the wavelength(s) of operation. For example, a normally incident guided wave will be reflected by gratings if the Bragg condition is satisfied:[11]

$$\Lambda = \frac{m_g \lambda_b}{2 n_{eff}} \qquad (2.7)$$

where m_g is the grating order, λ_b is the Bragg wavelength and n_{eff} is the effective index of the waveguide. This type of grating can be used in a DBR laser to form a laser cavity.

Current fabrication techniques use ion-exchange and etching. Ion exchange produces low efficiency gratings. Etched gratings can be very efficient and are usually made in one of three ways: holographic exposure, focused ion-beam lithography, and photomask printing. Although these techniques can produce high efficiency gratings, they require time-consuming multi-layer fabrication. Gratings made by the sol-gel process are inexpensive and can be fabricated in one step, avoiding multi-layer processing.

We have made gratings in the ormocer by two techniques. The first was photoimprinting, which involved UV illumination through a mask containing both a grating pattern and a channel waveguide. This method resulted in an index modulation-type grating. Organic components in the sol-gel impart some flexibility to the film. This facilitates embossing for use in defining the grating structure. In the second method, a master surface relief grating was pressed into the soft, deformable film and the pattern replicated in the film.

2.6.2. Fabrication of Gratings

For gratings made by UV light imprinting, a mask consisting of gratings ($\Lambda = 2.0~\mu m$) and a channel waveguide was placed in contact with a 5 μm thick film. It was exposed to UV light for 20 minutes followed by post-baking at 110°C for 60 minutes.

63

Exposed regions of the film increased in refractive index, producing an index modulation type grating.

For embossed gratings, a master was fabricated in a fused silica substrate by holographic interference lithographic techniques. This procedure rendered rectangular (0.3 cm x 1.0 cm) holographic gratings ($\Lambda = 0.41$ μm). To prevent the sol-gel film from sticking during the embossing procedure, hexamethyldisilazane (HMDS) was used to treat the surface of the master. HMDS is commonly used to passivate silica surfaces.[12] It reacts with free surface hydroxyl groups in the following manner:
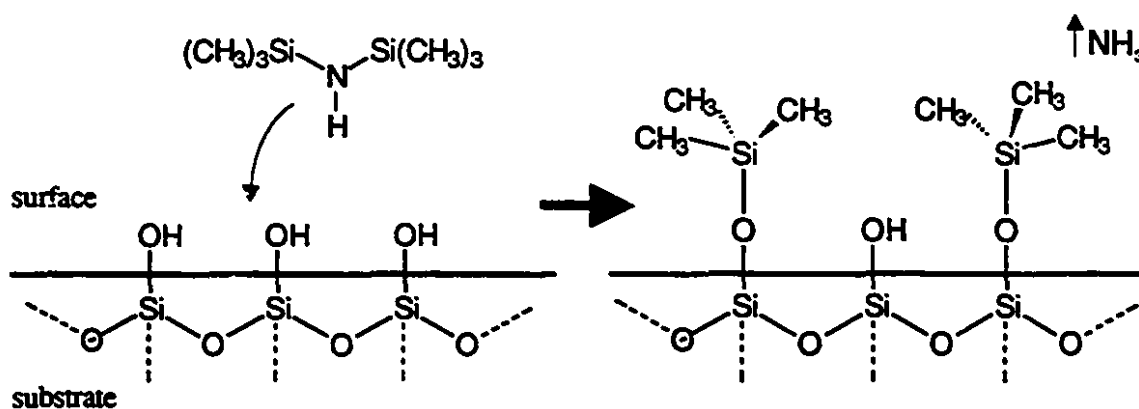
Figure 2.18 Reaction of HMDS with silica surface

With nearly complete surface passivation there is little tendency for the sol-gel to bond chemically with surface hydroxyl groups.

Samples were placed in the embossing apparatus 4 minutes after dip-coating to ensure the film was still soft and deformable. Pressures between 10 and 50 N/cm² were applied for 10 minutes. Some samples were then immediately exposed to UV light for 20

minutes to lock-in the embossed pattern for comparison with unexposed embossed samples. All samples were then postbaked at 110°C for 60 minutes.

2.6.3. Characterization

There is a very slight increase in film thickness on exposure to UV light, as evidenced by atomic force microscopy (AFM) of the photoimprinted gratings shown in Fig. 2.19; however, this increase is small, amounting to ~5 nm. Thus, gratings made by exposure through a mask can be assumed to be predominantly index modulation type gratings. The gratings look quite uniform, both in period and in height. AFM images of the surface relief type gratings made by the combined embossing/photocuring process, with a depth of ~100 nm, are shown in Fig. 2.20. Here, the period looks uniform; however, there is some variation in thickness along the ridges of the gratings (light coloured patches in the AFM image).
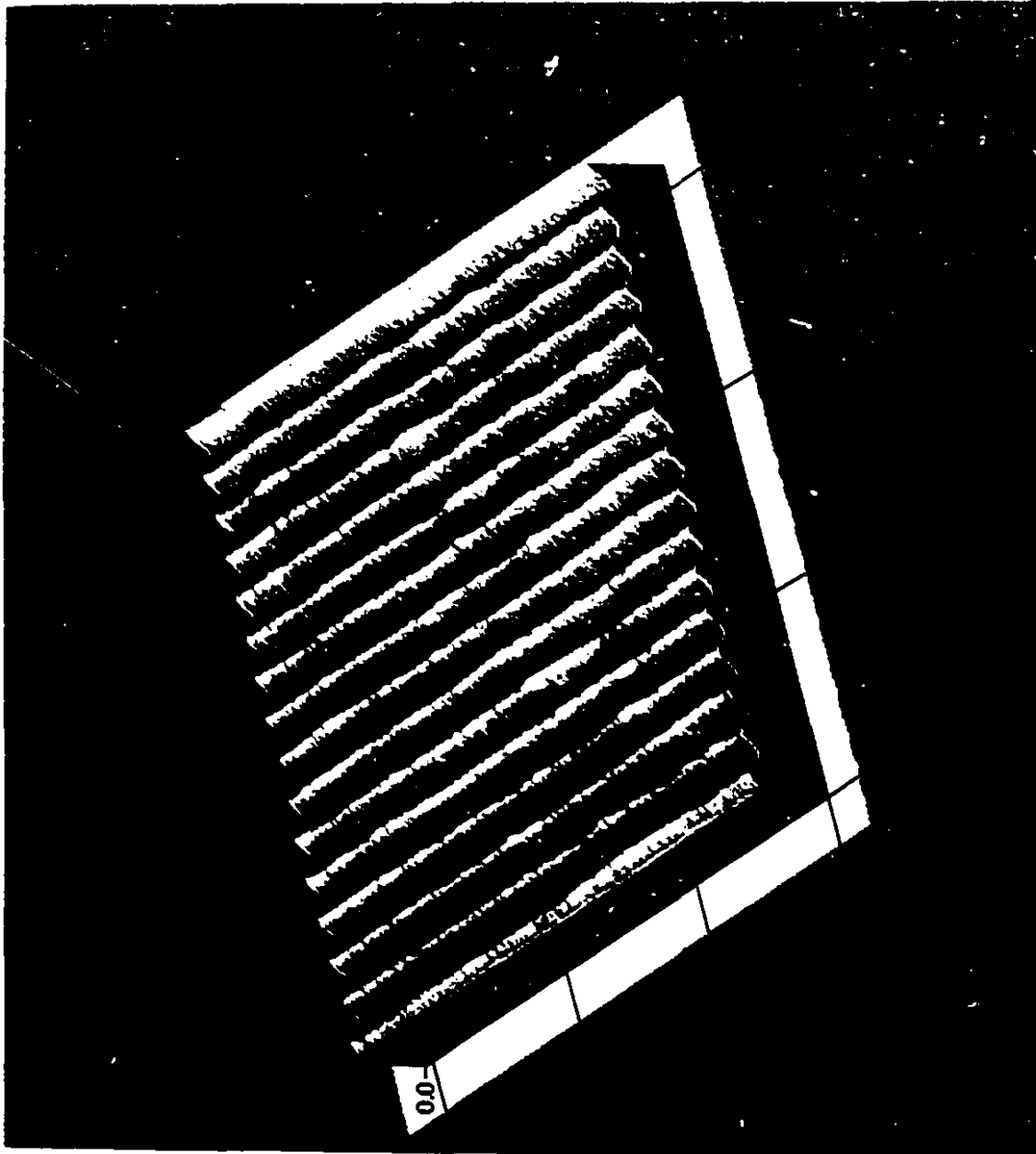
Figure 2.19 AFM image of photoimprinted gratings

66
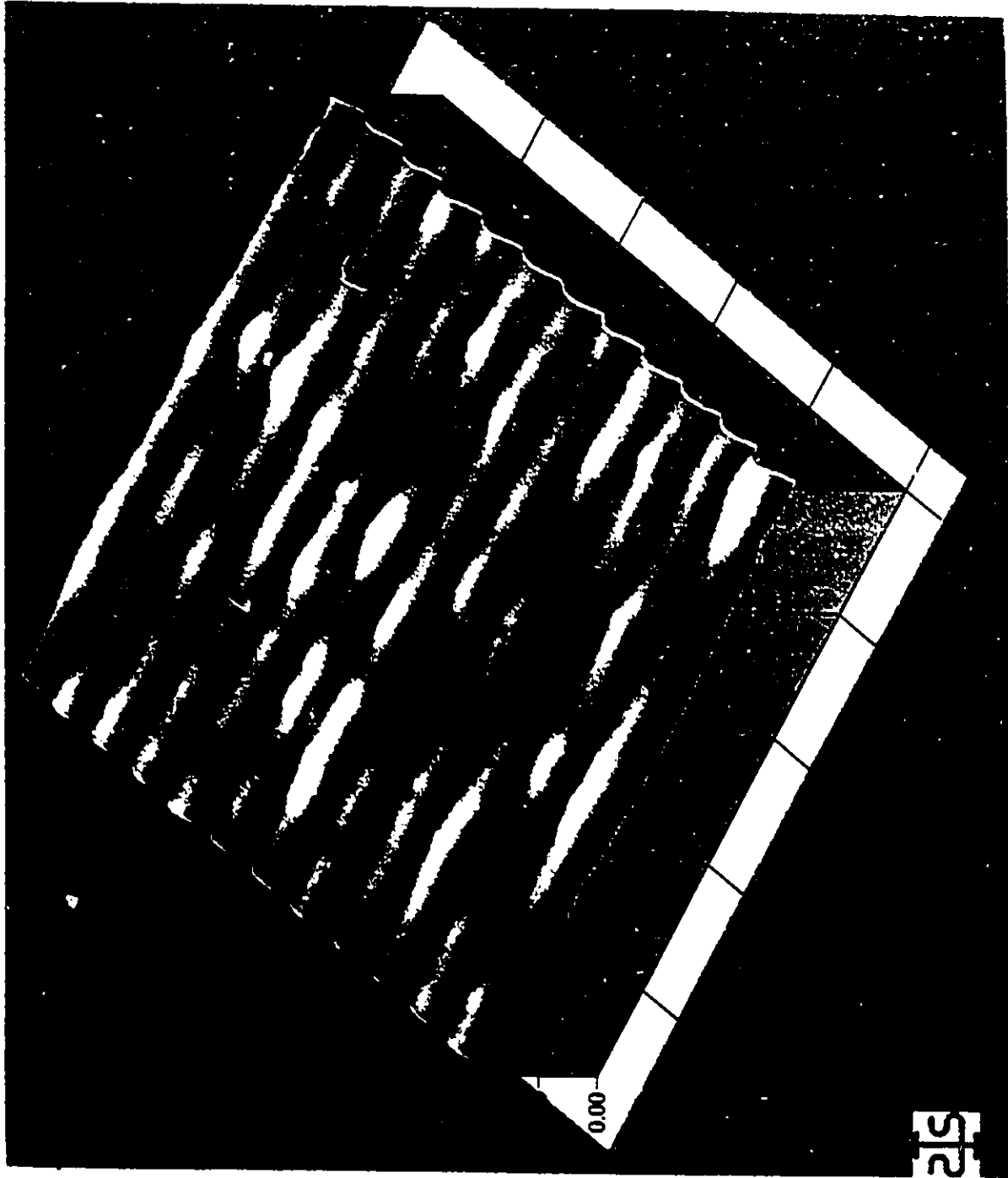
Figure 2.20 AFM image of embossed/photocured gratings

The period of the gratings was measured in the following way: a HeNe laser incident on the gratings produced a diffraction beam at an angle θ to it. The grating period was then calculated from the relation $\Lambda=\lambda/2sin\theta$. Results for both photo-imprinted and embossed gratings were in agreement with the periods of the masters. Calculated periods were confirmed by AFM images.

Diffraction efficiencies were obtained from the ratio of the power of the first order diffracted beam to the power of the incident HeNe laser. Photo-imprinted gratings had an efficiency of 0.22%. The low efficiency was attributed largely to the small refractive index change on exposure to UV light. A larger refractive index change on exposure to UV light may be possible by using a different photoinitiator and/or higher concentrations of photoinitiator. The latter method is known to induce large refractive index changes in PMMA.[13]

Embossed samples that were exposed to UV light, followed by heat treatment, had an efficiency of 1.25%, while embossed samples undergoing heat treatment only had an efficiency of 0.69%. The master gratings for the embossed samples had an efficiency of 1.66%. When comparing these values to the master grating, relative diffraction efficiencies of 75% and 42% respectively were obtained. A relative efficiency in this case is a good indication of the degree of replication that was achieved. Losses were attributed to reflection, absorption and diffraction into other orders. Post-embossing UV exposure had a considerable effect on the efficiency of embossed gratings. Unexposed embossed gratings had a lower efficiency, probably due to relaxation of the grating structure before heat treatment was able to solidify the structure.

Gratings produced by simultaneous embossing/UV exposure[14] may lead to improved efficiencies since any relaxation that may occur during transfer from the embossing apparatus to the UV light source can be avoided. In addition, improvement of the quality of the master gratings would directly lead to improved efficiencies for the embossed samples.

2.7. Conclusions

We have demonstrated that channel waveguides and passive waveguide devices (directional coupler and 1 x 8 beamsplitter) can be fabricated in films of the ormocer sol-gel described in Chapter 1. The procedure consists of four basic steps: sol-gel synthesis, dip-coating, UV exposure, and postbaking. It is a low cost procedure and is not labour intensive, unlike most current fabrication technologies. Waveguides and devices are defined by UV light through a mask which increases the refractive index of the sol-gel in the exposed regions. This material and process leads to waveguides with very low losses.

We were able to demonstrate waveguides capable of guiding at $\lambda = 0.6328$, 1.06 and 1.55 μm on silicon substrates, both with and without an SiO_2 buffer layer. This was accomplished by modifying waveguide configurations. The directional coupler was functional at $\lambda = 1.06$ μm, with power being transfered from arm 1 to arm 2 such that the output power ratio of arm 2:arm 1 was ~1.5. The 1 x 8 beamsplitter was functional at both $\lambda = 0.6328$ and 1.55 μm. A uniform power distribution in the output ports was observed for both wavelengths.

We have demonstrated that gratings can be fabricated in the ormocer sol-gel by two different methods. Photoimprinting produces index modulation type gratings while embossing produces surface relief type gratings. Exposure of embossed gratings to UV light locks in the grating structure and improves efficiency over embossed gratings subjected to thermal treatment only.

2.8. References

1. L.D. Hutcheson, In *Integrated Optical Circuits and Components*, L.D. Hutcheson, Ed., Marcel Dekker Inc., New York, 1987.

2. J.D. Mackenzie and Y.H. Kao. In *Glass Integrated Optics and Optical Fiber Devices*, S.I. Najafi, Ed., SPIE, Bellingham, WA, 1994.

3. M.F. Grant, In *Glass Integrated Optics and Optical Fiber Devices*, S.I. Najafi, Ed., SPIE, Bellingham, WA, 1994.

4. B.D. Fabes, D.J. Taylor, L. Weisenbach, M.M. Stuppi, D.L. Klein, L.J. Raymond, B.J.J. Zelinski and D.P. Birnie, *Sol-Gel Optics, SPIE Proc.*, **1328**, 319, (1990).

5. R.G. Hunsperger, *Integrated Optics: Theory and Technology*, Springer-Verlag, Berlin, 1991.

6. D.G. Hall and L.D. Hutcheson, In *Integrated Optical Circuits and Components*, L.D. Hutcheson, Ed., Marcel Dekker Inc., New York, 1987.

7. Integrated Optics Design Software, Optonex Ltd., Espoo. Finland.

8. S.I. Najafi, In *Introduction to Glass Integrated Optics*, S.I. Najafi, Ed., Artech House, Boston, 1992.

9. S. Honakanen, In *Glass Integrated Optics and Optical Fiber Devices*, S.I. Najafi, Ed., SPIE, Bellingham, WA, 1994.

10. E.G. Loewen, In *The Photonics Design and Applications Handbook*, Laurin Publishing, Pittsfield, MA, 1994.

11. M. Fallahi, In *Glass Integrated Optics and Optical Fiber Devices*, S.I. Najafi, Ed., SPIE, Bellingham, WA, 1994.

12. W. Hertl and M.L. Hair, *J. Phys. Chem.*, **75**, 2181, (1971).

13. H. Franke, In *Polymers for Lightwave and Integrated Optics*, L.A. Hornak, Ed., Marcel Dekker Inc., New York, 1992.

14. H. Krug, N. Merl and H. Schmidt, *J. Non-Cryst. Solids*, **147&148**, 447, (1992).

71

3. Erbium Coordination Chemistry

3.1. Introduction

Rare earth ions have long been known for their luminescence properties. In the field of optics, two rare earth ions in particular have received much attention: Nd^{3+} and Er^{3+}. Their characteristic emission wavelengths of interest are 1.3 μm and 1.55 μm respectively. The significance of these wavelengths is that they lie in the regions where dispersion and absorption, respectively, are lowest in silica glass: the so-called second and third telecommunications windows. Silica glass has many desirable properties that make it a good choice for optical applications. These include high UV transparency, high mechanical strength, high glass transition temperature, and extremely low thermal expansion.[1] The development of low loss single mode silica optical fibers, with losses as low as 0.2 dB/km, revolutionized the telecommunications industry. Continued efforts have led to high gain, low noise Er^{3+} fiber amplifiers,[2] allowing all-optical transoceanic fiber links, further demonstrating silica's importance and versatility in optics.

The relevant energy levels for Er^{3+} and Nd^{3+} are shown in Fig. 3.1.
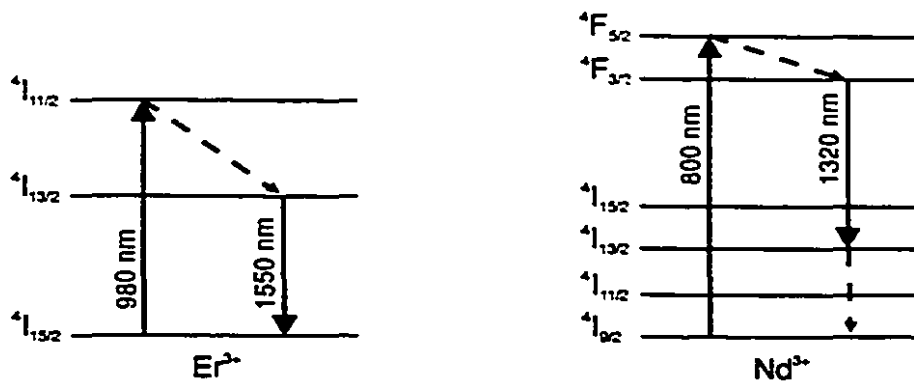
Figure 3.1 Energy level diagrams for erbium and neodymium

The transitions of interest are the $^4I_{13/2} \rightarrow {}^4I_{15/2}$ in Er^{3+} at 1.55 μm and the $^4F_{3/2} \rightarrow {}^4I_{13/2}$ in Nd^{3+} at 1.32 μm. As can be seen in Fig. 3.1, devices that utilize the $^4F_{3/2} \rightarrow {}^4I_{13/2}$ Nd^{3+} transition operate as four-level systems. Population inversions are achievable with very small pump powers. Devices using the $^4I_{13/2} \rightarrow {}^4I_{15/2}$ Er^{3+} transition operate as three-level systems. Greater pump powers are required since the system must be bleached before a population inversion occurs. Devices utilizing three-level systems present the additional problem of absorption of the luminescent signal by portions of the waveguide not pumped.[3]

The performance of active devices based on rare earth ions is determined by the relevant electronic and optical characteristics of the ion. These include absorption cross-section, spectral shapes of absorption and emission bands, excited state lifetimes, ion-ion interactions and ion-lattice interactions.[4] A major influence on all these properties is the host material. Silica glass has the drawback of being able to dissolve only low concentrations of rare earth ions. At higher concentrations, microscopic clustering of rare

73

earth ions occurs, rendering them unavailable for lasing applications. With Nd^{3+}, clustering leads to concentration quenching, whereby an ion in an excited state transfers part of its energy to a nearby ground state ion. The result is that both ions decay to the ground state non-radiatively. With Er^{3+}, cooperative upconversion can occur. In this process, two excited ions interact and one transfers its energy to the other. The result is one ion in the ground state with the other in a higher level which quickly non-radiatively decays back to its metastable state. The net result of the whole process is the conversion of one quantum of excitation into heat. This is of particular concern at high pump powers where high population inversions are necessary for efficient devices.

For optical fiber amplifiers, low concentrations are sufficient since device lengths are on the order of a few metres. For many integrated optical applications, higher concentrations are necessary since high gain is required over a short interaction length. One solution is to modify device structures so that interaction lengths are increased, allowing lower rare earth concentrations to be used. This was achieved for instance in an erbium doped integrated optical amplifier demonstrated by Kitigawa et al.[5] The waveguide length was increased by having several S-bends on the substrate. Another solution to this problem is achieved by material modification.

Aluminum or phosphorus co-doping in silica glass has been shown to increase the solubility of both Nd^{3+} and Er^{3+}.[1,6,7] Arai et al.[8] have described this effect for Nd-doped silica glasses. Rare earth ions need to be coordinated to a large number of non-bridging oxygens in the silica network to screen the charge on the cation. This places the Nd^{3+} in a high enthalpy state due to the difficulty in reaching coordination saturation. The Arai

model proposes that co-dopant oxides preferably coordinate Nd^{3+} ions and form a solvation shell, reducing the high enthalpy state. In terms of solution chemistry, SiO_2 is a poor solvent for Nd^{3+}, while both Al_2O_3 and P_2O_5 are soluble in SiO_2 and easily dissolve Nd_2O_5. Similar results have been found for Er^{3+} in Al-doped silica glasses.[5]

Rare earth doped glasses have been prepared by several different methods including flame hydrolysis deposition (FHD), ion exchange, chemical vapour deposition (CVD), and melting.[3] These are all high temperature techniques, which precludes them for many applications. In contrast, the sol-gel method for making rare earth doped glasses is a low temperature process. Several other advantages, including the ability to dope to higher concentrations and uniform rare earth ion distribution, make the sol-gel method a good choice. One of its main drawbacks, however, is residual hydroxyl which quench the $^4I_{13/2} \rightarrow {}^4I_{15/2}$ emission. Non-radiative relaxations may occur in rare earth ions by interaction between one of its excited state electronic levels and a suitable vibrational mode of its environment. Very efficient non-radiative transitions can occur due to vibronic coupling with the highly energetic vibrational states of OH oscillators nearby.[9,10] The very nature of the sol-gel process implies that there is alcohol and water present (i.e., hydroxyls). Drying removes most of the residual water and alcohols, but some may remain trapped in pores, or may be incorporated into the coordination sphere of the rare earth ion. In addition, some silanol groups produced during the hydrolysis reaction may not have undergone condensation reactions, leaving hydroxyl groups in the glass. Thus there are numerous sinks which may reduce or eliminate altogether, luminescence in sol-gel glasses.

One possible solution to this problem is to encapsulate the ion in a coordination sphere, thereby shielding it from its local environment. This may help to reduce, or eliminate the effects of hydroxyl quenching. In addition, there is the possibility of optimizing the luminescence properties of the ion by suitable choice of ligands.[9] It has been known for quite some time that rare earth fluorinated β-diketonates can lase.[11,12,13,14,15,16]

The aforementioned studies have focused almost exclusively on europium complexes. These have a very intense, narrow emission at ~610 nm (the $^5D_0 \rightarrow {}^7F_2$ transition), facilitating its study. Matthews and Knobbe[17] report that some of these europium fluorinated β-diketonate complexes can be doped into sol-gel glasses. The emission intensity was fifty times greater than from the same glasses doped with $EuCl_3$. In addition, they found that the spontaneous-emission cross-sections of the europium complexes (a measure of the radiation emission intensity from a given sample volume) were two to three orders of magnitude higher.

These results suggest that rare earth coordination complexes are good vehicles for introducing the ion into a sol-gel glass host. We have concentrated our efforts on fluorinated β-diketone complexes of erbium (III) to obtain luminescence at 1.55 μm. It seemed likely that synthetic procedures for europium would transfer to erbium. The chemistry among the rare earths is similar for the same oxidation states; differences among the lanthanides lie mainly in the number of 4f electrons.[18] These are sufficiently well shielded by the outlying 5s and 5p orbitals that they are essentially unavailable for chemical

76

interaction. The primary consequence of differing numbers of f-electrons is something known as the "lanthanide contraction": a decrease in ionic radius with increasing atomic number along the lanthanide series. This occurs because the addition of electrons to the already shielded f-orbitals cannot compensate for the stronger effect of increasing poorly screened nuclear charge. Thus there are slight differences in chemistry of rare earths, especially in coordination number, that are due to atomic or ionic size.

There is little information available on β-diketone coordination complexes of erbium. Some authors report preparing complexes over a series of rare earth ions, including erbium. However, they generally do not discuss specifics in regards to the erbium complexes. In addition, erbium coordination chemistry has concentrated on tris complexes. Accordingly, for the present studies a series of tetrakis erbium complexes were prepared and characterized. These were then doped into both the ormocer and MTMS sol-gels, and the resulting doped-glasses were further studied.

3.2. Experimental

3.2.1. Materials

The following chemicals were obtained from Aldrich: $ErCl_3 \cdot 6H_2O$ (99.9%); $Er(NO_3) \cdot 5H_2O$ (99.9%); 4,4,4-trifluoro-1-(2-thienyl)-1,3-butanedione (TTFAH) (99%); 4,4,4-trifluoro-1-phenyl-1,3-butanedione (PTFAH) (99%); 1,1,1,5,5,5-hexafluoro-2,4-pentanedione (HFAH) (99%); tetrapropylammonium hydroxide (1.0 M solution in water).

77

Triethylamine (99.5%) was obtained from Caledon. Tetraethylammonium bromide was obtained from J.T. Baker Chemical Co. Sodium hydroxide was obtained from BDH. All chemicals were used without further purification.

3.2.2. Synthesis of Erbium Complexes

Erbium (III) complexes of the type $AErB_4$ were prepared where A is an ammonium ion ($HNEt_3^+$, NEt_4^+, or NPr_4^+) and B is a fluorinated β-diketone of the type:
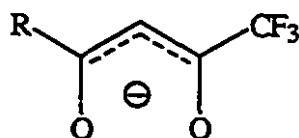
where R = thienyl, phenyl or CF_3. The synthetic procedures of Melby et al.[13] and Bauer et al.[14] were followed.

A.   Triethylammonium tetrakis(4,4,4-trifluoro-1-(2'-thienyl)-1,3-butanedionato-O,O') erbate(III) $[HNEt_3]^+[Er(TTFA)_4]^-$ (Procedure #13 in Melby et al.)

2.0 g (9.0 mmol) of TTFAH was dissolved in 30 mL 95% ethanol and heated to reflux. 0.91 g (9.0 mmol) of NEt_3 was added and the solution was again heated to reflux. 0.89 g (2.0 mmol) of $Er(NO_3)_3 \cdot 5H_2O$ dissolved in 10 mL water was added and the solution heated to reflux. Refluxing continued for approximately 30 min. A hot filtration was performed to remove insoluble impurities. Crystals deposited from the room

78

temperature solution after one hour. These were collected by suction filtration and washed with cold ethanol. To dry the crystals, air was drawn through for 15 min. Light pink, small, flaky crystals were produced.

B.   Triethylammonium tetrakis(4,4,4-trifluoro-1-phenyl-1,3-butanedionato-O,O')

erbate(III)   [HNEt$_3$]$^+$[Er(PTFA)$_4$]$^-$ (Procedure #13 in Melby et al.)

2.92 g (13.5 mmol) of PTFAH was dissolved in 45 mL 95% ethanol and heated to reflux. 1.37 g (13.5 mmol) of NEt$_3$ was added and the solution was again heated to reflux. 1.33 g (3.0 mmol) of Er(NO$_3$)$_3$·5H$_2$O dissolved in 15 mL water was added and the solution heated to reflux. Refluxing continued for approximately 45 min. A hot filtration was performed to remove insoluble impurities. Crystals deposited from the room temperature solution after 12 hours. These were collected by suction filtration and washed with cold ethanol. To dry the crystals, air was drawn through for 15 min. Light pink, small, flaky crystals were produced.

C.   Triethylammonium tetrakis(1,1,1,5,5,5-hexafluoro-2,4-pentanedionato-O,O')

erbate(III)   [HNEt$_3$]$^+$[Er(HFA)$_4$]$^-$ (Procedure #15 in Melby et al.)

1.52 g (15 mmol) of NEt$_3$, 3.90 g (18.7 mmol) of HFAH, and 1.66 g (3.7 mmol) of Er(NO$_3$)$_3$·5H$_2$O dissolved in 18 mL water were added in the above order to 37.5 mL of 95% ethanol. The solution was heated to boiling and allowed to boil down to half its original volume. 50 mL of water was added to produce a sticky pink precipitate.

79

Scratching of the flask induced crystallization. The product was collected by suction filtration. Recrystallization in chloroform yielded long bright pink needles.

D.   Tetraethylammonium tetrakis(4,4,4-trifluoro-1-phenyl-1,3-butanedionato-O,O')

erbate(III)   [NEt$_4$]$^+$[Er(PTFA)$_4$]$^-$ (Procedure #14 in Melby et al.)

2.16 g (10 mmol) of PTFAH and 0.53 g (2.5mmol) of NEt$_4$Br were added to 25 mL of 95% ethanol and heated to reflux. 10 mL of 1.0 M NaOH was added and the solution returned to reflux. After 10 min, 1.11 g of Er(NO$_3$)$_3$·5H$_2$O dissolved in 10 mL water was added and the solution was refluxed for a further 20 min. The solution was left to stand at room temperature for two days, after which the precipitate was collected by suction filtration and washed with cold 50% ethanol. The product was a light pink coloured powder which was recrystallized from ethanol.

E.   Tetrapropylammonium tetrakis(4,4,4-trifluoro-1-(2'-thienyl)-1,3-butanedionato-

O,O') erbate(III)   [NPr$_4$]$^+$[Er(TTFA)$_4$]$^-$ (Method B in Bauer et al.)

2.67 g (12 mmol) of TTFAH and 1.15 g (3 mmol) of ErCl$_3$·6H$_2$O were added to 100 mL of 95% ethanol and heated to reflux. To this was added 12 mL of a 1.0 M solution (12 mmol) of NPr$_4$OH. The solution was brought to reflux once again and heating was continued for one hour. Approximately 30 mL of solvent was then distilled off at 65°C. It was then cooled to room temperature and small crystals slowly began to form. Small, flaky, pinkish-orange crystals were collected by suction filtration and washed with cold ethanol. These were then recrystallized with 95% ethanol.

3.2.3. Preparation of Erbium-doped Sol-Gels

Erbium β-diketone complexes as well as erbium salts ($Er(NO_3)_3$, $ErCl_3$ and Er-acetate) were doped into both the ormocer and MTMS sol-gels described in Chapter 1. Doping levels were usually 2 wt% erbium ion. This was based on a calculation of the amount of solid material that would form per gram of sol, assuming that the sol-gel reactions went to completion and all residual water and alcohol evaporated. When doping into the ormocer, the desired complex or salt was added in solid form into the stirred sol approximately 45 minutes following the final addition of water. The compounds dissolved in minutes to hours, depending on the particular dopant. When preparing doped MTMS sol-gels, the particular dopant was dissolved into MTMS, then HCl was added to initiate the hydrolysis reactions. The PTFA complexes were not soluble in MTMS. Bulk samples and films were prepared from both sol-gel materials by the methods described in Chapter 1.

3.2.4. UV-Visible Absorption Spectroscopy

UV-visible absorption spectra were recorded with a Hewlett Packard 8452A diode array spectrophotometer over the wavelength range of 200 to 800 nm. Spectra were collected from all erbium β-diketone complexes dissolved in acetone, and from selected complexes dissolved in the ormocer sol.

3.2.5. Fourier Transform Infrared (FTIR) Spectroscopy

Infrared spectra were collected with a Bruker IFS-48 Fourier transform infrared spectrometer, in the range of 400 to 5000 cm^{-1}. The data acquisition software was supervised by OPUS Spectroscopic Software, Version 2 (Bruker) running under OS/2 operating system. Infrared spectra were imported into GRAMS spectral analysis software (Galactic Industries, Salem, NH) where spectral processing was performed.

3.2.6. Near Infrared (NIR) Spectroscopy

Near infrared spectra were collected with a Nicloet, Magna-IR 550 Spectrometer. The data acquisition software used was OMNIC, running under Windows 3.11 (Microsoft). Spectral processing was performed in GRAMS. Spectra were taken of erbium complexes dissolved in acetone, ethanol and/or dimethylformamide to a concentration of 10^{-2} M in a cuvette with a 1 cm path length. Spectra were also taken of the complexes in both the ormocer and MTMS glass hosts.

3.2.7. Elemental Analysis

Elemental analyses were performed on all erbium complexes by Guelph Chemical Laboratories Ltd. (Guelph, Ontario).

3.2.8. X-ray Crystallography

Single crystals of $NEt_4Er(PTFA)_4$ were grown for x-ray crystallography by dissolving the complex in a minimum amount of 100% ethanol and letting the solvent evaporate over a period of four days. The diffractometer used was a Rigaku AFC6S with

a Molybdenum Kα radiation source (λ=0.70930 Å). Further details are given in Appendix 1.

3.2.9. Melting Point Determination

Melting point determinations were performed on a Capillary Digital Melting Point Apparatus (Electrothermal).

3.3. Results and Discussion

3.3.1. Erbium β-Diketone Complexes

Fluorinated erbium β-diketone complexes were prepared with the intention of introducing erbium into a sol-gel glass host to obtain luminescence at 1.55 μm. Ligand encapsulation of erbium may offer the advantage of enabling higher concentrations of erbium to be dissolved into organically modified sol-gel glasses.

The reasons for choosing the particular erbium complexes are threefold. Firstly, there is a large amount of information available on analogous complexes of europium. These complexes have been intensely studied by a number of groups since the early 1960's for their luminescence properties. It is known that for the europium complexes, variations in the cation and ligand structure can affect fluorescence intensity and emission fine structure.[12] For example, fluorinated chelates show much more intense fluorescence than hydrocarbon chelates, whereas some cations quench fluorescence. Secondly, a

hydrophobic coordination shell was desired to try and reduce the effect of hydroxyl quenching. Thirdly, some of the ligands have low symmetry. This reduces the local-field symmetry of the rare earth ion making the radiative transitions more allowed.

With the above rationale in mind, the ligands chosen were thenoyltrifluoroacetone (TTFAH), phenyltrifluoroacetylacetone (PTFAH) and hexaflouroacetylacetone (HFAH). All ligands are bidentate and coordinate to the erbium through the oxygen substituents. The trifluoro groups, in addition to providing possible luminescence enhancement, are also very hydrophobic. The role of the organic base in the synthesis is to ionize the diketone (forming the enolate anion) and also to act as a cation in the resulting salts. The counterions ($HNEt_3^+$, NEt_4^+, or NPr_4^+) were selected because complexes of europium containing these cations have exhibited luminescence. The complexes are soluble in many organic solvents. They are insoluble in water. All of the complexes were obtained in crystalline form with colours ranging from light pink to pinkish-orange.

As previously mentioned, both tris and tetrakis europium β-diketone complexes are readily synthesized by reacting stoichiometric quantities of ligand and europium. In the case of erbium, this may not necessarily occur due to differences in ionic radii (Eu^{3+}, r = 0.95Å; Er^{3+}, r = 0.88Å). With a smaller ionic radius, there is less room for the ligands to approach the ion, and perhaps only the tris complexes may form, especially with the sterically bulky PTFA and TTFA ligands. Indeed, the only reference to the formation of a tetrakis erbium β-diketone complex is for the HFAH ligand.[12] This is of some consequence since some of the groups studying europium complexes found that the

tetrakis complexes showed stronger luminescence than the corresponding tris complexes.[19]

Lanthanides can have coordination numbers ranging from six to ten, although eight is most frequently found. The ion attracts ligands by overall electrostatic forces, since the well shielded f-electrons don't interact with ligands the way d-electrons do in transition metal complexes. This absence of strong covalent, directional bonding, and large ionic size allows for a variety of coordination numbers. In addition, crystal field splitting is quite small (200-300 cm^{-1}). Complexes reported to have coordination numbers of six usually have coordinated solvent molecules. The tetrakis β-diketone complexes are believed to be octacoordinate,[13] where the lanthanide ion is surrounded by four chemically equivalent β-diketone moieties. X-ray crystallography on the NEt$_4$Er(PTFA)$_4$ complex confirmed that this was indeed the case. An ORTEP view of the Er(PTFA)$_4^-$ anion is shown in Fig. 3.2. Ellipsoids are drawn at the 50% probability level, and hydrogens are omitted for clarity. The compound is monoclinic. Further crystallographic details, including atomic coordinates and bond lengths are given in Appendix 1.

85
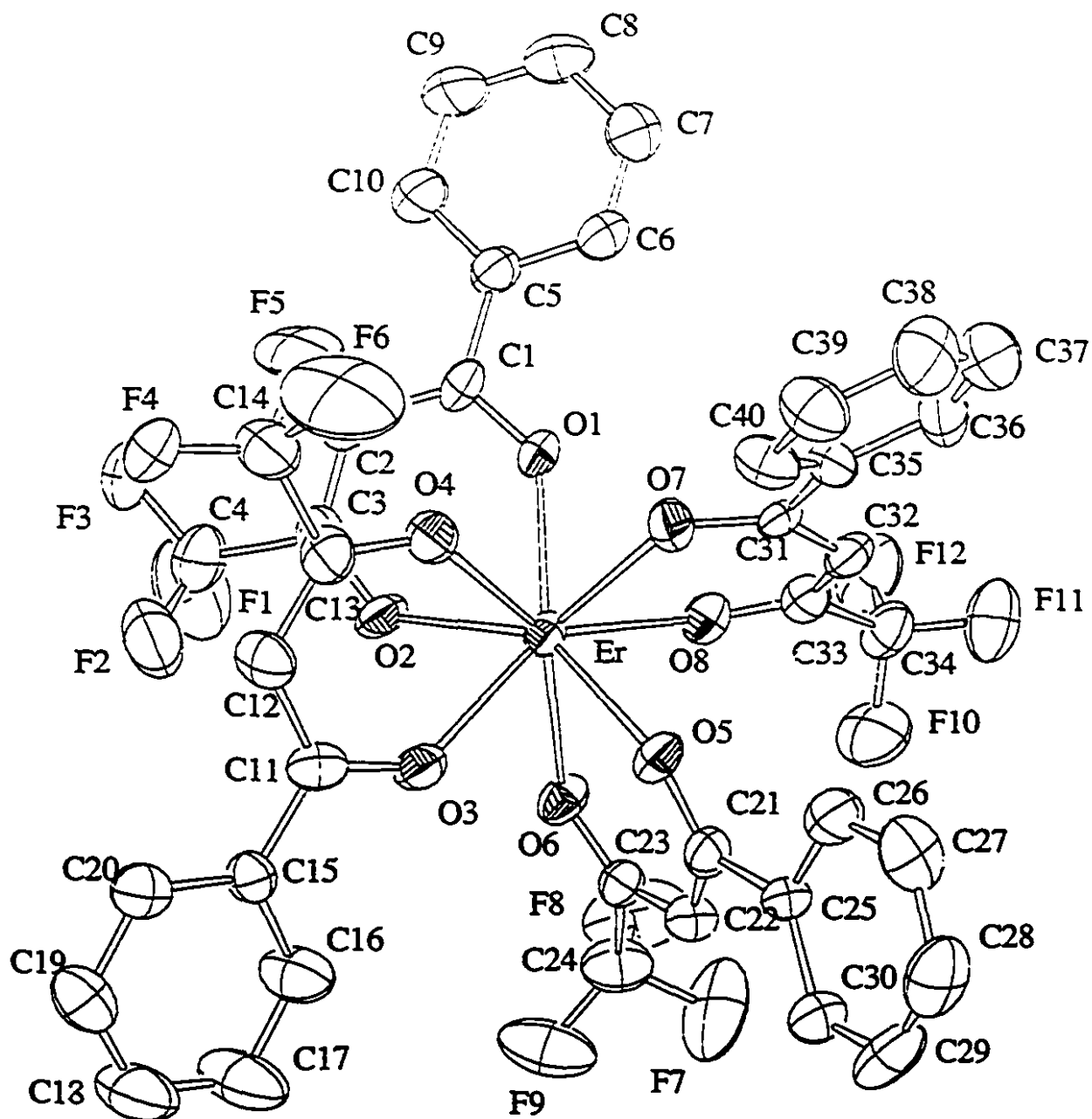
Figure 3.2 ORTEP view of the Er(PTFA)₄ anion with the numbering scheme adopted. Ellipsoids drawn at 50% probability level. Hydrogens omitted for clarity.

Octacrordinate lanthanide complexes most commonly adopt square antiprismatic and dodecahedral geometries. The erbium ion in this complex has tetragonal antiprism coordination. The preference for one symmetry over the other is driven mainly by steric requirements of the ligands or molecular packing forces.[20] Several different stereo- and geometric isomers are possible, especially with bidentate ligands. Bauer et al.[13] even found that it is possible to obtain two different forms of the same compound, having different melting points and emission spectra. This may explain the large melting point ranges (6 degrees) for two of the complexes since no attempt was made to isolate different isomers. Melting point data are given in Table 3.1.

Table 3.1 *Melting points of erbium β-diketone complexes*

Complex	Melting Point (°C)
HNEt₃Er(TTFA)₄	156-158
HNEt₃Er(PTFA)₄	110-113
HNEt₃Er(HFA)₄	143-149
NPr₄Er(TTFA)₄	197-198
NEt₄Er(PTFA)₄	166-172

In addition to the x-ray crystallographic data, further support for the existence of tetrakis chelates is given by elemental analysis. Results are presented in Table 3.2.

Table 3.2 Elemental analysis of erbium β-diketone complexes

Complex	%C		%H		%F		%S	
	calc.	meas.	calc.	meas.	calc.	meas.	calc.	meas.
HNEt$_3$Er(TTFA)$_4$	39.55	40.22	2.79	3.26	19.75	19.97	11.11	11.02
HNEt$_3$Er(PTFA)$_4$	48.89	48.87	3.57	3.66	20.17	20.62	-	-
HNEt$_3$Er(HFA)$_4$	28.45	28.39	1.84	1.97	41.54	40.78	-	-
NPr$_4$Er(TTFA)$_4$	42.68	42.77	3.58	3.76	18.41	17.52	10.36	9.68
NEt$_4$Er(PTFA)$_4$	49.78	49.58	3.83	3.62	19.68	19.72	-	-

Measured values are in good agreement with calculated values.

UV-vis spectra were taken of the erbium complexes dissolved in acetone. The peaks and their corresponding f-orbital electronic transitions are given in Table 3.3.

Table 3.3 UV-Visible Absorption Spectra of Erbium Complexes

Peak Position (nm)	Assignment
378	$^4G_{11/2} \leftarrow {}^4I_{15/2}$
450	$^4F_{3/2}, {}^4F_{5/2} \leftarrow {}^4I_{15/2}$
487	$^4F_{7/2} \leftarrow {}^4I_{15/2}$
521	$^4H_{11/2} \leftarrow {}^4I_{15/2}$
543	$^4S_{3/2} \leftarrow {}^4I_{15/2}$
653	$^4F_{9/2} \leftarrow {}^4I_{15/2}$

There were no major differences between spectra. This is to be expected since absorption bands for f-f electronic transitions show little dependence on the nature of the ligand.[21] These bands are very sharp because the f-orbitals are well shielded from their surroundings. External field induced splittings amount to only about 100 cm^{-1} on states arising from the various f^n configurations. The peak at 378 nm is only evident in the spectrum of the HFA complex. In the PTFA and TTFA complexes, this peak is hidden by intense ligand absorption bands which begin around 400 nm. The ligand absorption for the HFA complex does not begin until around 365 nm. The UV-vis absorption spectrum for the HFA complex in acetone is shown in Fig. 3.3.
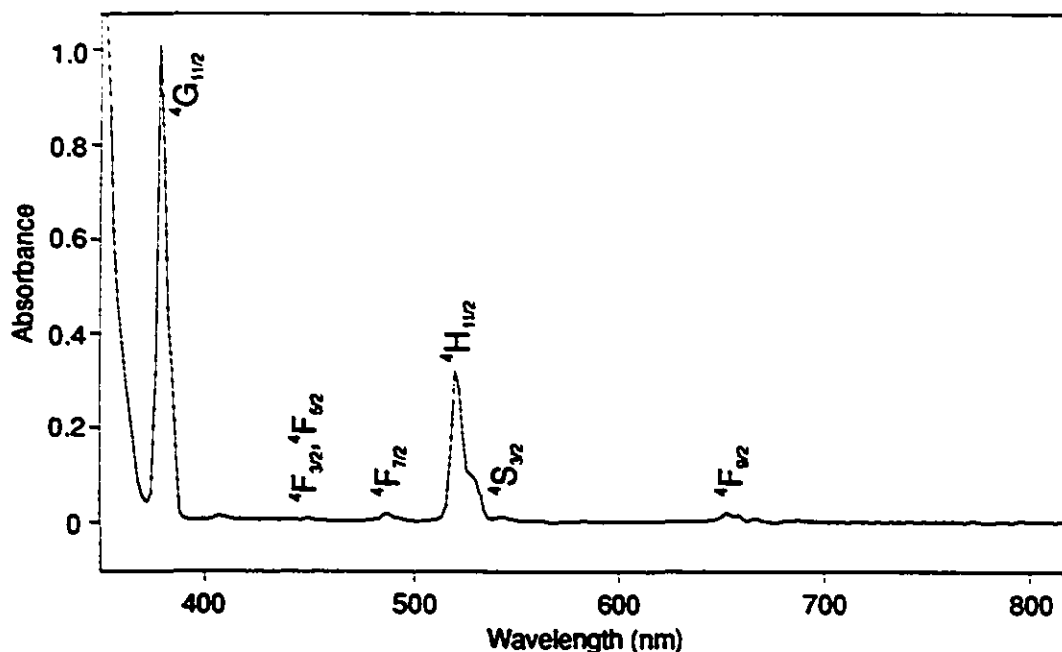
Figure 3.3 UV-vis absorption spectrum of $HNEt_3Er(HFA)_4$ in acetone

All complexes were further characterized by FTIR. Figs. 3.4, 3.5, and 3.6 show

FTIR spectra of $HNEt_3Er(TTFA)_4$, $HNEt_3Er(PTFA)_4$, and $HNEt_3Er(HFA)_4$ respectively.

Tables 3.4, 3.5 and 3.6 present the respective peak assignments. Spectra of both TTFA

complexes were essentially identical, indicating that the counterion had no effect on the

spectra. The same was true for the PTFA complexes. Assignments were made from

vibrational assignments for similar β-diketone complexes in the literature.[22,23,24]
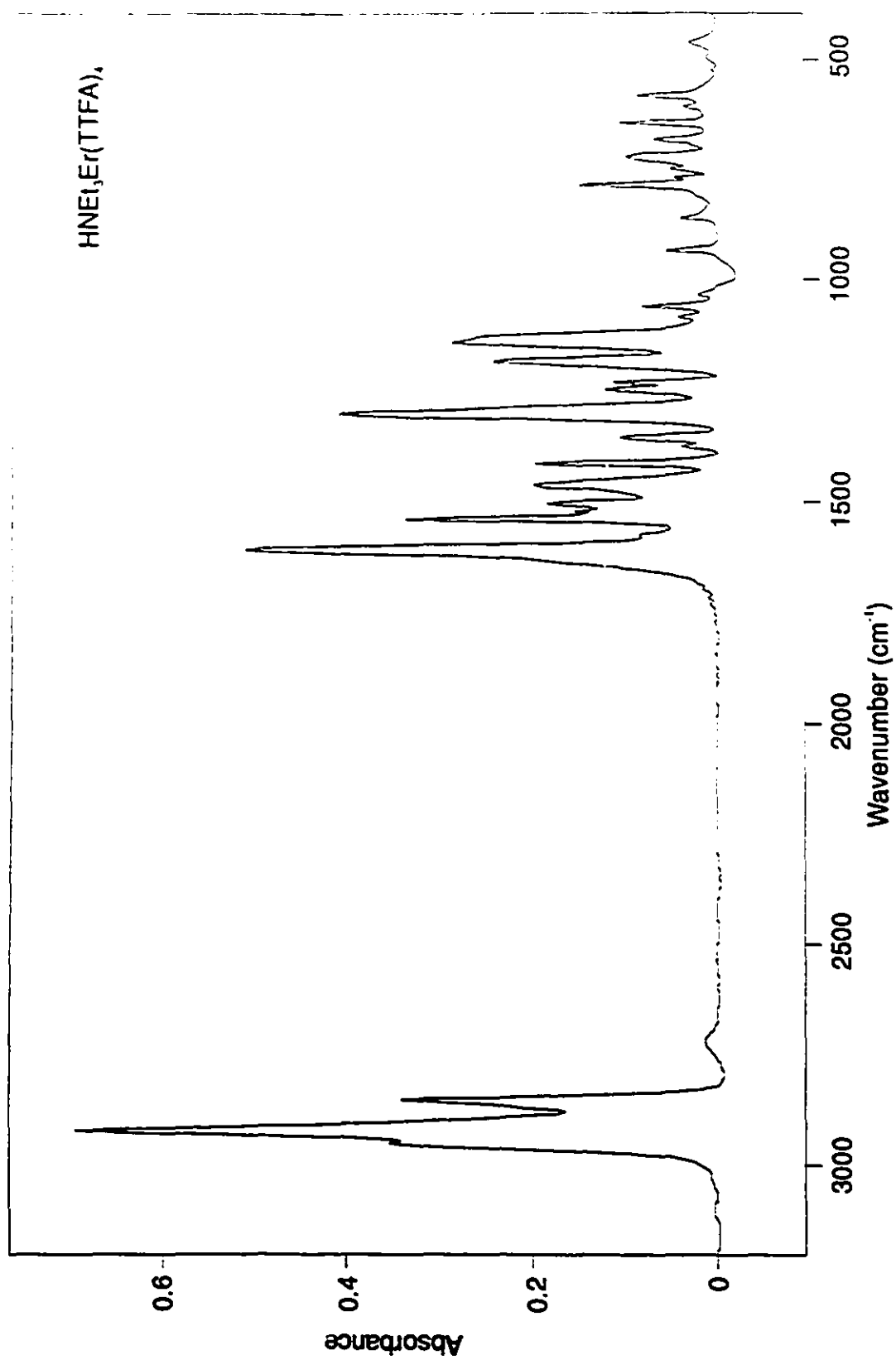
Figure 3.4 FTIR spectrum of HNEt₃Er(TTFA)₄ (KBr disk)

Table 3.4 *Observed vibrational frequencies (cm⁻) and assignments for Erbium-TTFA complexes[a].*

HNEt₃Er(TTFA)₄	NPr₂Er(TTFA)₄	Assignment[b]
1608 vs	1612 vs	v_{as} (C=O)
1577 sh	1568 w	
1541 s	1537 s	v_{as} (C=C=C)
1521 m	1520 m	
1504 m	1502 m	
1463 m	1475 m	δ (C-H) and v (C=O)
1413 m	1414 m	v (thenoyl ring)
1376 w	1390 w	
1356 m	1355 m	v_s (C=O)
1304 vs	1302 vs	v_{as} (CF₃)
1248 m	1244 m	v (C-CF₃) and v_s (C=C)
1230 m	1230 m	
1184 s	1178 m	δ (C-H)
1141 s	1140 s	v_s (CF₃)
1084 w	1084 w	
1061 m	1061 m	$δ_{ip}$ (C-H thenoyl ring)
935 w	933 w	$δ_{oop}$ (C-H)
858 w	858 w	
783 m	783 m	$δ_{oop}$ (C-H thenoyl ring)
767 w	767 w	
746 w	748 w	
721 m	725 m	$δ_{oop}$ (C-C thenoyl ring)
	692 w	
680 m	679 w	δ (C-S)
644 m	642 m	$δ_{oop}$ (CF₃—C⟨C / O⟩)
605 w	605 w	δ (CF₃)
580 m	580 m	ring deformation
	520 w	
496 w	492 w	
461 w	463 w	v (Er-O and C-R*)[c]

[a] Abbreviations used for band descriptions: vs, very strong; s, strong; m, medium; w, weak; sh, shoulder.

[b] Vibrational mode descriptions: v, stretching; δ, bending; as, asymmetric; s, symmetric; ip, in-plane; oop, out-of-plane.

[c] R*=CF₃ or φ

92
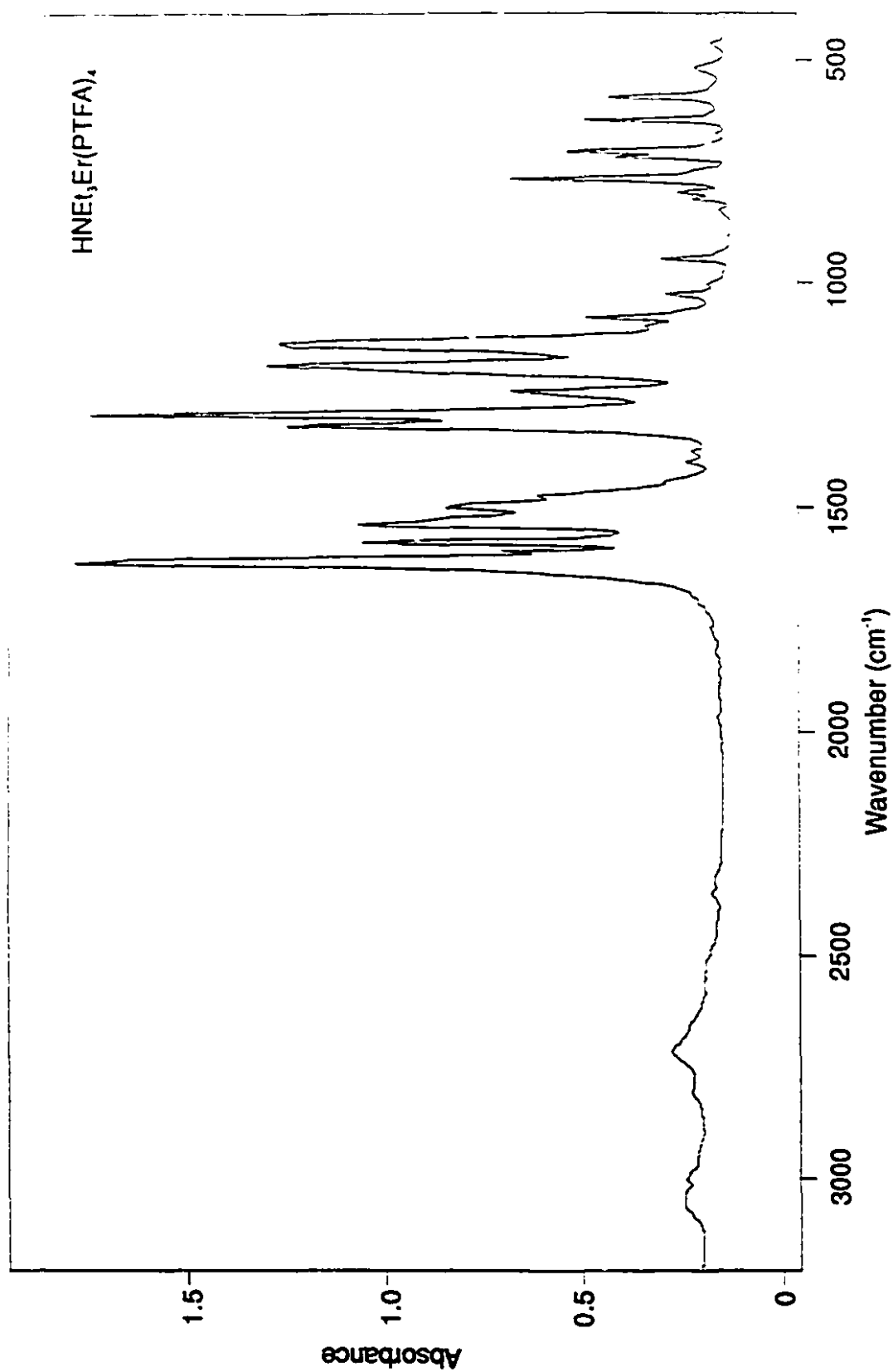
Figure 3.5 FTIR spectrum of HNEt₃Er(PTFA)₄ (KBr disk)

Table 3.5 Observed vibrational frequencies (cm^{-1}) and assignments for Erbium-PTFA complexes[a]

HNEt$_3$Er(PTFA)$_4$	NEt$_4$Er(PTFA)$_4$	Assignment[b]
1626 vs	1626 vs	ν_{as} (C=O)
1618 sh		
1598 m	1598 m	ν (ϕ ring)
1577 s	1579 m	ν (ϕ ring)
1539 s	1537 m	ν_{as} (C=C=C)
1500 m	1504 m	ν (ϕ ring)
1475 m	1479 m	δ (CH) and ν (C=O)
1442 sh	1441 w	
1398 w	1394 w	
1319 s	1319 s	ν_s (C=O)
1292 vs	1292 vs	ν_{as} (CF$_3$)
1242 m	1242 m	ν (C-CF$_3$)and ν_s (C=C)
1184 s	1184 s	δ (C-H)
1134 s	1130 s	ν_s (CF$_3$)
1097 sh	1097 sh	
1078 m	1078 m	δ_{ip} (ϕ C-H)
1026 w	1026 w	δ_{ip} (ϕ C-H)
1001 w	1001 w	
947 w	945 w	δ_{oop} (C-H)
837 w		
810 w	808 w	δ_{oop} (ϕ C-H)
794 w	794 w	δ_{oop} (ϕ C-H)
764 m	764 m	δ_{oop} (ϕ C-H)
717 m	717 m	δ_{oop} (ϕ C-C)
704 m	702 m	δ_{oop} (ϕ C-C)
632 m	632 m	$\delta_{oop}\left(CF_3-C\underset{O}{\overset{C}{<}}\right)$
580 m	580 m	ring deformation
517 w	519 w	δ_{ip} (ϕ ring)
463 w	463 w	ν(Er-O) and ν(C-R*)[c]
440 w	428 w	δ_{ip} (ϕ ring)

[a]Abbreviations used for band descriptions: vs, very strong; s, strong; m, medium; w, weak; sh, shoulder.

[b]Vibrational mode descriptions: ν, stretching; δ, bending; as, asymmetric; s, symmetric; ip, in-plane; oop, out-of-plane.
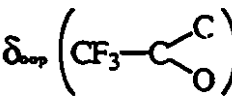
[c]R*=CF$_3$ or ϕ

Figure 3.6 FTIR spectrum of HNEt₃Er(HFA)₄ (KBr disk)

HNEt₃Er(HFA)₄

Table 3.6 *Observed vibrational frequencies (cm^{-1}) and assignments for Erbium-HFA complex*[a]

HNEt$_3$Er(HFA)$_4$	Assignment[b]
1655 s	v_{as} (C=O)
1610 w	
1560 m	v_{as} (C=C)
1533 m	
1514 m	
1481 sh	
1402 w	
1350 w	
1255 s	v (CF$_3$)
1218 m	v_s (C=C) and v (C-CF$_3$)
1201 m	
1145 vs	δ (C-H)
1099 m	
1032 w	
951 w	δ_{oop} (C-H)
800 m	
767 w	
742 w	
661 m	$\delta_{oop}\left(CF_3-C\overset{C}{\underset{O}{<}}\right)$
588 m	ring deformation
528 w	
470 w	v (Er-O) and v (C-CF$_3$)

[a]Abbreviations used for band descriptions: vs, very strong; s, strong; m, medium; w, weak; sh, shoulder.

[b]Vibrational mode descriptions: v, stretching; δ, bending; as, asymmetric; s, symmetric; ip, in-plane; oop, out-of-plane.

Near infrared (NIR) spectra were taken between 0.9 and 1.7 μm of all the complexes dissolved in acetone. Of particular interest were the transitions centred at 0.980 μm ($^4I_{11/2} \leftarrow {}^4I_{15/2}$) and at 1.55 μm ($^4I_{13/2} \leftarrow {}^4I_{15/2}$). All spectra displayed a relatively sharp structured absorption peak at ~0.975 μm, and a much broader absorption centred around 1.52 μm consisting of several overlapping peaks. Again, there were no differences between the spectra of the two TTFA complexes, or the two PTFA complexes, indicating the counterion had no effect on absorption in this region. Spectra of the complexes with different ligands were very similar in appearance. There were some very slight differences in the shapes and intensities of the bands near 1.52 μm; however, no great differences in either this transition or the one at 975 μm were to be expected. Recall that absorption bands for f-f electronic transitions show little dependence on the nature of the ligand. The only major difference was the intensity and position of a band near 1.64 μm which was attributed to the ligand. This was determined from NIR spectra of the ligand in acetone. Thus, the peaks arising from the $^4I_{11/2}$ and $^4I_{13/2}$ states are essentially ligand insensitive. Spectra of the erbium complexes derived from three different ligands with triethylammonium counterion, dissolved in acetone, are shown in Fig. 3.7.
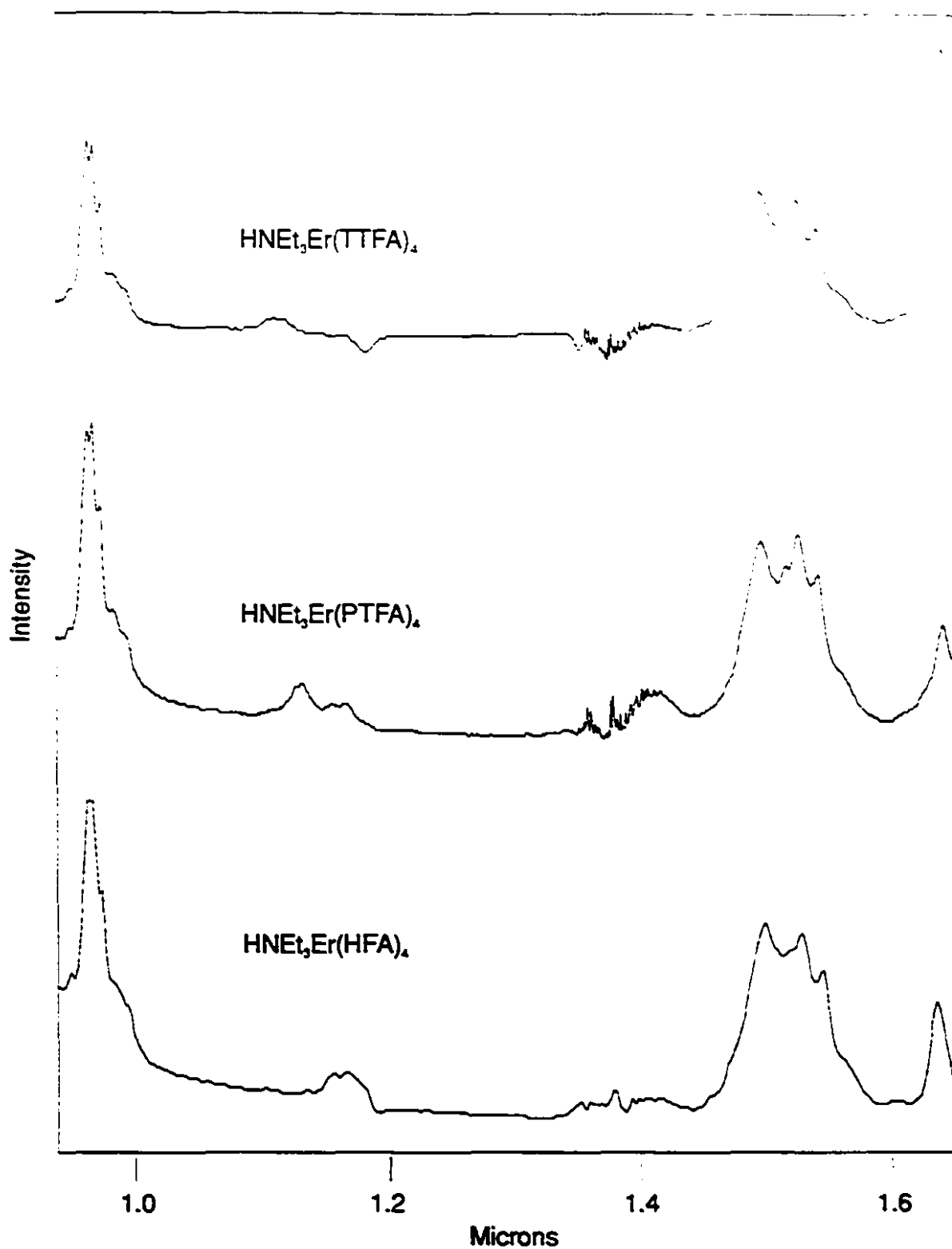
Figure 3.7 NIR spectra of HNEt₃Er(TTFA)₄, HNEt₃Er(PTFA)₄, and HNEt₃Er(HFA)₄ in acetone

98

Two of the complexes ($HNEt_3Er(TTFA)_4$ and $HNEt_3Er(HFA)_4$) were dissolved in DMF and ethanol to study the effect of solvent environment on the NIR spectra of the complexes. The erbium ion can be thought of as a Lewis acid and the solvents as Lewis bases. As lone pairs on solvent molecules bring electron density into the erbium cation (donor-acceptor interactions), it is expected that the spectrum will be perturbed. Solvent polarity may influence the degree to which the spectrum is perturbed. DMF has a higher dipole moment than acetone while ethanol has a lower dipole moment. There is also some incentive to see how the hydroxyl group of ethanol might perturb the spectra. OH oscillators are known to quench luminescence of lanthanide ions as the hydroxyl density of states are resonant with the lanthanide ion excited state levels.[9] Thus it is useful to probe the erbium $^4I_{13/2}$ level to see the effect of hydroxyl groups. As can be seen in Fig. 3.8 for the TTFA complex and in Fig. 3.9 for the HFA complex, there were indeed some changes.

For both complexes, the absorption at 0.975 μm was slightly sensitive to solvent. We observe no shift in peak position, and only slight changes in peak intensity. The structure of this band is less well resolved in DMF and ethanol as compared to acetone. The ligand band near 1.64 μm was solvent insensitive for both complexes. By contrast we observe significant perturbation associated with the absorption centred around 1.52 μm.

DMF caused the band profile of the $^4I_{13/2} \leftarrow {}^4I_{15/2}$ transition in the spectrum of the TTFA complex (top spectrum, Fig. 3.8) to exhibit a slight increase in intensity as compared with the spectrum obtained in acetone. Ethanol, however, severely perturbed this transition (bottom spectrum, Fig. 3.8). The resolvable peaks that were present in the acetone and DMF spectra near 1.52 μm were replaced by a very noisy, broad absorption

band in the ethanol spectrum. The peaks corresponding to the $^4I_{13/2} \leftarrow {}^4I_{15/2}$ transition in the spectrum of the HFA complex in DMF (top spectrum, Fig. 3.9) had less resolution and a slight red shift, as well as an increase in intensity as compared to the acetone spectrum. Again, ethanol had a much larger effect on this transition (bottom spectrum, Fig. 3.9). The band near 1.52 μm was broadened and very noisy, with less resolution compared to the other two spectra.
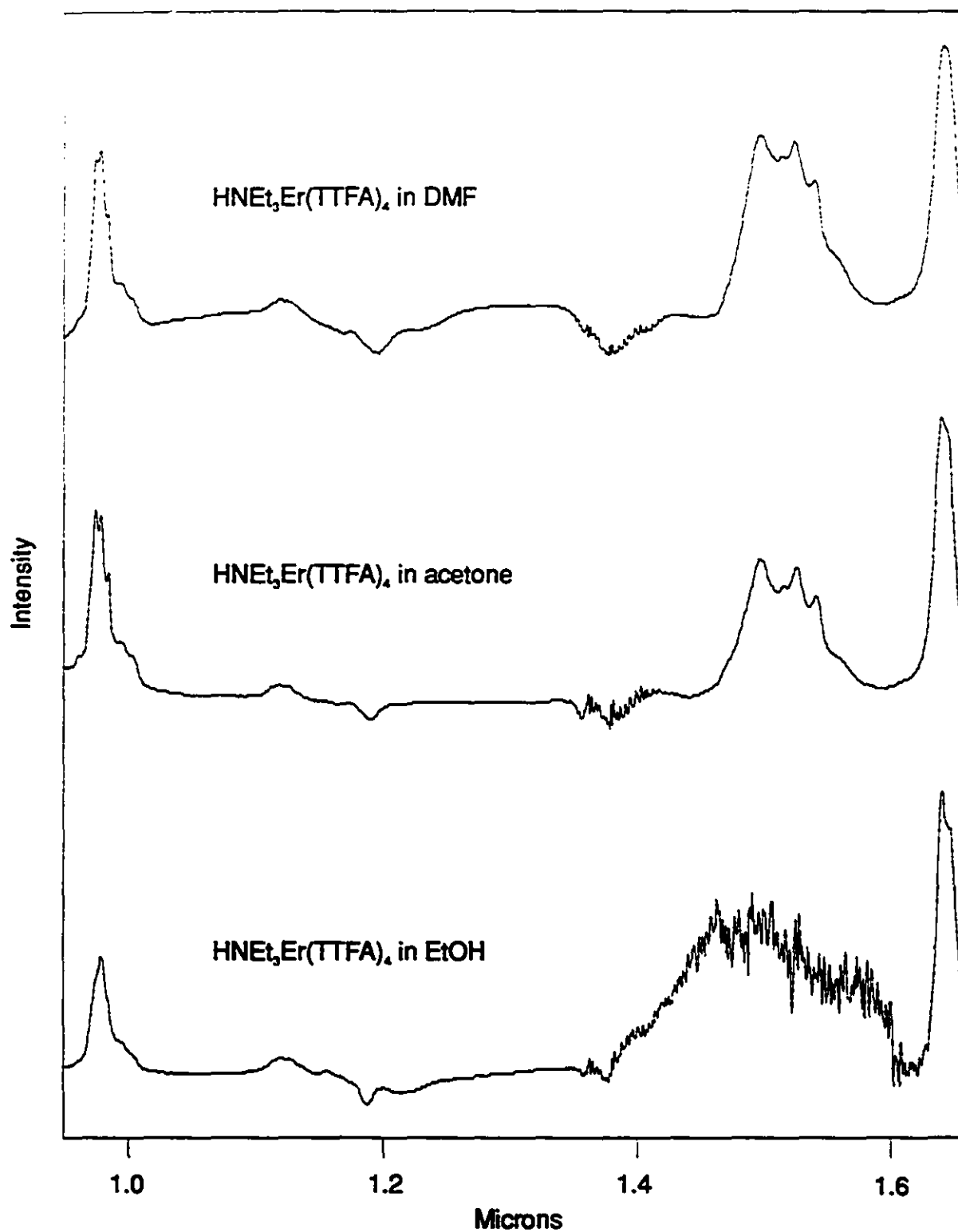
Figure 3.8 NIR spectra of HNEt₃Er(TTFA)₄ in different solvents, showing large perturbation in presence of hydroxyl groups
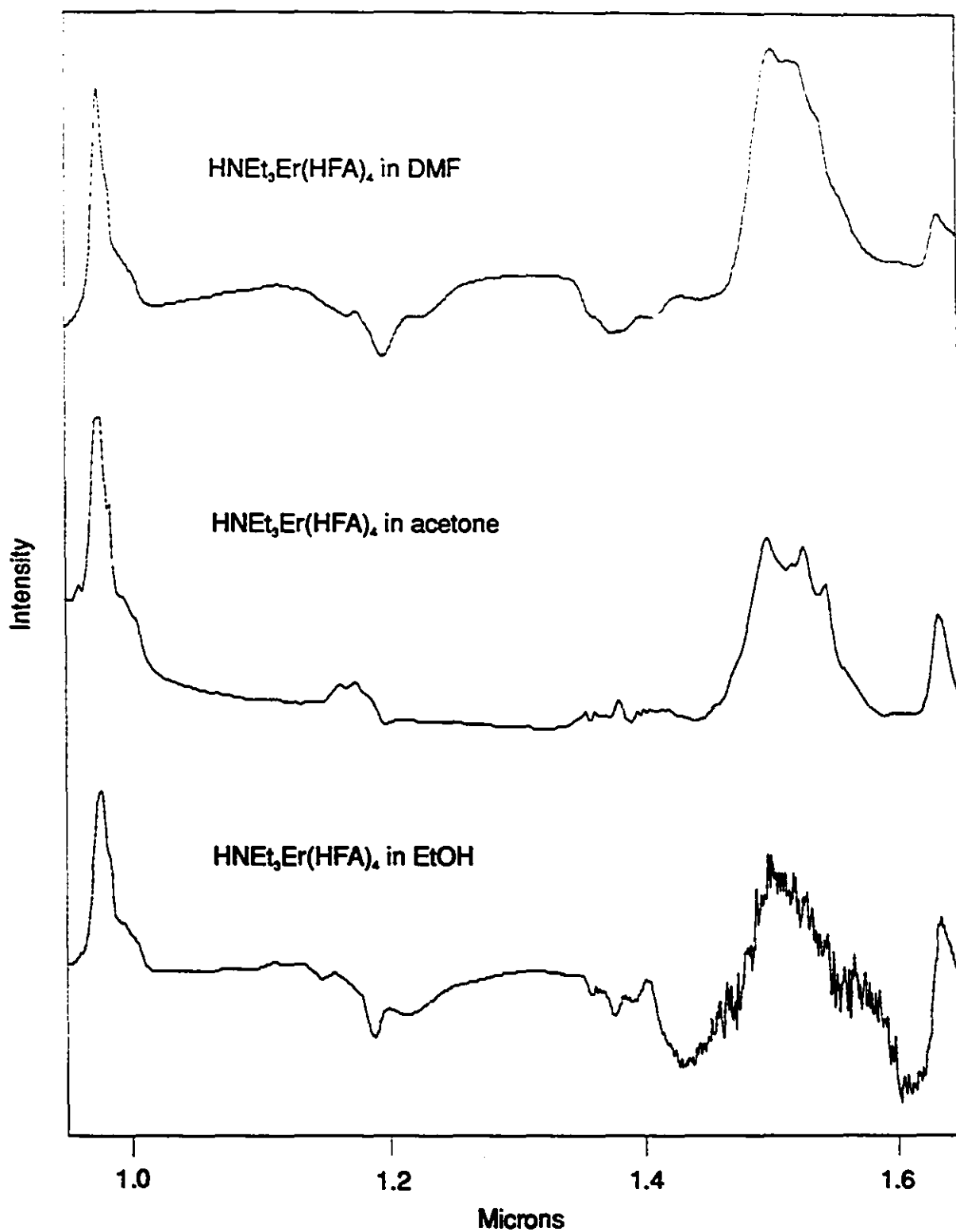
Figure 3.9 NIR spectra of HNEt₃Er(HFA)₄ in different solvents, showing large perturbation in presence of hydroxyl groups

From these observations, we can conclude that the $^4I_{11/2} \leftarrow {}^4I_{15/2}$ transition at

0.975 μm shows only a weak solvent effect, whereas the $^4I_{13/2} \leftarrow {}^4I_{15/2}$ transition near

1.52 μm is very sensitive to its surroundings. This suggests that in these complexes, there

is some access to the erbium ion in a liquid solvent environment. We do not know to what

degree solvent molecules can penetrate the coordination sphere; however, complete

shielding of the erbium ion in these complexes does not occur. The presence of hydroxyl

groups has a very large perturbation on the $^4I_{13/2} \leftarrow {}^4I_{15/2}$ transition in the spectra of both

complexes. This helps to explain the problem of luminescence quenching in erbium doped

sol-gel glasses. Residual hydroxyl groups are most probably responsible since there is

clearly a hydroxyl perturbation on this transition. The effect of solvent polarity seems to be

minimal.

NIR is an extremely useful spectroscopic probe of the $^4I_{13/2}$ excited state of Er^{3+}.

This state has been shown to be extremely sensitive to its environment, and further studies

will allow systematic investigations into guest-host interactions.

3.3.2. Erbium β-Diketone Complexes in Sol-Gel Glasses

Erbium doped sol-gels were prepared both in bulk and thin film forms. Dopants

included erbium in the form of the previously discussed coordination complexes and as

salts. All of the erbium complexes, erbium acetate, and $Er(NO_3)_3$ were very soluble in the

ormocer sol. Monoliths of the ormocer were not obtained because as the gel dried, it

adhered to the container walls resulting in uneven shrinkage and cracking. In addition, the

dried gel was rather soft. No attempt was made to investigate drying conditions which

may have resulted in better samples. Only two dopants were soluble in the MTMS sol-gel: $HNEt_3Er(HFA)_4$ and $HNEt_3Er(TTFA)_4$. The HFA complex was very soluble at high concentrations and beautiful pink monoliths were readily obtained. The TTFA complex was only soluble at low concentrations. At higher concentrations, it was soluble at the reaction temperature of 75°C, but on cooling, it began to crystallize out of the sol. No investigations were made to optimize doping levels in either sol-gel.

NIR spectra were taken of the ormocer sol, both undoped and doped with the $HNEt_3Er(PTFA)_4$ complex. These are displayed in Fig. 3.10. Also shown is the doped spectrum with the undoped spectrum subtracted. The undoped spectrum exhibits a very broad absorption from about 1.35 μm to beyond 1.7 μm. The spectrum of the doped sol was very similar to the undoped sol. There was a very small peak at 0.980 μm and one at 1.53 μm. These two peaks became more apparent when the undoped spectrum was subtracted from the doped spectrum. Further studies into which sol-gel components give rise to the absorptions in this region may permit some material modifications to reduce absorption.
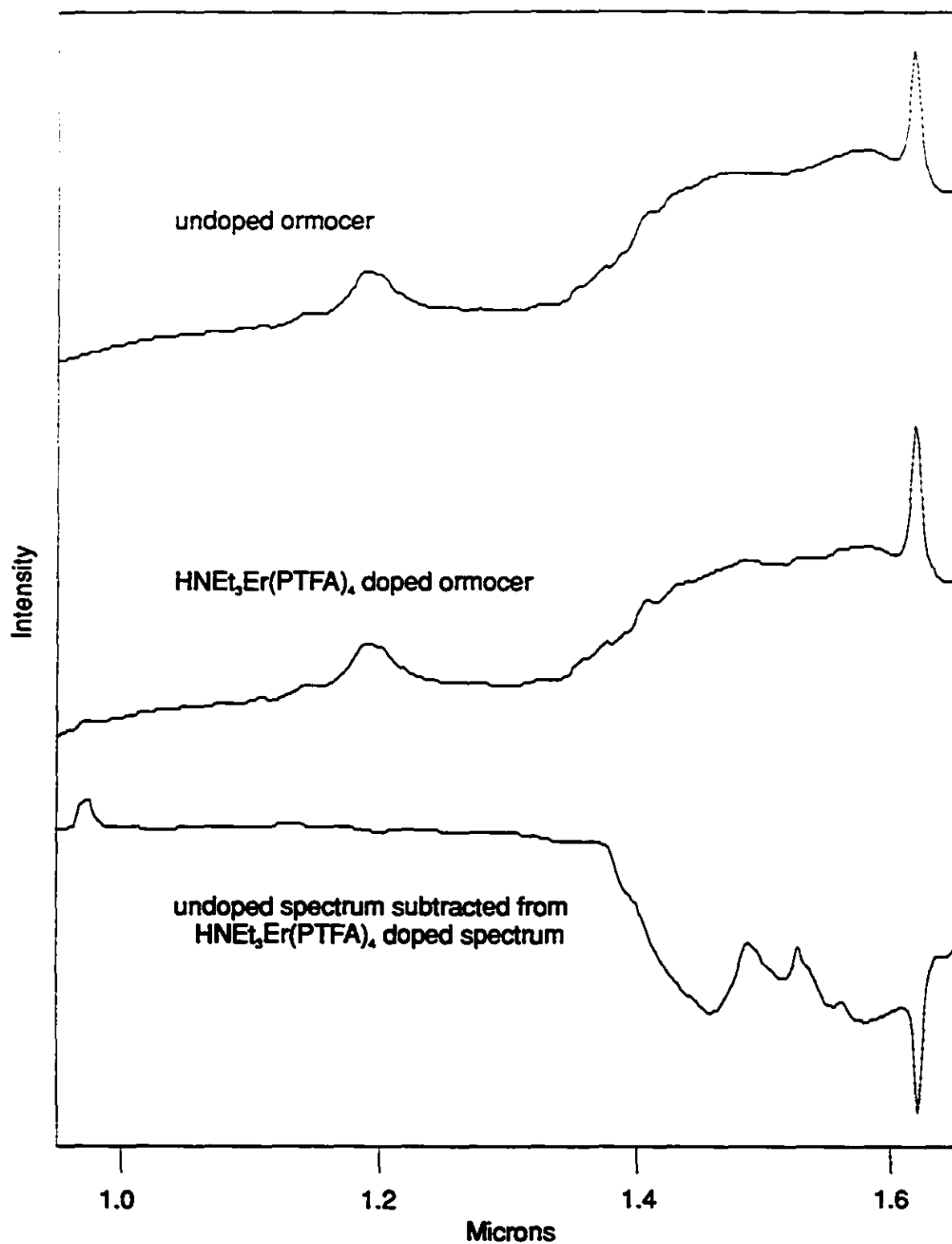
Figure 3.10 NIR spectra of undoped and HNEt₃Er(PTFA)₄ doped ormocers, and subtracted spectrum

Note: figure labels read: "undoped ormocer", "HNEt₃Er(PTFA)₄ doped ormocer", "undoped spectrum subtracted from HNEt₃Er(PTFA)₄ doped spectrum", y-axis "Intensity", x-axis "Microns" with markings 1.0, 1.2, 1.4, 1.6.

NIR spectra of undoped and $HNEt_3Er(HFA)_4$ doped MTMS sol-gel monoliths are shown in Fig. 3.11. The 0.980 μm absorption in the doped sample occurs in a region where there is minimal absorption in the MTMS host. There is a very large absorption in the doped sample in the 1.52 μm region; however, there is an absorption in the undoped MTMS sol-gel in the same region which may cause some interference. Other peaks arising from the MTMS host are observed at 1.19 and 1.40 μm. A spectrum of the doped sample with the undoped sample subtracted (relative to the peak at 1.40 μm) is shown in Fig. 3.12. The peak at 0.978 μm is basically unchanged, while the peak near 1.52 μm resembles the spectra of the complex dissolved in DMF, in that there are some resolvable peaks with a very similar shape. At this point, it is unclear as to whether or not MTMS is a suitable host for erbium complexes. Further studies to investigate the origin of the peak at 1.55 μm and to what extent, if any, it interferes with the erbium ion absorption/emission may determine the suitability of MTMS as a host for erbium.
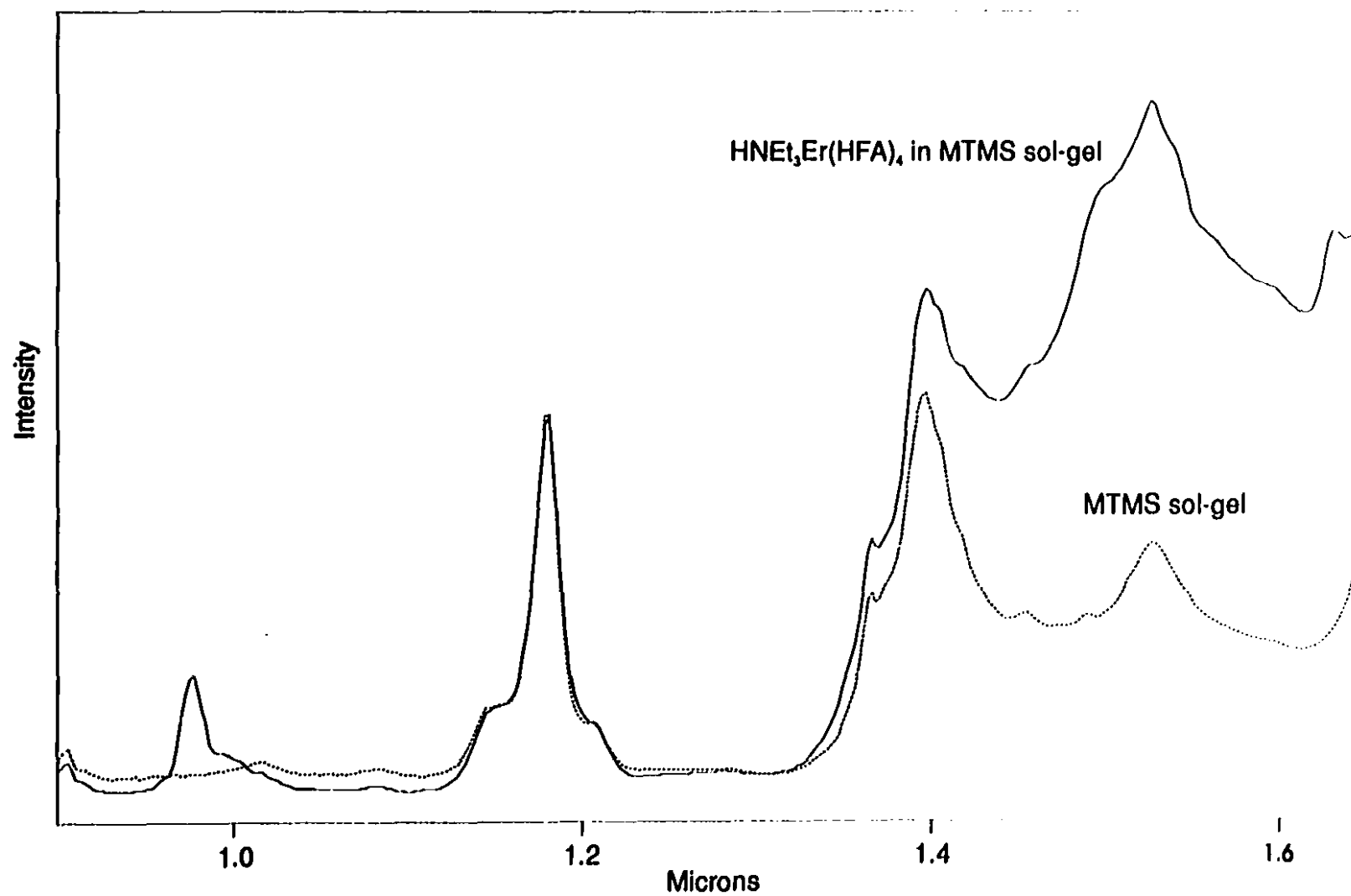
Fig. 3.11 Comparison of HNEt₃Er(HFA)₄ doped MTMS sol-gel with undoped MTMS sol-gel
(referenced to peak at 1.18 microns)
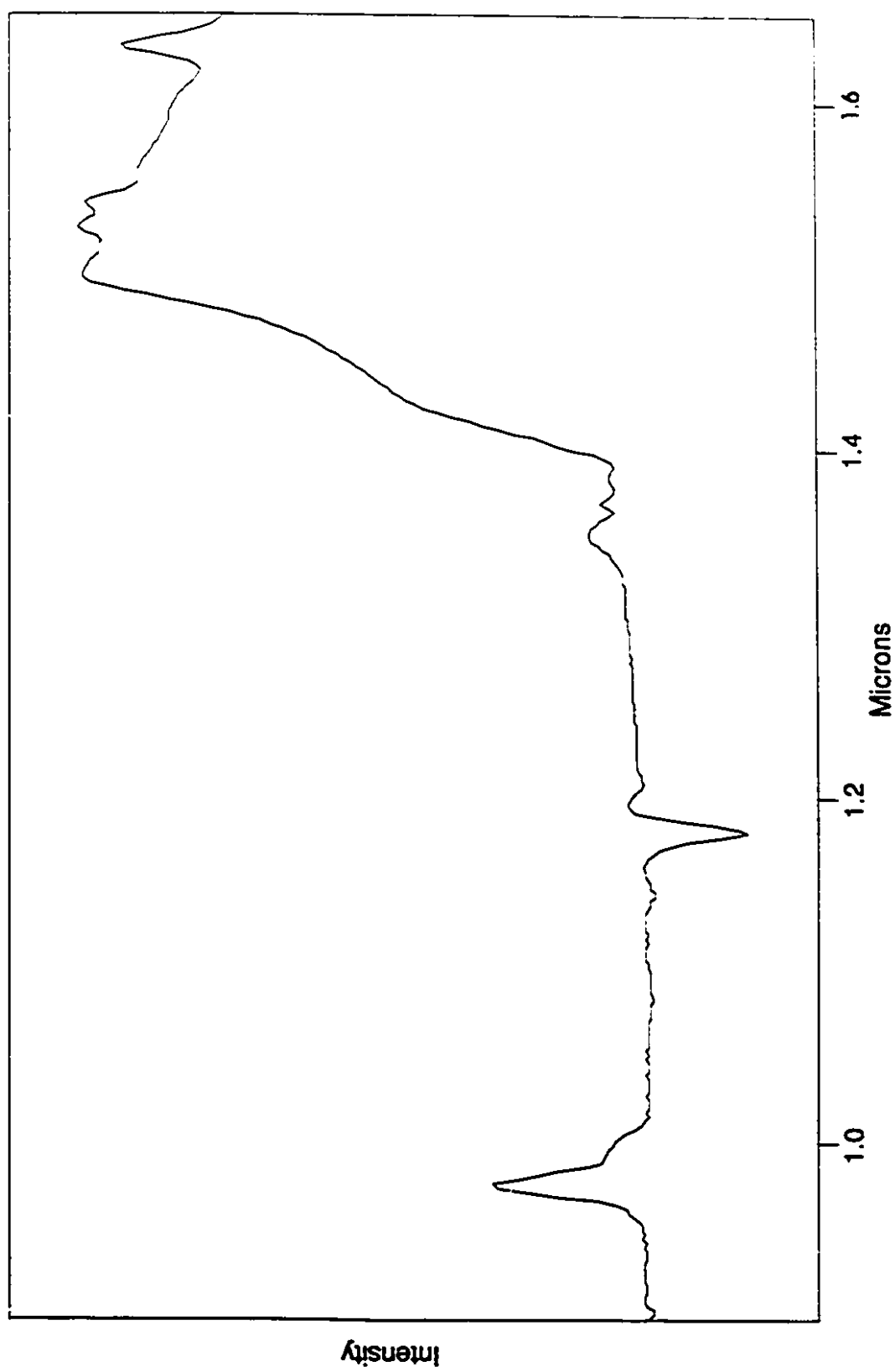
Fig. 3.12 Subtraction of undoped MTMS sol-gel spectrum from HNEt₃Er(HFA)₄ doped MTMS sol-gel spectrum (referenced to peak at 1.4 microns)

108

Several attempts were made to obtain luminescence from bulk samples of the erbium doped ormocer and MTMS sol-gels. Attempts were also made with erbium doped channel waveguides fabricated in the ormocer using the photolithographic technique described in Chapter 2, Section 2.3.2. All samples were pumped with light from a tunable Ti:sapphire laser operating near 0.980 μm. No luminescence was observed in any of the samples. It is unclear at this time whether this is due to problems with the experimental set-up or the samples. Improvements to the collection optics may improve results.

A very weak luminescence signal was observed in an erbium doped ormocer sol at the Optical Sciences Center at the University of Arizona as shown in Fig. 3.13.[25] The dopant was KEr(TTFA)₄.
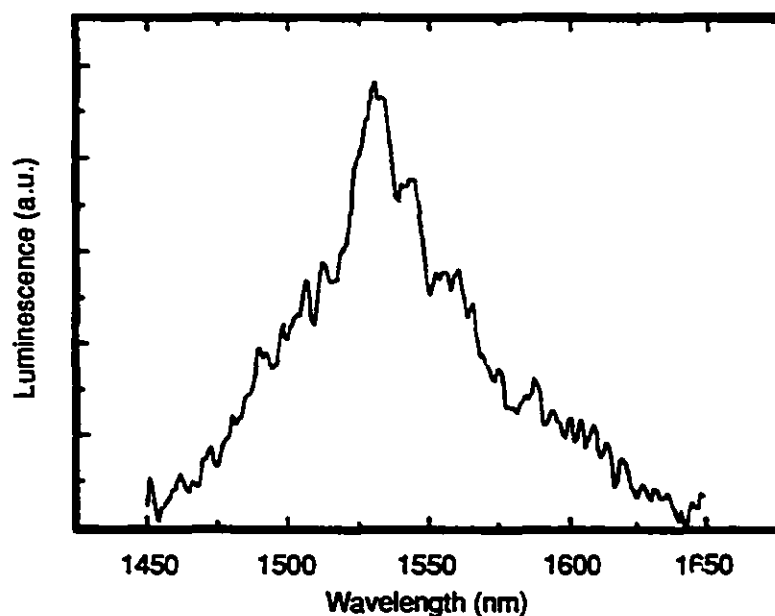
Figure 3.13 Luminescence spectrum of an erbium doped ormocer sol

This is the first example of the observation of luminescence from an erbium complex doped into an organically modified sol-gel glass.

3.4. Conclusions

Several tetrakis erbium β-diketonate coordination complexes were synthesized, of which the TTFA and PTFA complexes are believed to be novel. A crystal structure of the $NEt_4Er(PTFA)_4$ complex was obtained and showed that the complexes are tetrakis octacoordinate, with tetragonal antiprism coordination about the erbium ion. NIR proved to be an extremely useful tool for the study of perturbations of the $^4I_{13/2}$ excited state in different hosts. This state is very sensitive to the host environment, while the $^4I_{11/2}$ state is relatively insensitive. The above complexes were doped into both the ormocer and the MTMS sol-gels. The ormocer was able to dissolve all complexes at relatively high concentrations; however, monoliths were not produced. The ormocer sol absorbs in the region around 1.5 μm, and thus may not be an ideal host for erbium. The MTMS was able to dissolve the HFA and TTFA complexes and produce sol-gel monoliths. MTMS sol-gels have an absorption near 1.5 μm, which may interfere with the erbium ion, thus further studies are required to determine the suitability of this host. A very weak luminescence signal from an erbium doped ormocer sol was observed. Several other attempts to observe luminescence proved unsuccessful. Improvements to the experimental setup may lead to positive results. Future investigations into the source of host absorptions near 1.5 μm may permit some material modifications to reduce these absorptions and improve host compatibility with erbium.

3.5. References

1. K. Arai, H. Namikawa, K. Kumata, T. Honda, Y. Ishii and T. Handa, *J. Appl. Phys.*, **59**, 3430, (1986).

2. R.J. Mears, L. Reekie, I.M. Jauncey and D.N. Payne, *Electron. Lett.*, **23**, 1026, (1987).

3. K.J. Malone, In *Glass Integrated Optics and Optical Fiber Devices*, S.I. Najafi, Ed., SPIE, Bellingham, WA, 1994.

4. W.J. Miniscalco, *J. Lightwave Tech.*, **9**, 235, 1991.

5. T. Kitigawa, K. Hattori, K. Shuto, M. Yasu, M. Kobayashi and M. Horiguchi, *Electron. Lett.*, **28**, 1818, (1992).

6. L. Lee and D. Tsai, *J. Mater. Sci. Lett.*, **13**, 615, (1994).

7. T. Fujiyama, M. Hori, M. Sasaki, *J. Non-Cryst. Solids*, **121**, 273, (1990).

8. K. Arai, H. Namikawa, Y. Ishii, H. Imai, and H. Hosono, *J. Non-Cryst. Solids*, **95&96**, 609, (1987).

9. N. Sabbatini, M. Guardigli and J-M. Lehn, *Coord. Chem. Rev.*, **123**, 201, (1993).

10. G. Stein and E.Wurzberg, *J. Chem. Phys.*, **62**, 208, (1975).

11. H. Samuelson and A. Lempicki, *J. Chem. Phys.*, **39**, 110, (1963).

12. L.R. Melby, N.J. Rose, E. Abramson and J.C. Caris, *J. Am. Chem. Soc.*, **86**, 5117, (1964).

13. H. Bauer, J. Blanc and D.L. Ross, *J. Am. Chem. Soc.*, **86**, 5125, (1964).

14. C. Breecher, H. Samuelson and A. Lempicki, *J. Chem. Phys.*, **42**, 1081, (1964).

15. R.G. Charles and E.P. Reidel, *J. Inorg. Nucl. Chem.*, **29**, 715, (1966).

16. K.C. Joshi and V.N. Pathak, *J. Inorg. Nucl. Chem.*, **35**, 3161, (1972).

17. L.R. Matthews and E.T. Knobbe, *Chem. Mater.*, **5**, 1697, (1993).

18. T. Moeller, *The Chemistry of theLanthanides*, Reinhold Publishing Corp., New York, 1963.

19. R.G. Charles and E.P. Reidel, *J. Inorg. Nucl. Chem.*, **28**, 3005, (1966).

20. P.T. Moseley. In *Inorganic Chemistry Series Two. Volume 7. Lanthanides and Actinides*. Butterworth & Co., London, 1975.

21. F.A. Cotton and G. Wilkinson. *Advanced Inorganic Chemistry*. John Wiley & Sons, New York, 1980.

22. C.Y. Liang, E.J. Schimitschek aand J.A. Trias. *J. Inorg. Nucl. Chem.*, **32**, 811, (1970).

23. J.R. Ferraro and T.V. Healy. *J. Inorg. Nucl. Chem.*, **24**, 1467, (1962).

24. K. Nakamoto. *Infrared and Raman Spectra of Inorganic and Coordination Compounds*. John Wiley & Sons, New York, 1986.

25. C-Y. Li, J. Ingenhoff, S.I. Najafi, J. Chisham, M. MacLachlan, M. Andrews, Y. Kao, J.D. Mackenzie, T. Ohtsuki and N. Peyghambarian. *Optoelectronic Integrated Circuit Materials, Physics and Devices. SPIE Proc.*, **2397**, 430, (1995).

Appendix 1. X-Ray Crystallography Data

Discussion of structure determination and refinement procedure

Pale pink crystals of [(PTFA)4Er]NEt4 were obtained from ethanol. Compound is monoclinic, C2/c. Data was collected over 4 octants to allow for averaging. Data was processed by the NRCVAX package (Gabe et al 1989). The structure was solved by direct method using SHELXS-86 (Sheldrick, 1986) and difmap synthesis and refined using SHELXL-93 (Sheldrick, 1995). Anion sits in general position (Z=8). Two of the four PTFA ligands have disordered fluorines in the CF3 group. On both cases the occupancies for the disordered atoms were refined (final values 0.54 and 0.46) and fixed at these values. Thermal parameters were then refined. Geometries for both orientations of disordered CF3 groups were restrained to be similar the undisordered group formed by C34, F10, F11 and F12. There are two cations on twofold sites (Z=4 each). Both NEt4 groups are disordered.

All non-hydrogen atoms anisotropic. Hydrogen atoms were calculated at idealized positions using a riding model with different C-H distances for type of hydrogen. The isotropic displacement factors, U_{iso}, were adjusted to 30% higher value of the bonded carbon atom (methyl) and 20% higher (others). Hydrogens for methyl groups of NEt4 no 1 were not introduced in the model. Principal crystallographic data are in Table 1.

The Erbium atom has tetragonal antiprism coordination.

REFERENCES

Data reduction

Gabe E.J., LePage Y. Charland J.P. Lee F.L. and White P.S.
NRCVAX: J. Appl. Cryst. 22, 384-389, 1989.

Structure solution
Sheldrick, G.M. (1985). SHELXS-86.
Program for the Solution of Crystal Structures, Univ. of Gottingen, Germany.

Structure refinement
Sheldrick, G.M. (1995). SHELXL-93.
Program for Structure Analysis. J. Appl. Cryst. In preparation.

Molecular graphic
Johnson, C.K. (1976). ORTEPII. Report ORNL-5138.
Oak Ridge National Laboratory, Tenessee, USA.
Gabe, E.J., Le Page, Y., Charland, J.-P., Lee, F.L. and White, P.S. (1989).
J.Appl. Cryst. 22, 384-387.

Material for publication
Sheldrick, G.M. (1995). SHELXL-93.
Program for Structure Analysis. J. Appl. Cryst. In preparation.

Source of atomic scattering factors
International Tables for Crystallography (1992).
Vol. C. Tables 4.2.6., Dordrecht: Kluwer Academic Publishers.

Table 1. Crystal data and structure refinement for [(PTFA)4Er]NEt4.

Crystal Data

Crystal source	
Chemical formula, sum	C48 H48 Er F12 N O8
Chemical formula, moiety	[(C10H7O2F3)4Er]N(C5H5)4
Chemical formula weight, Mr	1162.13
Cell setting	Monoclinic
Space group	C 2/c
Unit cell dimensions (Å, °)	a = 23.428(8)α = 90
	b = 22.727(3)β = 120.59(2)
	c = 21.678(7)γ = 90
Volume of unit cell, V (Å³)	9936(5)
Formula units per cell, Z	8
Density calculated from	
formula and cell, Dx (Mg/m³)	1.554
F(000)	4664
Radiation type	Molybdenum Kα
Wavelength, lambda (Å)	0.70930
No. of reflections	
for cell measurement	24
Theta range (deg)	10 to 15
Linear absorption coefficient, mu (mm⁻¹)	0.125
Measurement temperature (K)	293(2)
Crystal shape	prism
Colour	light pink
Size (mm)	0.42 x 0.30 x 0.08

Data collection

Diffractometer type	Rigaku AFC6S
Data-collection method	ω/2Θ scans
Absorption correction type	None
Maximum and minimum transmission	
No. of reflections measured	17711
No. of independent reflections (Rint)	8754 (0.068)
No. of observed reflections	4924
Criterion for observed reflections	I>2σ(I)
Min. and max values of θ (°)	2.00 to 25.00
Ranges of h,k,l	-27<=h<=23, 0<=k<=27, 0<=l<=25
No. of standard reflections	3
Interval, (no reflections)	200
Intensity decay (%)	0.77

Refinement

Refinement method	Full-matrix on F^2
Final R indices, I>2σ(I)	R1 = 0.0666, wR2 = 0.1301
R indices, all data	R1 = 0.1296, wR2 = 0.1530
Goodness-of-fit on F^2, S	0.961

R1 = sum (absabs Foabs -abs Fcabsabs)/sum (abs Foabs),
wR2 = $[\Sigma \, [w(Fo^2-Fc^2)^2]/\Sigma \, [w(Fo^2)^2]]^{1/2}$ and
GoF = $[\Sigma \, [w(Fo^2-Fc^2)^2]/(\text{No. of reflns - No. of params.})]^{1/2}$

No. of reflections used in refinement	8754
No. of parameters refined	736
No. of restraints	106
Method of locating and refining H atoms	calculated/riding
Weighting scheme	based on measured e.s.d's
Function minimized	$\Sigma \, w(Fo^2-Fc^2)$

calc w=1/[\s^2(Fo^2)+(0.0725P)^2+0.0000P] where P=(Fo^2+2Fc^2)/3

Maximum shift/sigma	-0.183
Δ rho max (e Å^{-3})	1.421
Δ rho min (e Å^{-3})	-1.831
Δ rho background (e Å^{-3})	0.62

Source of atomic scattering factors	International Tables for Crystallography (1992)

Table 2. Atomic coordinates and equivalent isotropic
displacement parameters ($\text{Å}^2 \times 10^2$) for [(PTFA)4Er]NEt4.

$U_{eq} = (1/3)\,\text{sum}_i\,\text{sum}_j\,U_{ij}\,a^*_i\,a^*_j\,a_i\,a_j.$

	x	y	z	U_{eq}
Er	0.25640(2)	0.12139(2)	0.73907(2)	4.258(13)
O(1)	0.2966(3)	0.1490(2)	0.6644(3)	5.3(2)
O(2)	0.2828(3)	0.0367(3)	0.6990(3)	5.6(2)
O(3)	0.1898(3)	0.0486(3)	0.7462(3)	5.9(2)
O(4)	0.1614(3)	0.1143(3)	0.6282(3)	5.6(2)
O(5)	0.2187(3)	0.1579(3)	0.8116(3)	5.6(2)
O(6)	0.3219(3)	0.0736(3)	0.8504(3)	5.2(2)
O(7)	0.2182(3)	0.2168(2)	0.7035(3)	5.7(2)
O(8)	0.3463(3)	0.1810(3)	0.8081(3)	5.6(2)
C(1)	0.2951(4)	0.1271(4)	0.6104(4)	5.1(2)
C(2)	0.2799(5)	0.0673(4)	0.5929(5)	6.3(3)
C(3)	0.2768(4)	0.0270(4)	0.6396(5)	5.6(2)
C(4)	0.2676(7)	-0.0366(5)	0.6171(6)	9.7(4)
F(1)	0.3239(4)	-0.0655(3)	0.6497(6)	16.5(4)
F(2)	0.2287(4)	-0.0659(3)	0.6310(4)	12.9(3)
F(3)	0.2473(6)	-0.0458(3)	0.5494(4)	19.0(5)
C(5)	0.3135(5)	0.1657(4)	0.5679(5)	5.6(3)
C(6)	0.3233(5)	0.2252(5)	0.5831(5)	7.1(3)
C(7)	0.3419(5)	0.2602(5)	0.5455(6)	8.7(4)
C(8)	0.3492(6)	0.2387(6)	0.4903(6)	10.0(4)
C(9)	0.3400(7)	0.1814(6)	0.4760(6)	10.7(4)
C(10)	0.3217(5)	0.1437(5)	0.5129(5)	7.7(3)
C(11)	0.1468(4)	0.0124(4)	0.7033(5)	5.5(2)
C(12)	0.1127(4)	0.0221(4)	0.6271(5)	6.4(3)
C(13)	0.1223(4)	0.0721(4)	0.5963(5)	6.2(3)
C(14)	0.0780(5)	0.0805(5)	0.5164(6)	9.2(4)
F(4)[a]	0.0596(9)	0.0308(7)	0.4821(7)	10.4(6)
F(5)[a]	0.1070(11)	0.107(2)	0.4877(7)	19(2)
F(6)[a]	0.0530(12)	0.1336(9)	0.5026(12)	20(2)
F(41)[b]	0.031(2)	0.045(2)	0.4848(11)	29(3)
F(51)[b]	0.1113(11)	0.084(2)	0.4845(11)	17(2)
F(61)[b]	0.0225(9)	0.1051(12)	0.5011(10)	13.5(12)
C(15)	0.1313(4)	-0.0389(4)	0.7331(5)	5.0(2)
C(16)	0.1687(5)	-0.0504(5)	0.8049(6)	8.2(4)
C(17)	0.1570(7)	-0.0965(6)	0.8371(7)	11.7(5)
C(18)	0.1062(7)	-0.1330(6)	0.7963(8)	11.1(5)
C(19)	0.0664(6)	-0.1237(5)	0.7233(7)	9.5(4)
C(20)	0.0793(5)	-0.0771(5)	0.6925(6)	7.5(3)
C(21)	0.2382(4)	0.1554(4)	0.8769(5)	5.0(2)
C(22)	0.2894(4)	0.1188(4)	0.9265(5)	5.5(2)
C(23)	0.3243(4)	0.0828(4)	0.9075(4)	4.8(2)
C(24)	0.3792(5)	0.0459(5)	0.9702(5)	7.8(3)
F(7)[a]	0.4090(11)	0.0772(9)	1.0307(7)	15.0(12)
F(8)[a]	0.4370(7)	0.0516(12)	0.9756(12)	14.5(12)
F(9)[a]	0.3566(8)	-0.0022(7)	0.9832(10)	12.3(8)
F(71)[b]	0.3891(13)	0.0519(12)	1.0331(7)	12.2(10)
F(81)[b]	0.4231(9)	0.0254(12)	0.9563(10)	9.4(7)
F(91)[b]	0.370(2)	-0.0104(6)	0.9554(11)	17(2)
C(25)	0.1999(4)	0.1928(4)	0.9005(4)	5.0(2)

C(26)	0.1654(5)	0.2413(4)	0.8588(5)	6.7(3)
C(27)	0.1294(5)	0.2772(5)	0.8779(6)	7.9(3)
C(28)	0.1252(6)	0.2640(6)	0.9375(7)	9.2(4)
C(29)	0.1592(5)	0.2170(6)	0.9784(6)	8.8(4)
C(30)	0.1962(5)	0.1822(5)	0.9615(5)	6.6(3)
C(31)	0.2371(4)	0.2657(4)	0.7351(4)	4.3(2)
C(32)	0.3010(5)	0.2758(4)	0.7950(4)	6.0(3)
C(33)	0.3496(4)	0.2337(4)	0.8250(5)	5.0(2)
C(34)	0.4172(5)	0.2510(5)	0.8895(5)	6.9(3)
F(10)	0.4332(3)	0.2160(3)	0.9440(3)	11.2(3)
F(11)	0.4201(3)	0.3049(3)	0.9129(4)	10.9(2)
F(12)	0.4643(3)	0.2453(3)	0.8745(3)	10.5(2)
C(35)	0.1871(5)	0.3142(4)	0.7033(5)	5.5(2)
C(36)	0.2046(6)	0.3734(4)	0.7140(6)	7.7(3)
C(37)	0.1567(8)	0.4165(6)	0.6808(7)	10.8(4)
C(38)	0.0913(7)	0.4005(6)	0.6399(7)	9.5(4)
C(39)	0.0751(6)	0.3422(5)	0.6310(6)	8.1(3)
C(40)	0.1222(5)	0.2989(4)	0.6614(5)	6.4(3)
N(1)	0.5000	0.3983(5)	0.2500	8.5(4)
C(41)c	0.4312(8)	0.4108(11)	0.1876(12)	14(2)
C(41A)c	0.4739(11)	0.4530(8)	0.1963(11)	9.8(8)
C(42)	0.4133(9)	0.4524(7)	0.1318(9)	14.9(7)
C(43)c	0.5069(10)	0.3446(8)	0.2990(12)	8.6(7)
C(43A)c	0.4499(9)	0.3863(10)	0.2753(12)	10.2(9)
C(44)	0.4663(7)	0.3425(7)	0.3313(8)	12.5(5)
N(2)	1.0000	0.4235(6)	0.2500	9.4(5)
C(45)c	1.0367(11)	0.4224(13)	0.3341(9)	11.9(10)
C(46c	0.997(2)	0.416(2)	0.371(2)	11.0(13)
C(47)c	0.9539(11)	0.4774(10)	0.225(2)	13.5(12)
C(48)c	0.984(4)	0.5373(11)	0.252(6)	23(4)
C(49)c	0.9600(12)	0.3660(9)	0.2313(13)	13.0(12)
C(50)	1.0000	0.3101(9)	0.2500	14.3(9)
C(51)c	1.0560(9)	0.431(2)	0.2348(13)	11.3(10)
C(52)c	1.030(2)	0.430(3)	0.155(2)	14(2)

[a] occupancy 0.54; [b] occupancy 0.46; [c] occupancy 0.50

Table 3. Bond lengths (Å) and angles (°) for [(PTFA)4Er]NEt4.

Er-O(8)	2.302(6)
Er-O(4)	2.304(6)
Er-O(5)	2.314(6)
Er-O(2)	2.321(6)
Er-O(7)	2.323(6)
Er-O(3)	2.334(6)
Er-O(1)	2.335(6)
O(1)-C(1)	1.255(9)
O(2)-C(3)	1.242(10)
O(3)-C(11)	1.265(10)
O(4)-C(13)	1.261(10)
O(5)-C(21)	1.249(10)
O(6)-C(23)	1.228(9)
O(7)-C(31)	1.260(9)
O(8)-C(33)	1.244(10)
C(1)-C(2)	1.408(12)
C(1)-C(5)	1.485(12)
C(2)-C(3)	1.394(12)
C(3)-C(4)	1.505(13)
C(4)-F(2)	1.282(13)
C(4)-F(3)	1.309(12)
C(4)-F(1)	1.313(13)
C(5)-C(6)	1.383(12)
C(5)-C(10)	1.394(13)
C(6)-C(7)	1.360(13)
C(7)-C(8)	1.38(2)
C(8)-C(9)	1.33(2)
C(9)-C(10)	1.381(14)
C(11)-C(12)	1.440(12)
C(11)-C(15)	1.465(12)
C(12)-C(13)	1.393(12)
C(13)-C(14)	1.511(13)
C(14)-F(41)	1.26(2)
C(14)-F(5)	1.28(2)
C(14)-F(51)	1.28(2)
C(14)-F(61)	1.29(2)
C(14)-F(4)	1.301(14)
C(14)-F(6)	1.31(2)
C(15)-C(16)	1.368(12)
C(15)-C(20)	1.386(12)
C(16)-C(17)	1.361(14)
C(17)-C(18)	1.35(2)
C(18)-C(19)	1.38(2)
C(19)-C(20)	1.367(14)
C(21)-C(22)	1.405(12)
C(21)-C(25)	1.500(12)
C(22)-C(23)	1.360(11)
C(23)-C(24)	1.559(12)
C(24)-F(71)	1.27(2)
C(24)-F(81)	1.30(2)
C(24)-F(8)	1.30(2)
C(24)-F(9)	1.31(2)
C(24)-F(91)	1.31(2)
C(24)-F(7)	1.33(2)
C(25)-C(30)	1.390(11)
C(25)-C(26)	1.393(12)

```
C(26)-C(27)          1.379(13)
C(27)-C(28)          1.38(2)
C(28)-C(29)          1.36(2)
C(29)-C(30)          1.357(14)
C(31)-C(32)          1.416(11)
C(31)-C(35)          1.496(12)
C(32)-C(33)          1.371(12)
C(33)-C(34)          1.538(12)
C(34)-F(12)          1.306(10)
C(34)-F(10)          1.310(11)
C(34)-F(11)          1.314(11)
C(35)-C(40)          1.360(12)
C(35)-C(36)          1.392(12)
C(36)-C(37)          1.38(2)
C(37)-C(38)          1.37(2)
C(38)-C(39)          1.37(2)
C(39)-C(40)          1.370(13)
N(1)-C(41)#1         1.51(2)
N(1)-C(41)           1.51(2)
N(1)-C(43A)          1.55(2)
N(1)-C(43A)#1        1.55(2)
N(1)-C(43)#1         1.57(2)
N(1)-C(43)           1.57(2)
N(1)-C(41A)#1        1.60(2)
N(1)-C(41A)          1.60(2)
C(41)-C(42)          1.42(2)
C(41A)-C(42)         1.40(2)
C(43)-C(44)          1.44(2)
C(43A)-C(44)         1.46(2)
N(2)-C(51)           1.52(2)
N(2)-C(51)#2         1.52(2)
N(2)-C(49)           1.54(2)
N(2)-C(49)#2         1.54(2)
N(2)-C(47)#2         1.54(2)
N(2)-C(47)           1.54(2)
N(2)-C(45)#2         1.57(2)
N(2)-C(45)           1.57(2)
C(45)-C(46)          1.51(2)
C(47)-C(48)          1.51(3)
C(49)-C(50)          1.51(2)
C(51)-C(52)          1.51(2)
O(8)-Er-O(4)          142.9(2)
O(8)-Er-O(5)          83.5(2)
O(4)-Er-O(5)         103.5(2)
O(8)-Er-O(2)         113.6(2)
O(4)-Er-O(2)          81.5(2)
O(5)-Er-O(2)         144.9(2)
O(8)-Er-O(7)          74.8(2)
O(4)-Er-O(7)          73.5(2)
O(5)-Er-O(7)          71.0(2)
O(2)-Er-O(7)         141.4(2)
O(8)-Er-O(3)         142.7(2)
O(4)-Er-O(3)          72.3(2)
O(5)-Er-O(3)          73.1(2)
O(2)-Er-O(3)          75.6(2)
O(7)-Er-O(3)         121.7(2)
O(8)-Er-O(1)          74.6(2)
O(4)-Er-O(1)          79.2(2)
O(5)-Er-O(1)         143.4(2)
```

O(2)-Er-O(1)	71.7(2)
O(7)-Er-O(1)	75.1(2)
O(3)-Er-O(1)	139.1(2)
C(1)-O(1)-Er	135.2(6)
C(3)-O(2)-Er	128.6(6)
C(11)-O(3)-Er	136.1(5)
C(13)-O(4)-Er	132.2(6)
C(21)-O(5)-Er	135.2(6)
C(31)-O(7)-Er	132.3(5)
C(33)-O(8)-Er	131.0(6)
O(1)-C(1)-C(2)	121.1(8)
O(1)-C(1)-C(5)	117.7(8)
C(2)-C(1)-C(5)	121.1(8)
C(3)-C(2)-C(1)	122.6(8)
O(2)-C(3)-C(2)	128.0(9)
O(2)-C(3)-C(4)	115.5(9)
C(2)-C(3)-C(4)	116.5(9)
F(2)-C(4)-F(3)	106.5(11)
F(2)-C(4)-F(1)	104.6(11)
F(3)-C(4)-F(1)	102.5(10)
F(2)-C(4)-C(3)	115.0(10)
F(3)-C(4)-C(3)	115.3(10)
F(1)-C(4)-C(3)	111.5(11)
C(6)-C(5)-C(10)	118.4(9)
C(6)-C(5)-C(1)	119.7(9)
C(10)-C(5)-C(1)	122.0(9)
C(7)-C(6)-C(5)	119.6(10)
C(6)-C(7)-C(8)	122.1(11)
C(9)-C(8)-C(7)	118.1(12)
C(8)-C(9)-C(10)	122.2(12)
C(9)-C(10)-C(5)	119.5(11)
O(3)-C(11)-C(12)	120.9(8)
O(3)-C(11)-C(15)	118.4(8)
C(12)-C(11)-C(15)	120.7(9)
C(13)-C(12)-C(11)	123.0(9)
O(4)-C(13)-C(12)	127.3(9)
O(4)-C(13)-C(14)	114.6(8)
C(12)-C(13)-C(14)	117.9(8)
F(41)-C(14)-F(51)	111(3)
F(51)-C(14)-F(61)	130(2)
F(5)-C(14)-F(4)	103(2)
F(5)-C(14)-F(6)	75(2)
F(4)-C(14)-F(6)	134(2)
F(41)-C(14)-C(13)	116.3(13)
F(5)-C(14)-C(13)	113.0(11)
F(51)-C(14)-C(13)	112.0(13)
F(61)-C(14)-C(13)	111.4(12)
F(4)-C(14)-C(13)	112.3(11)
F(6)-C(14)-C(13)	110.3(13)
C(16)-C(15)-C(20)	116.7(9)
C(16)-C(15)-C(11)	119.7(9)
C(20)-C(15)-C(11)	123.7(9)
C(17)-C(16)-C(15)	123.5(11)
C(18)-C(17)-C(16)	118.5(12)
C(17)-C(18)-C(19)	120.9(12)
C(20)-C(19)-C(18)	119.3(11)
C(19)-C(20)-C(15)	121.2(10)
O(5)-C(21)-C(22)	124.8(8)
O(5)-C(21)-C(25)	115.0(8)

```
C(22)-C(21)-C(25)          120.1(8)
C(23)-C(22)-C(21)          122.4(8)
O(6)-C(23)-C(22)           133.0(8)
O(6)-C(23)-C(24)           112.4(8)
C(22)-C(23)-C(24)          114.6(8)
F(71)-C(24)-F(81)          124(2)
F(8)-C(24)-F(9)            126(2)
F(71)-C(24)-F(91)          107(2)
F(81)-C(24)-F(91)           69(2)
F(8)-C(24)-F(7)             82(2)
F(9)-C(24)-F(7)            108(2)
F(71)-C(24)-C(23)          119.8(12)
F(81)-C(24)-C(23)          113.0(11)
F(8)-C(24)-C(23)           112.5(12)
F(9)-C(24)-C(23)           113.1(10)
F(91)-C(24)-C(23)          110.7(12)
F(7)-C(24)-C(23)           110.9(11)
C(30)-C(25)-C(26)          117.2(9)
C(30)-C(25)-C(21)          124.2(9)
C(26)-C(25)-C(21)          118.6(8)
C(27)-C(26)-C(25)          121.1(10)
C(28)-C(27)-C(26)          119.9(11)
C(29)-C(28)-C(27)          119.1(11)
C(28)-C(29)-C(30)          121.7(11)
C(29)-C(30)-C(25)          120.9(11)
O(7)-C(31)-C(32)           123.8(8)
O(7)-C(31)-C(35)           115.0(7)
C(32)-C(31)-C(35)          121.2(8)
C(33)-C(32)-C(31)          123.8(9)
O(8)-C(33)-C(32)           128.4(9)
O(8)-C(33)-C(34)           113.2(8)
C(32)-C(33)-C(34)          118.3(9)
F(12)-C(34)-F(10)          106.0(9)
F(12)-C(34)-F(11)          107.7(9)
F(10)-C(34)-F(11)          106.4(9)
F(12)-C(34)-C(33)          110.9(8)
F(10)-C(34)-C(33)          110.7(8)
F(11)-C(34)-C(33)          114.6(9)
C(40)-C(35)-C(36)          119.5(10)
C(40)-C(35)-C(31)          117.8(8)
C(36)-C(35)-C(31)          122.7(9)
C(37)-C(36)-C(35)          120.3(11)
C(38)-C(37)-C(36)          119.6(12)
C(39)-C(38)-C(37)          119.0(12)
C(38)-C(39)-C(40)          122.2(11)
C(35)-C(40)-C(39)          119.4(10)
C(41)#1-N(1)-C(43A)        111.8(13)
C(41)-N(1)-C(43A)#1        111.8(13)
C(41)#1-N(1)-C(43)#1       116.5(13)
C(41)-N(1)-C(43)#1          81.1(13)
C(43A)-N(1)-C(43)#1        105.5(12)
C(41)#1-N(1)-C(43)          81.1(13)
C(41)-N(1)-C(43)           116.5(13)
C(43A)#1-N(1)-C(43)        105.5(12)
C(41)-N(1)-C(41A)#1        110.2(14)
C(43A)-N(1)-C(41A)#1        87.6(13)
C(43A)#1-N(1)-C(41A)#1108.4(12)
C(43)-N(1)-C(41A)#1        104.0(12)
C(41)#1-N(1)-C(41A)        110.2(14)
```

```
C(43A)-N(1)-C(41A)        108.4(12)
C(43A)#1-N(1)-C(41A)       87.6(13)
C(43)#1-N(1)-C(41A)       104.0(12)
C(42)-C(41)-N(1)          127(2)
C(42)-C(41A)-N(1)         123(2)
C(44)-C(43)-N(1)          119.3(13)
C(44)-C(43A)-N(1)         119.1(14)
C(51)-N(2)-C(49)          121(2)
C(51)#2-N(2)-C(47)#2      111(2)
C(49)#2-N(2)-C(47)#2      111.1(13)
C(49)#2-N(2)-C(45)#2      101(2)
C(47)#2-N(2)-C(45)#2      107(2)
C(51)-N(2)-C(45)          103.3(12)
C(49)-N(2)-C(45)          101(2)
C(47)-N(2)-C(45)          107(2)
C(46)-C(45)-N(2)          120(2)
C(48)-C(47)-N(2)          118(3)
C(50)-C(49)-N(2)          116(2)
C(52)-C(51)-N(2)          110(2)
```

Symmetry transformations used to generate equivalent atoms:
#1 -x+1,y,-z+1/2   #2 -x+2,y,-z+1/2

Table 4. Torsion angles (°) for [(PTFA)4Er]NEt4.

O(8)-Er-O(1)-C(1)	153.9(8)
O(4)-Er-O(1)-C(1)	-52.6(8)
O(5)-Er-O(1)-C(1)	-150.7(7)
O(2)-Er-O(1)-C(1)	31.9(8)
O(7)-Er-O(1)-C(1)	-128.1(8)
O(3)-Er-O(1)-C(1)	-6.5(9)
O(8)-Er-O(2)-C(3)	-99.0(8)
O(4)-Er-O(2)-C(3)	45.6(8)
O(5)-Er-O(2)-C(3)	147.0(7)
O(7)-Er-O(2)-C(3)	-3.9(9)
O(3)-Er-O(2)-C(3)	119.4(8)
O(1)-Er-O(2)-C(?)	-35.8(7)
O(8)-Er-O(3)-C(11)	-166.8(8)
O(4)-Er-O(3)-C(11)	29.0(8)
O(5)-Er-O(3)-C(11)	139.7(9)
O(2)-Er-O(3)-C(11)	-56.5(8)
O(7)-Er-O(3)-C(11)	85.7(9)
O(1)-Er-O(3)-C(11)	-19.0(10)
O(8)-Er-O(4)-C(13)	167.5(7)
O(5)-Er-O(4)-C(13)	-95.4(8)
O(2)-Er-O(4)-C(13)	49.2(8)
O(7)-Er-O(4)-C(13)	-160.5(8)
O(3)-Er-O(4)-C(13)	-28.3(8)
O(1)-Er-O(4)-C(13)	122.0(8)
O(8)-Er-O(5)-C(21)	-63.2(8)
O(4)-Er-O(5)-C(21)	153.8(8)
O(2)-Er-O(5)-C(21)	59.4(10)
O(7)-Er-O(5)-C(21)	-139.3(9)
O(3)-Er-O(5)-C(21)	87.4(8)
O(1)-Er-O(5)-C(21)	-116.2(8)
O(8)-Er-O(7)-C(31)	-25.1(7)
O(4)-Er-O(7)-C(31)	174.3(8)
O(5)-Er-O(7)-C(31)	63.2(7)
O(2)-Er-O(7)-C(31)	-134.0(7)
O(3)-Er-O(7)-C(31)	118.2(7)
O(1)-Er-O(7)-C(31)	-102.8(7)
O(4)-Er-O(8)-C(33)	54.0(9)
O(5)-Er-O(8)-C(33)	-49.8(7)
O(2)-Er-O(8)-C(33)	162.1(7)
O(7)-Er-O(8)-C(33)	22.2(7)
O(3)-Er-O(8)-C(33)	-100.6(8)
O(1)-Er-O(8)-C(33)	100.6(8)
Er-O(1)-C(1)-C(2)	-17.2(13)
Er-O(1)-C(1)-C(5)	166.0(6)
O(1)-C(1)-C(2)-C(3)	-11.2(14)
C(5)-C(1)-C(2)-C(3)	165.5(9)
Er-O(2)-C(3)-C(2)	29.6(14)
Er-O(2)-C(3)-C(4)	-152.9(7)
C(1)-C(2)-C(3)-O(2)	4(2)
C(1)-C(2)-C(3)-C(4)	-173.3(9)
O(2)-C(3)-C(4)-F(2)	41(2)
C(2)-C(3)-C(4)-F(2)	-140.8(10)
O(2)-C(3)-C(4)-F(3)	166.0(11)
C(2)-C(3)-C(4)-F(3)	-16(2)
O(2)-C(3)-C(4)-F(1)	-77.6(13)

C(2)-C(3)-C(4)-F(1)	100.2(12)
O(1)-C(1)-C(5)-C(6)	-8.1(13)
C(2)-C(1)-C(5)-C(6)	175.1(9)
C(1)-C(1)-C(5)-C(10)	171.5(9)
C(2)-C(1)-C(5)-C(10)	-5.2(14)
C(10)-C(5)-C(6)-C(7)	-2(2)
C(1)-C(5)-C(6)-C(7)	178.2(9)
C(5)-C(6)-C(7)-C(8)	3(2)
C(6)-C(7)-C(8)-C(9)	-3(2)
C(7)-C(8)-C(9)-C(10)	2(2)
C(8)-C(9)-C(10)-C(5)	-1(2)
C(6)-C(5)-C(10)-C(9)	1(2)
C(1)-C(5)-C(10)-C(9)	-178.9(10)
Er-O(3)-C(11)-C(12)	-21.0(14)
Er-O(3)-C(11)-C(15)	160.6(6)
O(3)-C(11)-C(12)-C(13)	-3(2)
C(15)-C(11)-C(12)-C(13)	175.5(9)
Er-O(4)-C(13)-C(12)	23(2)
Er-O(4)-C(13)-C(14)	-162.5(7)
C(11)-C(12)-C(13)-O(4)	2(2)
C(11)-C(12)-C(13)-C(14)	-173.1(9)
O(4)-C(13)-C(14)-F(41)	-168(3)
C(12)-C(13)-C(14)-F(41)	8(3)
O(4)-C(13)-C(14)-F(5)	37(2)
C(12)-C(13)-C(14)-F(5)	-147(2)
O(4)-C(13)-C(14)-F(51)	63(2)
C(12)-C(13)-C(14)-F(51)	-122(2)
O(4)-C(13)-C(14)-F(61)	-91(2)
C(12)-C(13)-C(14)-F(61)	84(2)
O(4)-C(13)-C(14)-F(4)	153.6(14)
C(12)-C(13)-C(14)-F(4)	-31(2)
O(4)-C(13)-C(14)-F(6)	-45(2)
C(12)-C(13)-C(14)-F(6)	130(2)
O(3)-C(11)-C(15)-C(16)	-8.1(14)
C(12)-C(11)-C(15)-C(16)	173.5(10)
O(3)-C(11)-C(15)-C(20)	171.1(9)
C(12)-C(11)-C(15)-C(20)	-7.3(14)
C(20)-C(15)-C(16)-C(17)	0(2)
C(11)-C(15)-C(16)-C(17)	178.8(11)
C(15)-C(16)-C(17)-C(18)	1(2)
C(16)-C(17)-C(18)-C(19)	-1(2)
C(17)-C(18)-C(19)-C(20)	1(2)
C(18)-C(19)-C(20)-C(15)	-1(2)
C(16)-C(15)-C(20)-C(19)	0(2)
C(11)-C(15)-C(20)-C(19)	-178.9(10)
Er-O(5)-C(21)-C(22)	-10.0(14)
Er-O(5)-C(21)-C(25)	173.3(5)
O(5)-C(21)-C(22)-C(23)	2(2)
C(25)-C(21)-C(22)-C(23)	178.1(8)
C(21)-C(22)-C(23)-O(6)	1(2)
C(21)-C(22)-C(23)-C(24)	179.8(8)
O(6)-C(23)-C(24)-F(71)	178(2)
C(22)-C(23)-C(24)-F(71)	-1(2)
O(6)-C(23)-C(24)-F(81)	18(2)
C(22)-C(23)-C(24)-F(81)	-162(2)
O(6)-C(23)-C(24)-F(8)	52(2)
C(22)-C(23)-C(24)-F(8)	-127(2)
O(6)-C(23)-C(24)-F(9)	-97(2)
C(22)-C(23)-C(24)-F(9)	83(2)

```
O(6)-C(23)-C(24)-F(91)      -57(2)
C(22)-C(23)-C(24)-F(91)     123(2)
O(6)-C(23)-C(24)-F(7)       142(2)
C(22)-C(23)-C(24)-F(7)      -38(2)
O(5)-C(21)-C(25)-C(30)      156.2(9)
C(22)-C(21)-C(25)-C(30)     -20.7(14)
O(5)-C(21)-C(25)-C(26)      -23.4(12)
C(22)-C(21)-C(25)-C(26)     159.7(9)
C(30)-C(25)-C(26)-C(27)       0.3(14)
C(21)-C(25)-C(26)-C(27)    -180.0(9)
C(25)-C(26)-C(27)-C(28)      -3(2)
C(26)-C(27)-C(28)-C(29)       3(2)
C(27)-C(28)-C(29)-C(30)      -1(2)
C(28)-C(29)-C(30)-C(25)      -1(2)
C(26)-C(25)-C(30)-C(29)       1.5(14)
C(21)-C(25)-C(30)-C(29)    -178.2(9)
Er-O(7)-C(31)-C(32)          20.4(12)
Er-O(7)-C(31)-C(35)        -161.4(5)
O(7)-C(31)-C(32)-C(33)        0.4(14)
C(35)-C(31)-C(32)-C(33)    -177.8(8)
Er-O(8)-C(33)-C(32)         -15.7(14)
Er-O(8)-C(33)-C(34)         162.4(6)
C(31)-C(32)-C(33)-O(8)       -3(2)
C(31)-C(32)-C(33)-C(34)     179.4(8)
O(8)-C(33)-C(34)-F(12)       64.0(11)
C(32)-C(33)-C(34)-F(12)    -117.7(10)
O(8)-C(33)-C(34)-F(10)      -53.4(11)
C(32)-C(33)-C(34)-F(10)     124.9(10)
O(8)-C(33)-C(34)-F(11)     -173.8(8)
C(32)-C(33)-C(34)-F(11)       4.5(13)
O(7)-C(31)-C(35)-C(40)       21.1(12)
C(32)-C(31)-C(35)-C(40)    -160.6(8)
O(7)-C(31)-C(35)-C(36)     -157.9(9)
C(32)-C(31)-C(35)-C(36)      20.4(13)
C(40)-C(35)-C(36)-C(37)      -2(2)
C(31)-C(35)-C(36)-C(37)     177.2(9)
C(35)-C(36)-C(37)-C(38)       3(2)
C(36)-C(37)-C(38)-C(39)      -2(2)
C(37)-C(38)-C(39)-C(40)       0(2)
C(36)-C(35)-C(40)-C(39)      -1(2)
C(31)-C(35)-C(40)-C(39)    -179.5(9)
C(38)-C(39)-C(40)-C(35)       2(2)
```

Symmetry transformations used to generate equivalent atoms:
#1 -x+1,y,-z+1/2   #2 -x+2,y,-z+1/2

Table 5. Hydrogen coordinates and isotropic displacement parameters ($A^2 \times 10^3$) for [(PTFA)4Er]NEt4.

	x	y	z	U_{iso}
H(2A)	0.2372(5)	0.0660(4)	0.5489(5)	7.5
H(2B)	0.3122(5)	0.0521(4)	0.5816(5)	7.5
H(6)	0.3171(5)	0.2412(5)	0.6188(5)	8.5
H(7)	0.3501(5)	0.2999(5)	0.5574(6)	10.5
H(8)	0.3602(6)	0.2636(6)	0.4638(6)	12.0
H(9)	0.3460(7)	0.1663(6)	0.4398(6)	12.8
H(10)	0.3150(5)	0.1039(5)	0.5012(5)	9.2
H(12A)	0.1226(4)	−0.0114(4)	0.6065(5)	7.7
H(12B)	0.0657(4)	0.0203(4)	0.6103(5)	7.7
H(16)	0.2040(5)	−0.0255(5)	0.8332(6)	9.9
H(17)	0.1835(7)	−0.1026(6)	0.8862(7)	14.1
H(18)	0.0979(7)	−0.1649(6)	0.8174(8)	13.3
H(19)	0.0312(6)	−0.1489(5)	0.6956(7)	11.4
H(20)	0.0528(5)	−0.0709(5)	0.6434(6)	8.9
H(22A)	0.3214(4)	0.1441(4)	0.9644(5)	6.6
H(22B)	0.2703(4)	0.0940(4)	0.9478(5)	6.6
H(26)	0.1666(5)	0.2496(4)	0.8175(5)	8.0
H(27)	0.1081(5)	0.3103(5)	0.8506(6)	9.5
H(28)	0.0994(6)	0.2869(6)	0.9495(7)	11.0
H(29)	0.1570(5)	0.2085(6)	1.0191(6)	10.6
H(30)	0.2195(5)	0.1507(5)	0.9911(5)	7.9
H(32A)	0.3197(5)	0.3083(4)	0.7820(4)	7.2
H(32B)	0.2944(5)	0.2900(4)	0.8331(4)	7.2
H(36)	0.2488(6)	0.3841(4)	0.7436(6)	9.2
H(37)	0.1687(8)	0.4560(6)	0.6863(7)	12.9
H(38)	0.0584(7)	0.4291(6)	0.6184(7)	11.5
H(39)	0.0308(6)	0.3314(5)	0.6034(6)	9.7
H(40)	0.1099(5)	0.2595(4)	0.6536(5)	7.6
H(41A)	0.4145(8)	0.3733(11)	0.1638(12)	17.2
H(41B)	0.4047(8)	0.4207(11)	0.2089(12)	17.2
H(41C)	0.4727(11)	0.4865(8)	0.2234(11)	11.8
H(41D)	0.5077(11)	0.4614(8)	0.1843(11)	11.8
H(43A)	0.4981(10)	0.3092(8)	0.2706(12)	10.3
H(43B)	0.5528(10)	0.3428(8)	0.3373(12)	10.3
H(43C)	0.4420(9)	0.4233(10)	0.2919(12)	12.2
H(43D)	0.4083(9)	0.3746(10)	0.2336(12)	12.2
H(45A)	1.0685(11)	0.3904(13)	0.3504(9)	14.2
H(45B)	1.0619(11)	0.4586(13)	0.3514(9)	14.2
H(46A)	1.026(2)	0.416(2)	0.422(2)	14.3
H(46B)	0.973(2)	0.379(2)	0.357(2)	14.3
H(46C)	0.966(2)	0.448(2)	0.358(2)	14.3
H(47A)	0.9310(11)	0.4785(10)	0.173(2)	16.3
H(47B)	0.9206(11)	0.4712(10)	0.238(2)	16.3
H(48A)	0.951(4)	0.5668(11)	0.233(6)	29.7
H(48B)	1.016(4)	0.5452(11)	0.238(6)	29.7
H(48C)	1.006(4)	0.5379(11)	0.304(6)	29.7
H(49A)	0.9351(12)	0.3659(9)	0.2557(13)	15.5
H(49B)	0.9283(12)	0.3659(9)	0.1802(13)	15.5
H(50A)	0.9708	0.2768(9)	0.2363	18.6
H(50B)	1.0308	0.3089(9)	0.3007	18.6
H(50C)	1.0239	0.3089(9)	0.2249	18.6
H(51A)	1.0780(9)	0.469(2)	0.2543(13)	13.6

H(51B)	1.0883(9)	0.400(2)	0.2579(13)	13.6
H(52A)	1.065(2)	0.435(3)	0.146(2)	17.6
H(52B)	0.998(2)	0.461(3)	0.132(2)	17.6
H(52C)	1.008(2)	0.393(3)	0.136(2)	17.6

Table 6. Anisotropic parameters ($A^2 \times 10^2$) for [(PTFA)4Er]NEt4.
The anisotropic displacement factor exponent takes the form:
$-2 \pi^2 [h^2 a^{*2} U11 + \ldots + 2 h k a^* b^* U12]$

	U11	U22	U33	U23	U13	U12
Er	4.52(2)	4.57(2)	3.35(2)	-0.49(2)	1.76(2)	-0.07(2)
O(1)	7.2(4)	5.1(3)	4.2(3)	-1.4(3)	3.3(3)	-1.1(3)
O(2)	7.6(4)	6.0(4)	3.9(3)	-0.1(3)	3.5(3)	0.9(3)
O(3)	6.2(4)	7.8(5)	3.6(3)	-0.8(3)	2.5(3)	-2.3(4)
O(4)	5.1(3)	5.8(4)	4.7(3)	0.1(3)	1.6(3)	-0.5(3)
O(5)	6.8(4)	6.2(4)	4.2(4)	-1.0(3)	3.2(3)	-0.1(3)
O(6)	5.4(4)	5.8(4)	3.5(3)	0.1(3)	1.6(3)	1.6(3)
O(7)	7.0(4)	4.1(4)	5.2(4)	-0.2(3)	2.6(3)	-0.2(3)
O(8)	5.4(4)	6.3(4)	4.1(3)	-0.9(3)	1.8(3)	-0.4(3)
C(1)	4.8(5)	6.4(6)	3.7(5)	-1.6(5)	1.8(4)	-0.7(5)
C(2)	5.1(6)	8.2(8)	5.3(6)	-1.3(6)	2.6(5)	0.0(5)
C(3)	5.4(6)	4.9(6)	7.0(7)	-0.8(5)	3.5(5)	0.2(5)
C(4)	15.1(12)	6.6(8)	9.4(9)	-2.5(7)	7.6(9)	0.3(8)
F(1)	17.7(8)	8.3(6)	26.1(11)	-1.7(6)	13.1(8)	3.3(6)
F(2)	17.6(7)	7.9(5)	16.5(7)	-3.3(5)	11.1(6)	-4.5(5)
F(3)	41(2)	7.1(5)	12.6(6)	-5.2(4)	16.6(8)	-6.0(7)
C(5)	6.2(6)	6.5(7)	4.6(5)	-0.6(5)	3.2(5)	-0.5(5)
C(6)	9.7(8)	7.4(8)	5.5(6)	-1.1(5)	4.8(6)	-1.8(6)
C(7)	10.1(9)	8.5(8)	7.5(8)	-1.0(7)	4.4(7)	-3.3(7)
C(8)	14.6(11)	10.7(10)	8.4(8)	0.7(7)	8.6(8)	-1.1(9)
C(9)	18.0(13)	9.5(10)	8.3(8)	0.1(7)	9.5(9)	-0.7(9)
C(10)	10.3(8)	7.5(7)	6.3(7)	-0.4(6)	5.0(7)	0.2(6)
C(11)	5.2(6)	6.5(6)	5.3(6)	1.2(5)	3.2(5)	0.9(5)
C(12)	4.7(6)	7.1(7)	6.9(7)	0.5(6)	2.6(6)	-1.2(5)
C(13)	5.0(6)	6.0(7)	5.2(6)	0.1(5)	0.9(5)	-0.5(5)
C(14)	8.7(10)	8.8(10)	5.1(7)	1.5(7)	-0.1(7)	-3.1(8)
F(4)	15(2)	8.9(10)	4.7(8)	-1.7(7)	3.2(9)	-3.9(11)
F(5)	22(2)	22(2)	2.9(8)	1.8(11)	0.1(13)	-15(2)
F(6)	14(2)	23(3)	13(2)	11(2)	0(2)	2(2)
F(41)	20(3)	38(5)	8(2)	10(2)	-8(2)	-25(3)
F(51)	15(2)	29(4)	10(2)	1(2)	8(2)	0(3)
F(61)	7.8(14)	20(3)	5.9(11)	1(2)	-1.9(11)	8(2)
C(15)	4.5(5)	5.4(6)	5.1(5)	-0.1(4)	2.4(5)	-0.8(4)
C(16)	5.6(7)	10.6(9)	6.2(7)	2.8(6)	1.3(6)	-1.2(6)
C(17)	9.5(10)	13.4(12)	9.1(9)	5.7(9)	2.5(8)	-1.6(9)
C(18)	13.1(12)	9.6(10)	10.9(11)	4.0(8)	6.4(10)	-0.6(9)
C(19)	9.9(9)	8.8(9)	10.5(9)	-0.4(8)	5.8(8)	-3.7(7)
C(20)	8.4(8)	7.2(7)	6.2(7)	0.6(6)	3.3(6)	-1.1(6)
C(21)	5.7(6)	5.0(6)	5.2(6)	-0.9(4)	3.5(5)	-0.5(5)
C(22)	6.4(6)	5.8(6)	5.0(5)	0.2(5)	3.3(5)	-0.4(5)
C(23)	4.5(5)	5.2(6)	3.3(5)	-0.2(4)	1.1(4)	-0.8(5)
C(24)	7.0(8)	9.2(10)	6.3(8)	3.0(7)	2.7(7)	2.6(7)
F(7)	14(2)	12(2)	6.3(11)	-1.6(10)	-4.1(11)	5.2(12)
F(8)	6.6(10)	25(3)	11(2)	5(2)	3.6(10)	4.2(13)
F(9)	10.6(11)	14(2)	12(2)	7.9(12)	5.3(11)	3.0(10)
F(71)	19(2)	14(2)	4.1(10)	4.9(10)	6.6(12)	11(2)
F(81)	8.5(14)	13(2)	5.4(10)	5.1(11)	2.8(10)	5.6(12)
F(91)	32(4)	7.3(14)	12(2)	6.7(11)	10(2)	7(2)
C(25)	6.6(6)	5.3(6)	4.4(5)	-0.2(4)	3.6(5)	-0.8(5)
C(26)	7.9(7)	6.9(7)	6.0(6)	-0.1(5)	4.1(6)	0.3(6)

C(27)	6.6(7)	6.7(7)	11.1(9)	0.2(7)	5.0(7)	1.4(6)
C(28)	8.6(8)	10.5(10)	10.9(10)	−3.1(8)	6.8(8)	0.5(7)
C(29)	8.4(8)	13.8(12)	6.2(7)	−2.2(7)	5.2(7)	−0.2(8)
C(30)	8.1(7)	7.3(7)	5.9(6)	−0.5(5)	4.7(6)	−0.7(6)
C(31)	5.8(6)	5.1(5)	2.9(4)	−0.6(4)	2.8(4)	−0.9(4)
C(32)	7.5(7)	7.2(7)	3.7(5)	−1.4(5)	3.2(5)	−2.4(6)
C(33)	4.7(5)	5.9(6)	4.6(5)	−0.3(5)	2.5(5)	−0.2(5)
C(34)	5.9(7)	8.9(8)	5.5(6)	−2.1(6)	2.7(6)	−1.9(6)
F(10)	9.8(5)	14.3(7)	5.7(4)	0.5(4)	1.1(4)	−2.4(5)
F(11)	9.0(5)	10.8(5)	9.3(5)	−4.5(4)	2.2(4)	−2.7(4)
F(12)	6.0(4)	15.2(7)	9.3(5)	−3.9(4)	3.2(4)	−2.8(4)
C(35)	8.0(7)	4.2(5)	5.9(6)	0.1(5)	4.7(5)	−0.4(5)
C(36)	9.4(8)	5.1(7)	7.4(7)	−1.0(6)	3.5(6)	0.0(6)
C(37)	16.8(13)	6.5(8)	9.6(10)	0.3(7)	7.2(10)	0.8(10)
C(38)	10.2(10)	7.5(9)	9.2(9)	0.3(7)	3.7(8)	3.4(8)
C(39)	7.7(8)	7.2(8)	8.6(8)	1.5(6)	3.6(7)	0.5(7)
C(40)	5.5(6)	6.4(7)	6.8(7)	2.0(5)	2.9(6)	0.6(5)
N(1)	10.1(10)	4.8(8)	13.4(12)	0.0	8.0(10)	0.0
C(41)	3.0(13)	14(3)	22(4)	−10(3)	3(2)	0(2)
C(41A)	14(2)	4.5(13)	14(2)	0.4(14)	10(2)	−1(2)
C(42)	15(2)	14.0(14)	12.9(13)	7.7(11)	5.3(12)	3.7(12)
C(43)	5.2(12)	8(2)	12(2)	1.1(14)	4(2)	2.5(13)
C(43A)	5.2(13)	11(2)	15(2)	−4(2)	6(2)	−1.8(14)
C(44)	12.7(11)	12.5(12)	15.0(13)	5.0(10)	8.9(11)	0.3(10)
N(2)	6.4(9)	11.1(13)	8.1(10)	0.0	1.7(9)	0.0
C(45)	8(2)	12(2)	12(2)	0(2)	2(2)	−1(2)
C(46)	10(2)	15(3)	10(2)	−1(2)	7(2)	−1(3)
C(47)	7(2)	17(3)	17(3)	9(3)	7(2)	7(2)
C(48)	31(8)	8(2)	34(5)	1(5)	20(7)	−2(4)
C(49)	13(2)	18(3)	6(2)	−1(2)	3(2)	−4(2)
C(50)	21(3)	9(2)	15(2)	0.0	11(2)	0.0
C(51)	6(2)	19(3)	10(2)	5(2)	5(2)	2(2)
C(52)	12(3)	19(4)	12(3)	0(3)	8(3)	−2(3)